N d'ordre: 40080

Université des Sciences et Technologies de Lille

Ecole Doctorale des Sciences Pour l'Ingénieur

Alignement et caractérisation de nanofils semiconducteurs

THESE

présentée a l'Université des Sciences et Technologies de Lille

pour obtenir le titre de

Docteur de l'Université

Spécialité : Micro et Nanotechnologies, Acoustique et Télécommunications

par

Marcin MARCZAK

Soutenue le **17 septembre 2009** devant le jury composé de:

Rapporteurs :	Serge LEFRANT
	Rajmund BACEWICZ
Examinateurs :	Liviu NICU
	Jerzy GARBARCZYK
Co-encadrants :	Djamila HOURLIER
	Heinrich DIESINGER
Directeurs de thèse :	Thierry MELIN
	Leszek ADAMOWICZ

WARSAW UNIVERSITY
OF TECHNOLOGY

Faculty of Physics

Ph.D. THESIS

Marcin Marczak, M.Sc., Eng.

Alignment and characterization of semiconducting nanowires

Supervisors
Leszek Adamowicz, Ph.D. (WUT)
Thierry Mélin, Ph.D (IEMN)

Warsaw, 2009

To my mother

Mojej mamie

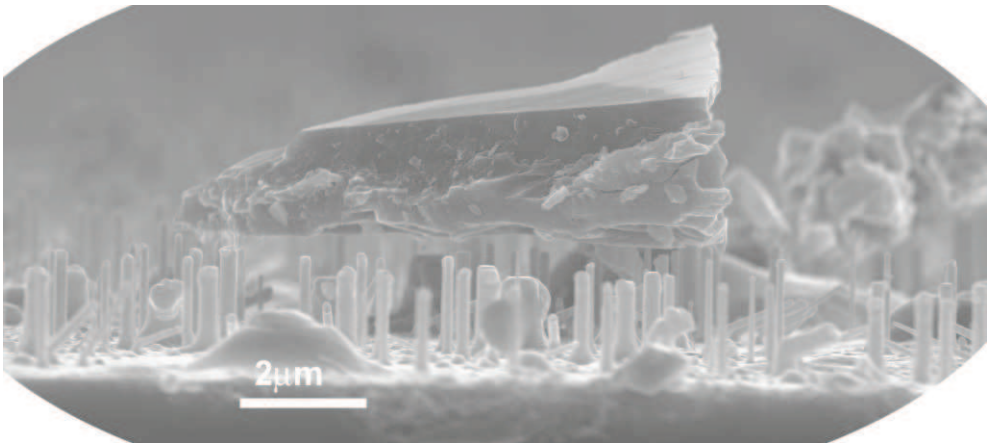

Résumé

Le but de ce travail est de mieux comprendre les propriétés chimiques, microstructurales, mécaniques et les propriétés d'assemblage de nanofils obtenus par dépôt chimique en phase vapeur (CVD).

La première partie de cette étude est consacrée à l'analyse par spectroscopie Raman de nanofils de silicium isolés obtenus par CVD. L'analyse des spectres Raman indique la présence de silicium sous deux formes: l'une correspondant à du silicium cristallin (cSi) à 520 cm^{-1} et l'autre correspondant à du silicium amorphe (aSi) à 470 cm^{-1} formant une structure coeur-coquille (cSi-aSi). La température de ces deux phases $T_{cSi} < T_{aSi}$ est déterminée en fonction du rapport des intensités Stokes/anti-Stokes, de la position et de la largeur à mi-hauteur des pics Raman. On montre que le coeur des nanofils est en contact thermique avec le substrat, favorisant l'évacuation de chaleur. L'asymétrie de type Fano du pic à 520 cm^{-1} permet en outre d'estimer le dopage au bore des nanofils silicium, de l'ordre de 10^{19} cm^{-3}.

Dans la deuxième partie, une nouvelle approche d'assemblage de nanofils à partir de suspensions liquides est présentée. Elle est basée sur un dispositif de micro-pompe par diélectrophorèse à champ propagatif qui génère la polarisation à quadrature de phase par dispersion structurelle entre l'isolant capacitif de la matrice d'électrodes et le liquide faiblement conducteur. La spectroscopie d'impédance est utilisée, afin de déterminer la fréquence de croisement et de maximiser l'effet de pompage. La propagation et rotation des nanofils sont observées et interprétées en termes d'une compétition entre forces de pompage, de piégeage et d'entraînement visqueux.

Dans la troisième partie, deux voies ont été empruntées pour obtenir des systèmes

à nanofils suspendus, l'une, basée sur la diélectrophorèse statique, et l'autre, basée sur l'alignement direct lors du procédé de synthèse. Ces systèmes seront utilisés pour (1) des systèmes nanoélectromécaniques suspendus (*e.g.* pour biocapteurs) et (2) réaliser des dipositifs de type transistors, en couplage direct avec la spectroscopie Raman (variations de l'asymétrie de type Fano du pic 520 cm^{-1} en fonction de la tension de grille).

Abstract

The aim of the present study was to develop a better understanding of the chemical, microstructural, mechanical properties and assembly techniques of nanowires obtained by chemical vapor deposition (CVD).

The fist part deals with the results of Raman scattering of well-separated silicon nanowires (SiNWs) obtained by thermal decomposition on gold-catalytic sites by CVD method and deposited on a Au surface. The Raman spectra analysis indicates the presence of two silicon phases: crystalline (cSi) - 520 cm^{-1} and amorphous (aSi) - 470 cm^{-1}, forming a core (cSi) - shell (aSi) structure. The Raman spectra have been acquired from three points along cone shaped nanowires: base, center and tip. Based on the Stokes/anti-Stokes intensity ratios, the position and full width at half maximum of the Raman peaks, the temperatures of the $T_{cSi} < T_{aSi}$ have been determined. It suggests that the nanowire cSi core is in a good thermal contact with the metallic substrate, allowing heat evacuation of the SiNW core, for which the thermal conductivity is known to be low. Moreover the carrier concentration of the boron-doped SiNWs was estimated at 10^{19} cm^{-3} from the Fano-like asymmetry of the peak at 520 cm^{-1}.

In the second part, a new approach to SiNW manipulation is presented. At the beginning the travelling wave dielectrophoresis (twDEP) micro liquid pump design and its work principle is presented. Our device is used to simultaneously pump a weakly ionic SiNW suspension and to trap and to rotate SiNWs. The rotation is out-of-plane with respect to the electrodes. To maximize liquid pumping the cross-over frequency of the RC replacement circuit representing the liquid conductivity and the

insulating layer covering the electrodes was determined by impedance spectroscopy. The observed propagation and rotation of nanowires is explained by means of a frequency dependent competition between trapping and drag forces.

In the third part two different approaches have been tested for obtaining a suspended nanowire structures. The first one is based on static dielectrophoresis and the second one on the direct alignment during the growth process. These systems will be used for: (1) nanoelectromechanical systems (e.g. for a biosensor); (2) nanowire field effect ransistor structures coupled with Raman spectrometer (to observe a change in the asymmetry of the Fano-like 520 cm^{-1} peak in function of a gate voltage).

Contents

Acknowledgments

I would like to thank my supervisors Dr Thierry Mélin form the Institute d'Electronique, Microélectronique et de Nanotechnologie in France and professor Leszek Adamowicz from Faculty of Physics at Warsaw University of Technology for giving me the opportunity to perform this work at both universities, their kindness, support and involvement in my research: Merci beaucoup pour tout Thierry!

Je voudrais remercier Dr Djamila Hourlier pour l'encadrement de mes travaux scientifiques et tout ce que j'ai appris avec elle. Merci Djamila!

Ich möchte mich ganz herzlich bei Dr. Heinrich Diesinger für seine Betreuung, Engagement für meine Arbeit, für alles was ich von Ihm gelernt habe und die Hilfe mit der berühmten französischen Bürokratie bedanken!! Danke schön Heinrich!

Je voudrais remercier Dr Emmanuelle Pichonat pour leur l'aid pendat les mesures Raman. Merci Emmanuelle!

I would like to thank all my friends and colleagues in Lille for creating great and motivating work atmosphere. Thank you Claudio, Łukasz, David, Timothée, Damien, Anisha, Nicolas, Ondrej, Edern, Sara, Ludger W., Françoise V., Jean Philippe N., Dominique D., Florence S. and Bernard L.

Chciałbym podziekować kolegom w Warszawie za stworzenie miłej atmosfery pracy. Dziękuję Mariuszu, Jarku, Krzysztofie, Aniu, Czarku, Wojtku i Michale!

I would like to address my special thanks to the people closest to me: Danke schön Myriam für deine Unterstützung und dass Du immer da warst! Dziękuję moim rodzicom, dziadkom oraz mojej siostrze za wsparcie! Je voudrais remercier ma tante Marie pour son aide! Dziękuję Olku, Kaju, Piotrze i Magdo!

Chapter 1

Introduction

This PhD thesis was realized according to the co-tutelle agreement between Faculty of Physics, Warsaw University of Technology in Poland (WUT) and Université des Sciences et Technologies de Lille in France(USTL).

1.1 Aim

The aim of this research was to align and characterize semiconducting nanowires for applications in nanodevices like shown in Fig. 1.1.

Nanowires were characterized (structure, temperature and doping) using Raman Spectroscopy technique at Warsaw University of Technology and at the Institut d'Electronique de Microlectronique et de Nanotechnologie (IEMN/USTL)* for complementary experiments when needed. A new pumping principle was demonstrated and its usefulness to device fabrication was successfully proved in providing suspended nanowire structures for NEMS applications, electrical and Raman characterization

*the doping analysis with collaboration with E. Pichonat from Laboratoire de Spectrochimie Infrarouge et Raman in Lille, France

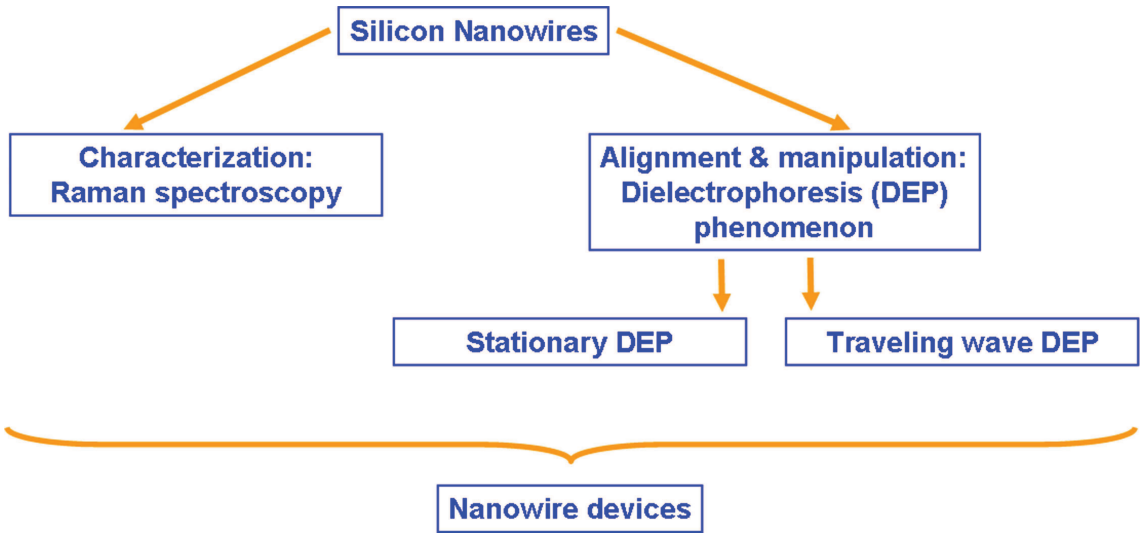

Figure 1.1: The aim of this research was to align and characterize semiconducting nanowires for applications in nanodevices.

1.2 Novelty of this work

1. A liquid micro-pump based on traveling dielectrophoresis was designed and proved to be a good tool for nanowire suspension pumping and nanowire handling;

2. Raman spectroscopy was shown as a fast and convenient tool to obtain information about silicon nanowire structure and its doping level;

3. Devices using suspended nanowires were built to test their usability for nanoelectromechanical systems (*e.g.* biosensors) and to observe gate effect by Raman spectrometry, since the modulation of the carrier density is expected to vary the Fano effect;

4. An electro-mechanical actuation of suspended silicon nanowires at their resonance frequency was shown and an mechanical actuation of germanium nanowires at their 1^{st}, 2^{nd} and 3^{rd} resonance frequency was shown.

1.3 Overview

This work is divided into three sections. At the very beginning (section 1.4) I will present the basics of how the silicon and germanium nanowires are grown [†], as methods and tools presented later aim on their analyzing and manipulating.

In the first part (**chapter 2**) silicon nanowire structure and doping are analyzed. The results of Raman scattering study of individual nanowires deposed on an Au surface. The Raman spectra analysis indicates presence of both crystalline (520 cm^{-1}) and amorphous (470 cm^{-1}) silicon phases, forming quite independent fractions. From the growth conditions, nanowires are expected to form such a core-shell cone, with the amorphous silicon phase (aSi) outside, and the crystalline silicon phase (cSi) inside. The nanowire diameter varies from 100 nm to 400 nm. The Raman spectra have been acquired from the three points of the cone shaped nanowire: base, center and tip. Based on the Stokes/anti-Stokes (St/aSt) intensity ratios, the position and full width at half maximum of the Raman peaks temperatures of the amorphous shell and the cSi core in different position along the nanowire different have been determined. Against our expectations, the crystalline silicon (cSi) temperature was found lower than the amorphous silicon temperature (aSi). This suggests that the nanowire cSi core is in a good thermal contact with the metallic substrate, thus improving the heat evacuation of the SiNW core, for which the thermal conductivity is known to be low. Additionally it will be shown how one can investigate boron doping of SiNW from Fano-like asymmetry of the Raman peak at 520 cm^{-1}. The doping level was determined at the level of 10^{19} atoms/ cm^{-3}.

micropump is presented.

In the second part (**Chapter 3**) a new approach to the manipulation of silicon nanowires is described. At the beginning the design and working principle of a travelling wave dielectrophoresis micropump is presented. The cell impedance is monitored by impedance spectroscopy, and pumping is maximized by operating the array at the impedance crossover frequency. Next this device is used to simultane-

[†]synthesis was performed by D. Hourlier at Institut d'Electronique, de Microlectronique et de Nanotechnologie in France

ously pump a weakly ionic nanowire suspension and to trap and to rotate nanowires. The rotation is out-of-plane with respect to the electrodes. This is in contrast to previous works, where nanowire rotation was in the electrode plane. The observed propagation and rotation of nanowires is explained by means of a frequency dependent competition between trapping and drag forces.

In the third part (**Chapter 4**) a procedure based on static dielectrophoresis to prepare suspended nanowire structures is presented. They are used : (1) to combine transport (field-effect characterization) of suspended nanowires, and to check the free carrier concentration shift while operation the device from its back-gate, through the change in Raman spectroscopy (asymmetry of the 520 cm^{-1} Fano line); (2) for fabrication of suspended nanowires upon electrode arrays for electrostatic actuation and detection in the $\sim$57 MHz range, and contributing in (3) fabricating suspended nanowires directly from oriented growth between etched walls in a silicon wafer for mechanical excitation in the 5 MHz range, where their 1^{st}, 2^{nd} and 3^{rd} resonance frequency was registered.

1.4 Nanowires growth

Silicon and germanium nanowires

The method for silicon nanowires growth, is presented in detail in work of Hourlier *et al.* [1]. In general nanowires were grown as follows:

As shown in Fig. 1.2 a ⟨111⟩ Si wafer coated with a thin layer of Au (5 nm) is used as a substrate to grow Si nanowires. It is heated to a high temperature (< 500 °C for Si and < 900 °C for Ge) until the Au layer forms liquid alloy nanodroplets with the underlying Si substrate. A gas mixture of SiH_4 (for GeNW GeH_4) diluted in 10% H_2 in argon under gas flow dynamics is introduced in the growth CVD chamber. It preferentially dissolves in the Au-Si (Au-Ge) alloy nanodroplets. Once the liquid droplet is supersaturated with silicon, then the precipitation of the solid silicon (germanium) nanowire occurs. Figure 1.3 shows an SEM image of a Si nanowire array on a Si⟨111⟩ substrate and a Ge array in Fig. 1.4. The vast majority of nanowires grow out of the liquid droplet perfectly orthogonal to the substrate.

Silicon nanowires (SiNW) are up to 15 μm long and from 50 to 200 nm in

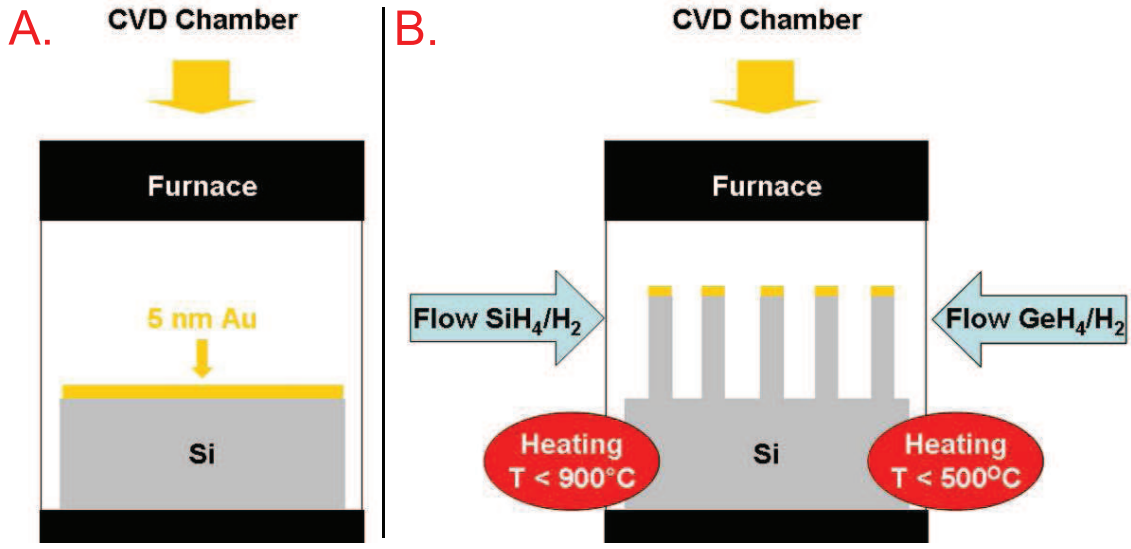

Figure 1.2: Semiconducting nanowire growth process. **A.** A (111) silicon substrate covered with 5 nm gold is introduced into CVD chamber; **B.** Depending on the nanowire type, whole system is heated up and under a SiH_4 gas flow for silicon nanowires and GeH_4 for germanium nanowires (mixed with H_2) growth occurs.

diameter. Germanium nanowires (GeNW) are longer - up to 20 μm and much thiner - from 3 to 30 nm. Both types are undoped or doped (boron or phosphorous). As seen in the Fig. 1.4, GeNW are not perpendicular to the surface. This effect is due to their length to diameter ratio. This causes their bending.

Bottom-up approach of nanowires growth can be directly use in the device fabrication. As will be shown in the following chapters nanowires can be also grown on the walls etched in silicon, which results in the nanowires parallel to the wafer surface (see Fig. 3.1 and Fig. 4.10).

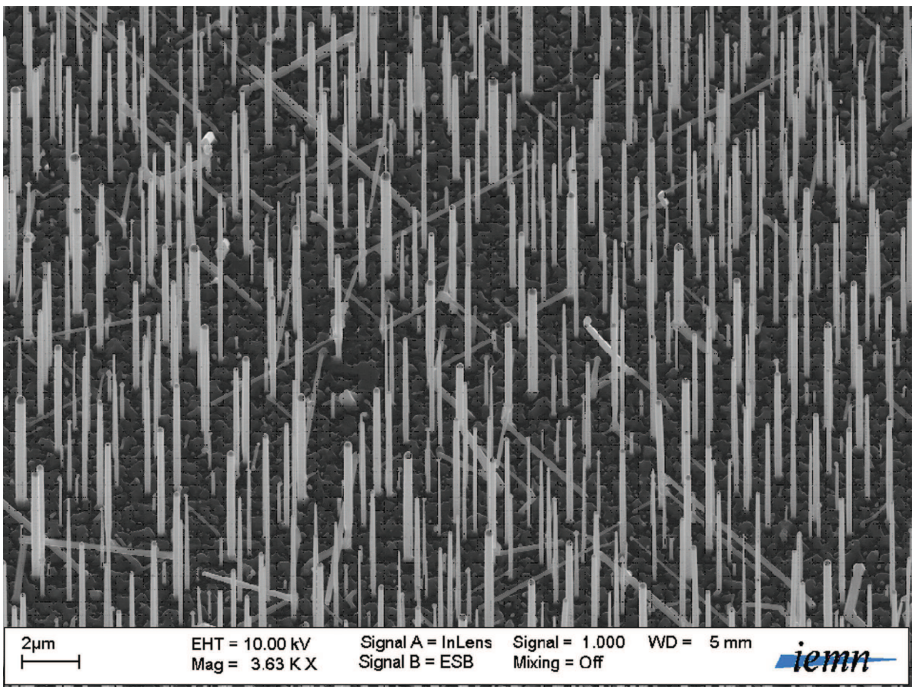

Figure 1.3: Silicon nanowires grown on the ⟨111⟩ silicon substrate using VLS technique.

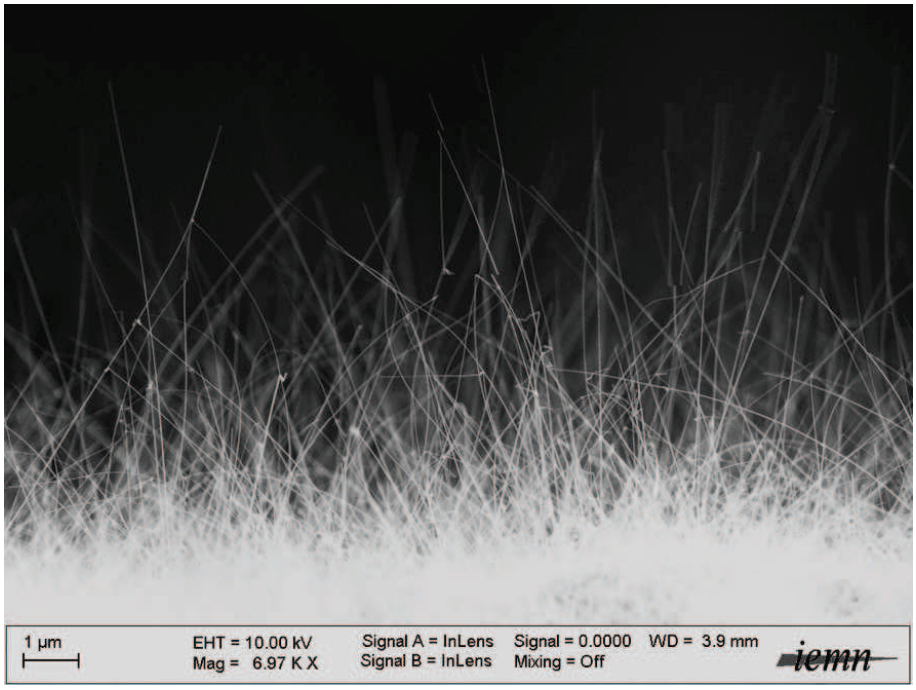

Figure 1.4: Germanium nanowires: length 10 μm and diameter $15 - 20$ nm.

Chapter 2

Raman Spectroscopy

In this chapter I will focus on Raman Spectroscopy (RS) applied to silicon nanowires. At the beginning of the Chapter (2.1) I will introduce Raman spectroscopy. In this part I will answer the questions what it is, what are its origins and where can we use it. Next, I will continue to its application to nanowires deposited on the golden surface and their structure analysis. In section (2.2) I will determine the cone-shaped nanowire structure, where amorphous (aSi) and crystalline silicon (cSi) phases will be investigated. It will turn out that silicon nanowires investigated here form a core/ shell structure, where the core is made of cSi and shell from aSi. Based on this structure I will investigate in section (2.3) the temperature of these two phases based on the Stokes/anti-Stokes ratio and silicon LO-TO mode shift. The tip of the SiNWs is found in a good thermal contact with the golden surface, explaining the lower temperature of the core than the shell of the SiNW. Next, in section (2.4) I will show how one can investigate boron doping of SiNW from Fano-like asymmetry of the Raman peak at 520 cm^{-1}. The doping level was determined at the level of 10^{19} cm^{-3}.

2.1 Introduction

Raman spectroscopy is one of many spectroscopic techniques using inelastic scattering of monochromatic light. During this process energy is exchanged between incident photon and molecule or material lattice. As a result of this a scattered photon has a higher or lower energy compared to the initial one. This energy difference comes from change of the vibration or rotation energy and thus gives insight to its energy levels. From its discovery in 1928 a lot of theoretical and experimental work in Raman spectroscopy was focused on inelastic light scattering fundamentals and its applications to understand molecule structure. With time the role of Raman spectroscopy in advanced research got more and more important and found application also in nanotechnology.

Discovery

All has started with Einstein's hypothesis that light consists of quanta confirmed in 1923 by A.H. Compton who discovered the effect known under his name (a change in energy of an X-ray photon or γ-rays, while interacting with matter) [2]. Based on this discovery [3] the physicist Adolf Smekal predicted from the quantum nature of light that the scattered monochromatic light would consist of its original wavelength and also from lower and higher wavelengths. First evidence was published in 1928 by the Russian scientists **Grigorii Samuilovich Landsberg** and **Leonid Isaakovich Mandelstam** who were studying the A. Einstein's and P. Debye's theories of specific heat of solids. They have expected that the frequency of light scattered by crystal would not only be diffracted by the Debye elastic waves acting as a grating, but also it would experience a frequency shift due to elastic waves propagating at the velocity of sound. While looking for this change in quartz they had observed a different one than they had expected. They were sure to discover a new phenomenon but they were not able to explain it.

In 1922 **Sir Chandrasekhara Venkata Raman** [see figure 2.1] together with **Sir Kariamanickam Srinivasa Krishnan** made their discovery while looking for

Figure 2.1: Sir Chandrasekhara Venkata Raman (1888 - 1970) [3].

an optical analogue to the Compton effect. They were observing the depolarization of water as a function of wavelength. Three years later K.S. Krishnan observed a "feeble fluorescence" when light was scattered by various liquids.* However determining the spectra was difficult due to its very low intensity. In 1928 C. V. Raman at the meeting of the South Indian Scientists Association (March 16, 1928) has presented spectra showing a change of frequency. He and K.S. Krishnan have altogether examined 60 vapors and liquids and observed second radiation of a smaller frequency. As the scattered light had high intensity and was polarized, they have excluded fluorescent radiation as a cause of it [3]. Before this lecture C.V. Raman sent on February and March 1928 [4] two short articles to *Nature*, which appeared in print before the first publication of the Russian physicists (*Die Nautrewissenschaften*, May 6, 1928).

For his discovery C.V. Raman received in 1930 the Noble Prize in Physics and

*in regard to professor S. Lefrant (Institut des Matriaux Jean Rouxel, France) remark: a french scientist Jean Cabannes has indentified independently the inelastic light scattering in gases, so called Cabannes-Daure effect. For this discovery he was proposed by C. Fabry for the Nobel Prize in 1929, which was awarded to de Broglie.

the effect was named after him: **Raman scattering**. According to the Rajinder Singh and his work about C.V. Raman [3] there were three reasons why the Russian scientists were not awarded: 1. Physicists from many countries have nominated Raman for the prize, while only two nominated the Russians; 2. Raman published his results earlier than the Russians (who also cited Raman's previous work); 3. Nobel prize committee felt that C.V. Raman results were more universal as they were performed for solids, liquids and gases.

Development

During following years, the research was focused on the phenomenon fundamentals, however due to lack of the technology its development was very slow. Research was at this time focused on both infrared and Raman spectroscopy what has allowed to formulate solid model of vibrational molecule dynamics and created a basis for Raman spectroscopy as a significant scientific tool. Unfortunately, discoveries from that time could not be applied in the research without certain technological progress. The most difficult problem was inelastic scattering detection (very weak compared to the Rayleigh scattering). The breakthrough happened with laser discovery in 1960, which could provide a perfect source of monochromatic light. Another advantage was a possibility to measure a very small volume of the sample ($10^6 - 10^7$ less material than previously). Additionally use of the laser eliminated some of the problems related to the scattered light, improved detection power and allowed this way to analyze low frequency vibrations. Adjusting laser wavelength allowed to avoid problems with occurring for some materials fluorescence and absorption. Starting from 1970 most of the Raman systems were equipped with Ar+ lasers with stable 488 and 514.5 nm lines. Kr+, He-Ne, Cd, Ru laser were also entering the market. Other problem (mentioned already earlier) was elastic scattering, which was very disturbing while looking at the region close to the laser line. This problem was first partially solved by using additional monochromator, but this increased apparatus size and decreased the optical setup efficiency. Recently Raman setups are equipped with notch filers, which allow to decrease the spectrometer size and to increase

its efficiency. Next step was acquiring the scattered light. Until 1970 traditional photographic methods were applied. They were very time consuming but efficient. From this time scientists started using CCD camera, however their efficiency till 1987 was very low. That year a new breakthrough occurred and time dependent spectra acquisition became possible. Last big step was to couple PC computer with the spectrometer.

Applications

Raman spectroscopy is applied to the analysis of many different materials and systems present in our daily life. To list some of these applications, we can see how broad and recognized it is [5]: **pharmaceutical applications** [6] (*e.g.* it gives insight in monitoring and controlling of processes also at the production stage and it enables to control temperature and humidity); **carbon and diamond research** [7, 8] (*e.g.* to see nanotubes hirality); **gemology, geology and mineralogy research** [9] (*e.g.* to verify whether diamonds have been artificially treated at high temperature and pressure); **nanotechnology research** [8]; **art and heritage analysis application** [10] (*e.g.* to allow conservators to understand the original materials (paints, pigments, lacquers etc) in addition to any degradation processes); **semiconductors research** [11] (*e.g.* to monitor stress, and other parameters such as surface/device temperature, make it an effective tool throughout the semiconductor device manufacturing process); **biological and biomedical research** [12] (*e.g.* to distinguish between cancerous, pre-cancerous and normal tissues, and its sensitivity to changes in cell metabolites and protein structures); **forensic sciences application** [13] (*e.g.* it is predominantly used for the unambiguous identification of unknown substances).

Raman effect

Raman effect occurs when a incident light photon (E_0) interacts with crystal lattice phonon, by creating a new phonon (E_0 looses energy) or it adsorbs some energy from the lattice phonon. This results in additional spectra of Stokes (Fig. 2.2a) and

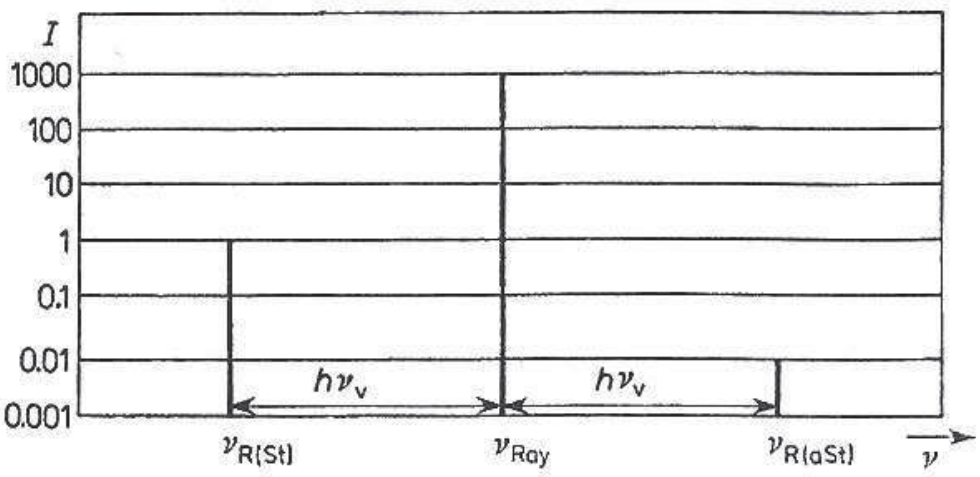

Figure 2.2: Intensities comparison of light scattering (a) Stokes (St); (b) Rayleigh; (c) anti-Stokes (aSt).

antiStokes scattering (Fig. 2.2c) next to the Rayleigh one (Fig. 2.2b). The intensity of inelastically scattered light is less than 10^{-6} of the intensity of incident light (see Fig. 2.2). It is a spontaneous process (T $\propto 10^{-14}$ s).

There are classical and quantum models explaining Raman effect which will be presented below. I will start with the classical one based on the scattering on a molecule (for simplicity). I will use this one oscillator representation, keeping in mind that for a crystal, one has to take n oscillators into account. The out-coming result would be similar to the case presented here.

Classical model

Incident light might be described with equation

$$\mathrm{E(k,}\omega) = \mathrm{E}_0 exp[i(\omega t - \mathrm{kx})] \ , \tag{2.1}$$

where E_0 is incident light electric field; ω is angular frequency; k is a wave vector and x is a position in the crystal. It will cause a polarization of the material. The ionic polarization $\mathrm{P_j}$ is described with equation

$$P_j = \frac{q^2 E_0 e^{i\omega t}}{\mu(\omega_{TO}^2 - \omega^2)} \ . \tag{2.2}$$

In this equation the effective mass μ is defined as $\frac{1}{\mu} = \frac{1}{M_1} + \frac{1}{M_2}$, for our needs this relation will be presented as $P_j = \chi E$, where χ is the electric susceptibility. If we assume that the electro-magnetic wave can induce lattice vibrations, then electric susceptibility will not depend from ion movements. Let us consider what will happen if independent lattice oscillations exist beside electro-magnetic wave. These oscillation through ion vibrations create an additional polarization. This effect can be described assuming that electric susceptibility has two parts: one constant and second induced by lattice vibrations. This leads us to

$$\chi = \chi_0 + \frac{d\chi}{du} u cos(\omega_{fon} t) = \chi_0 + \frac{1}{2}\frac{d\chi}{du} u \left\{ exp(i\omega_{fon} t) + exp(-i\omega_{fon} t) \right\} \ . \tag{2.3}$$

Assuming that electric field intensity for the electro-magnetic wave is described by Eq. (2.1) the polarization relation (Eq. (2.2)) will become

$$P_j = \underbrace{\chi_0 \mathrm{E}_0 exp[i(\omega_0 t)]}_{Rayleigh\ scattering} + \underbrace{\frac{1}{2}\frac{d\chi}{du} u E_0 exp[i(\omega_0 + \omega_{fon})t]}_{anti-Stokes\ scattering} + \underbrace{\frac{1}{2}\frac{d\chi}{du} u E_0 exp[i(\omega_0 - \omega_{fon})t]}_{Stokes\ scattering} \ . \tag{2.4}$$

In Eq. (2.4) beside the ω_0 wave appear two other waves with lower and higher frequencies $\omega_0 - \omega_{fon}$ and $\omega_0 + \omega_{fon}$ respectively, with their intensities proportional to the electric susceptibility derivative $\frac{d\chi}{du}$.

Quantum model

The quantum model can be easily presented as in the Fig. 2.3. Here light scattering has its origin in absorbing the light to the virtual energy state (dash line) and then its spontaneous emission to ground state. As the emission is spontaneous, the virtual state energy can have any value. Existing in crystal a phonon field can cause, that the system being in excited state will absorb or emit phonon at $\hbar\omega_{fon}$. This will result in system energy either $E + \hbar\omega_{fon}$ or $E - \hbar\omega_{fon}$, and thus while relaxing to the ground state three different photons could be emitted

1. $E_{Ray} = \hbar\omega_{photon} = E$

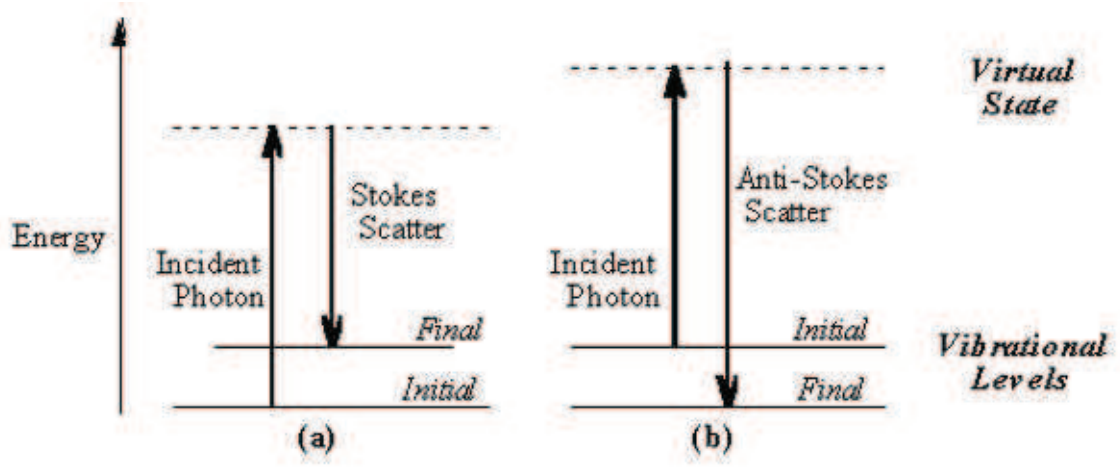

Figure 2.3: Quantum model of Raman scattering.

2. $E_{aSt} = \hbar\omega_{photon} = E + \hbar\omega_{phonon}$
3. $E_{St} = \hbar\omega_{photon} = E - \hbar\omega_{phonon}$

First equation corresponds to the resonance energy and is called Rayleigh line. Photon with the lower energy corresponds to the Stokes line (E_{St}) and with higher energy to the anti-Stokes (E_{aSt}) line.

2.2 Nanowire structure analysis

Silicon nanowires (SiNWs) are expected to be potential candidates for building blocks of future electronics devices and, in consequence, they have recently attracted a significant interest of the solid state community. Several reasons of these expectations can be mentioned. Most of the present-day technology is still based on silicon and SiNWs fabrication is relatively inexpensive, fast and quite well developed. The n-type and p-type doping of the material is possible [14]. That makes the SiNWs a strong competitor to nanotubes in the field of micro- and nonoelectronics. Reported possible applications include field effect transistor [15], biological [16] and chemical [17, 18] sensors, solar cells [19] and light emitting diodes [20].

Methods to determine structure of the SiNW

One of the most common way and at the same time the most precise is **Transmission electron microscopy (TEM)**. This technique can provide information about nanowire crystalline properties, composition and elements distribution. However this technique requires a special sample preparation and is not very well suited for the quick nanowire structure verifying application.

In this part we report a well recognized and fast method of SiNW characterization - Raman spectroscopy. Both intrinsic and doped materials can be studied [14]. The quality of SiNW crystallization, nanowire diameter [21], temperature [22, 23] and thermal conductivity [24] can be withdrawn from Raman scattering spectra. We report the Raman scattering study of the individual conical core/shell SiNWs deposited on the gold surface. Diameter at the base of the nanowires was 400 nm and on the tip 100 nm.

We have observed Raman scattering spectra of single, well separated Si nanowires. The analysis of the spectra shows that in the nanowires a crystalline core exists, surrounded by an amorphous envelope.

2.2.1 Experiment preparation

The cone shaped SiNWs used in our study have been synthesized by CVD (Chemical Vapor Deposition). First the after-growth surface containing SiNW has been immersed into isopropanol or ethanol and agitated 30 seconds in an ultrasonic bath. The resultant solution has been spin coated on a silicon substrate covered with a 1 μm thick Au layer. This procedure enables us to separate and spread the nanowires over the substrate in a rather controlled way (we can control the density of the SiNWs).

As shown in Figure 2.5 the markers have been drawn around the single nanowire to identify the examined objects and to locate them during the micro-Raman experiments. Markers have been created with Ga+ ion etching in the Ti and Au substrate using Focus Ion Beam (FIB) technique.

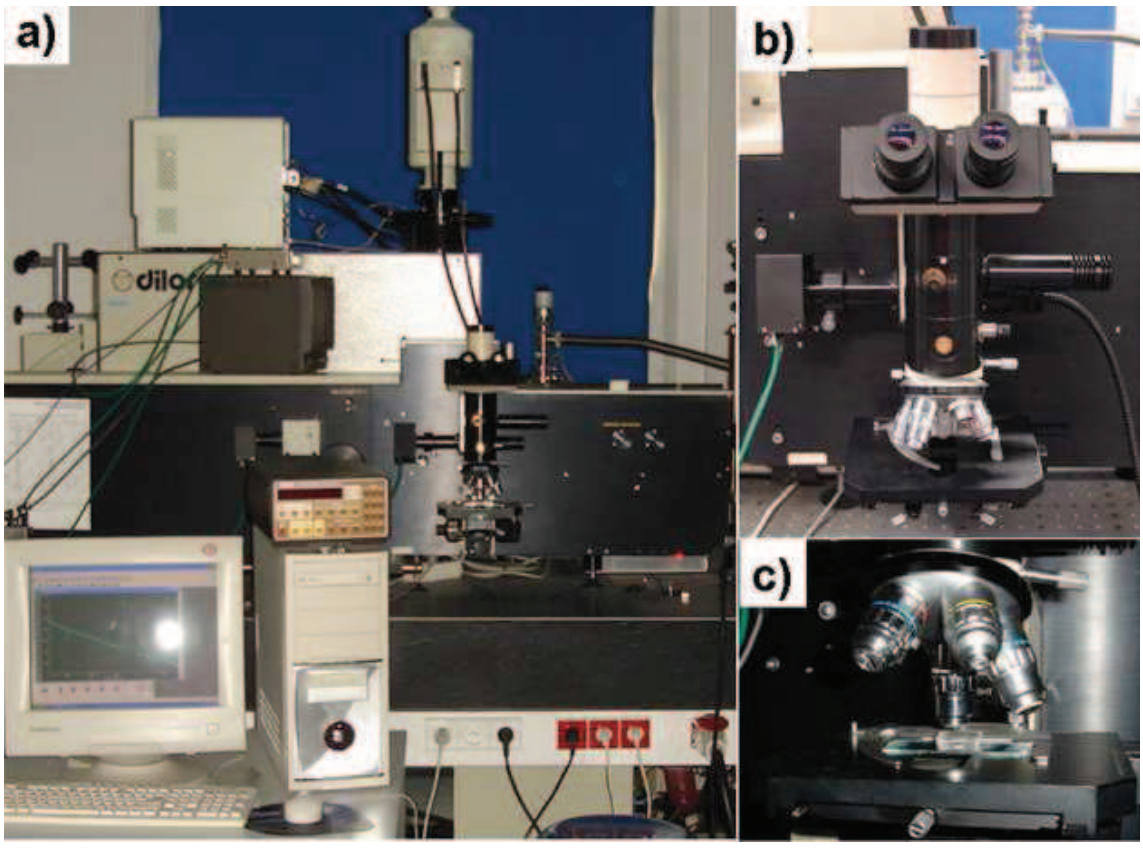

Figure 2.4: (a) Raman Backscattering Spectrometer Dilor XY-800. (b) Optical microscope under which one can see the sample and through which laser beam is focused. (c) Raman table with a sample on it.

2.2.2 Results and discussion

Micro-Raman experiments have been performed at room temperature in ambient atmosphere using Dilor XY-800 spectrometer (see Fig. 2.4). The accuracy of the Raman spectra has been estimated on the $1-2$ cm^{-1} level, depending on the spectral region. Two Kr+ laser lines 647 nm and 482 nm have been used. Raman spectra have been analyzed in three points along the nanowire length: base, middle and tip. The SEM measurements provide us with information concerning the geometrical parameters of the nanowires such as their shapes, lengths, and diameters. The lengths of the examined nanowires were between 5 μm and 15 μm, while their diameters varied from 100 nm to 400 nm. As presented in Fig. 2.5, the CVD synthesis produces straight conical nanowires. This can be seen in the Raman spectra (Fig. 2.6). A narrow peak slightly below 520 cm^{-1} has been observed in a

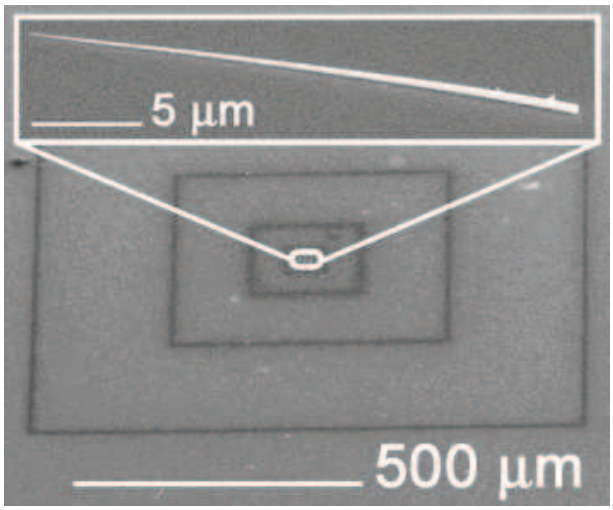

Figure 2.5: **Top** : silicon nanowire grown by CVD and deposited on a 500 nm Au-coated silicon substrate. The nanowire diameter is 100 nm (at its tip) and 400 nm (at its base), and 15 μm long. **Bottom** : marker structures fabricated by focused ion beam (Ga+ ion etching) around the nanowire. This structure allows to find the wire using the optical microscope of Dilor XY-800 backscattering Raman spectrometer (see Fig. 2.4).

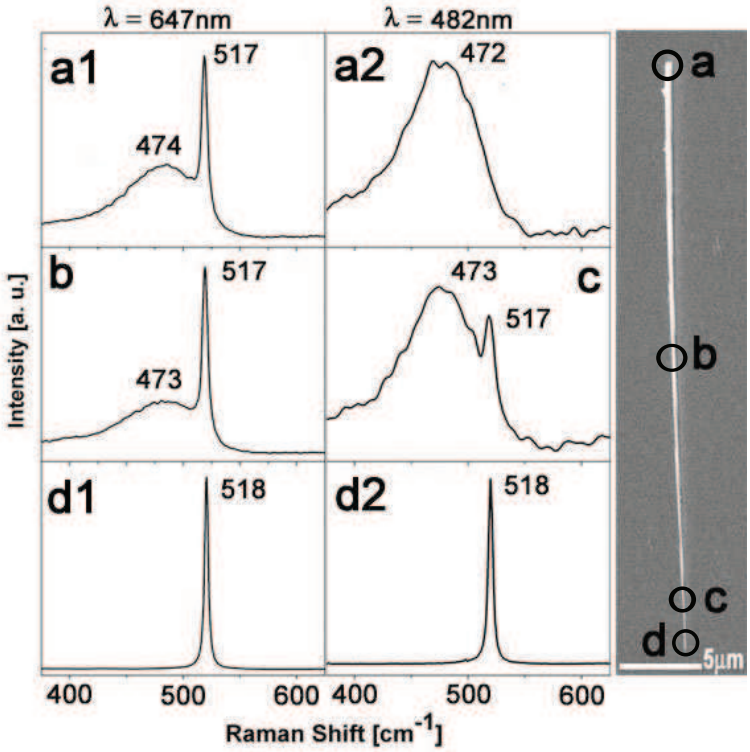

Figure 2.6: Raman spectra from the tree different points along the CVD SiNW for the 647 nm and 482 nm laser lines. The broad peak at 470 cm^{-1} is characteristic of amorphous silicon and is visible along with the LO-TO silicon mode (520 cm^{-1}).

vast majority of our spectra. The peak corresponds to the first order LO-TO peak of crystalline silicon (c-Si). The c-Si peak has been used as a reference point of our measurements - it is the main band of silicon in the Raman scattering (always visible in Si rich materials). We found out that the morphologies of the CVD grown SiNWs are reflected in the Raman spectra. The spectra depend substantially on the position of the light spot on the wire. As presented in Fig. 2.6a (excitation line 647 nm), the Raman spectra taken from the thicker ends of the CVD nanowires basically form a superposition of two peaks. The first one corresponds to the LO-TO peak of crystalline Si; the second broad band basically reflects the phonon DOS of a crystalline Si and can be attributed to the disorder activated phonon modes. This suggests that nanowires are built from a crystalline silicon core and an amorphous silicon shell.

At the thinner end of the nanowire the broad band is practically absent. The crystalline Si peak is downshifted of approximately 2 cm^{-1} in comparison with the thick end peak. The 482 nm Raman spectra are quite similar to the previous ones (Fig. 2.6c). A decay of crystalline Si band already 1 μm from the thin end of the SiNW is visible (Fig. 2.6c middle graph). As mentioned previously the broad peak centered at approximately 470 cm^{-1} coincides with the peak of phonon DOS. It is known, that the activation of the short-wavelength phonon modes is interpreted as due to disorder and dimensional effects [25, 26]. It is possible that, the disorder activated phonon modes responsible for the DOS-like Raman peaks are seen not only due to the finite size of the nanowires but also as a result of the morphology of the object and the interplay between these effects.

We suggest that the measured nanowires are formed of crystalline silicon core surrounded by amorphous silicon (see Fig. 2.7). There is some controversy in literature concerning the direct energy gap of a-Si but it is rather accepted, that for nanoclusters of a-Si its energy gap is higher than the indirect c-Si gap. It strongly depends on the a-Si nanocluster dimensions [26, 27]. In consequence, the amorphous envelope, where the a-Si direct energy gap dominates is more transparent for the red light (647 nm = 1.91 eV) than for the blue light (482 nm = 2.57 eV). The resonance

effects should also be taken into account, hence the amorphous envelope is better seen in the Raman spectra excited with higher energies [†].

2.3 Temperature analysis

Nanowire temperature determination is very important as nanowires have a potential to become a future building blocs in electronics and in power cells based on thermo-electricity effect. Raman spectroscopy enables us to monitor changes almost in real time and also very locally. From this measurements one can obtain additional information about nanowire thermal conductivity[‡].

Raman spectroscopy

The advantage of Raman spectroscopy is that it provides information about local temperature and allows the user to go deeper [§] in the nanowire structure (actually this function has wider application in temperature analysis of coated transistors). In this experiment we have obtained information about temperature distribution which have shown that silicon core is cooler than amorphous silicon shell. The local temperature of the nanowires has been determined from the Stokes/ anti-Stokes intensities (I_S/I_{AS}) ratio and the analysis of the LO-TO 520 cm^{-1} downshift. A good agreement has been observed between these two methods. We explain this effect as caused by poor thermal nanowire conductivity and good silicon core tip contact with metal substrate.

[†]published: Marczak et *al.*"The individual core/shell silicon nanowires' structure probed by Raman spectroscopy" *Physica Status Solidi C*, vol. 6, p. 2053, **2009** [28]

[‡]One of the techniques to measure nanowire temperature is the **thermoreflectance imaging system** giving submicrometer spatial resolution and 0.1°C temperature resolution using visible light [29]. Other approaches are more indirect techniques. The nanowire temperature measurement is determining how the nanowire thermal conductivity changes with the temperature. It is known that with the increase of the temperature, nanowire conductivity will increase (same as in the bulk silicon) [24].

[§]d_p (probing depth of the laser light) depends on the material photo-absorption coefficient α described by the formula: $d_p = 2.3/2\alpha$ [30]

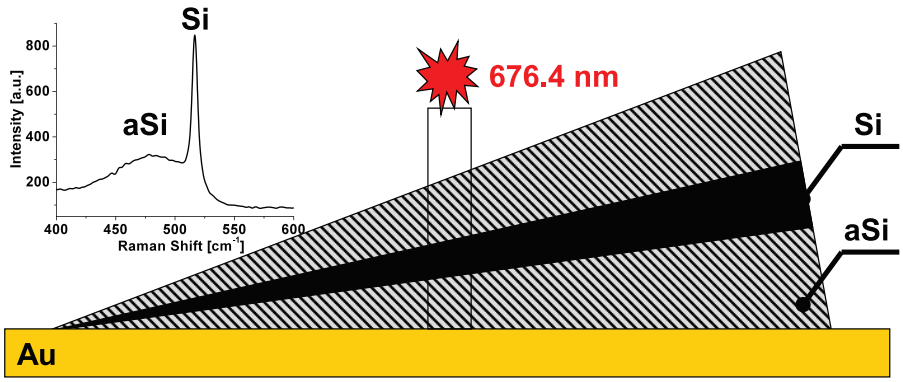

Figure 2.7: Model of the core/shell nanowire. Our results suggest that the nanowire cSi core is in a good thermal contact with the metallic substrate (on the tip we observe only cSi), thus improving the heat evacuation of the SiNW, for which the thermal conductivity is known to be low.

2.3.1 Results and discussion

We have observed that the local temperature of the nanowire core is lower than the shell. We explain this effect by a good thermal contact of the nanowire core tip with the Au surface. On the thick end the silicon core is isolated by an amorphous silicon. Low thermal conductivity of the silicon nanowire core and shell is of importance for the observed effect. Temperatures obtained from Stokes and anti-Stokes (I_S/I_{AS}) ratio (eq. 2.5) and the analysis of the LO-TO 520 cm^{-1} downshift [22] (similar behavior as in Fig. 2.9) indicate presence of warmer ($T_{aSi}\rangle 450\ K$) amorphous cover around a cooler ($T_{Si} \sim 400\ K$) crystalline silicon core [see Fig. 2.8]

$$\frac{I_S}{I_{AS}} \propto e^{\frac{\hbar\omega_0}{k_B T}}\ , \tag{2.5}$$

where I_S and I_{AS} are Stokes and anti-Stokes intensities, ω_0 is a shift of incident light frequency and T is the temperature[¶].

On the thin end in Fig. 2.8c ($T_{Si} \sim 350K$), where almost no aSi is observed, the silicon core temperature stays low. Our results suggest that the nanowire cSi core is in good thermal contact with the metallic substrate (on the tip we observe only

[¶]in regard to prof. dr hab. R. Bacewicz (WUT, Poland) remark: this is an effective temperature, which can differ from the thermodynamic one. This could influence the visible temperature difference, as this equation was used in the same form for both crystalline and amorphous silicon.

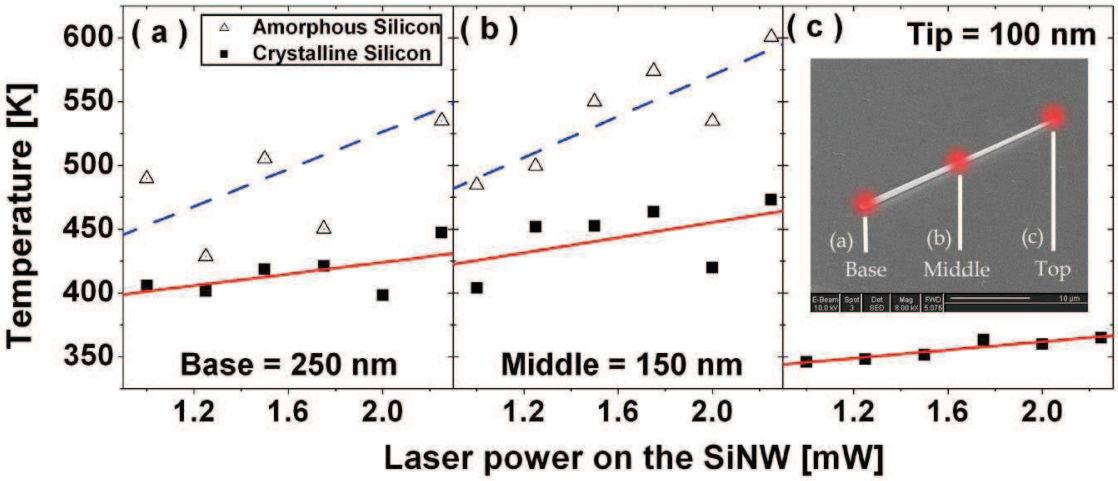

Figure 2.8: Temperatures obtained from I_S/I_{AS} ratio and the analysis of the LO-TO 520 cm^{-1} downshift (λ = 647 nm) indicate presence of warmer ($T_{aSi}\rangle 450K$) amorphous cover (a,b - triangles) around a cooler ($T_{Si} \sim 400K$) crystalline silicon core (a,b - squares). On the thin end (c), where almost no aSi is observed, the silicon core temperature stays low ($\sim 350K$). T_{aSi} and T_{Si} increases with the laser power.

cSi), thus improving the heat evacuation of the SiNW, which thermal conductivity is proved to diminish with diameter [24]. ‖.

Additional experiment was performed to observe a silicon peak position change in function of temperature. Sample was placed in a cryostat (Oxford Instruments) on the hot finger. Temperature could be controlled from 10K to 450K. Experiment was performed first for the silicon wafer (used for calibration) (squares) and then for the silicon nanowires (triangles). A significant downshift of 4 cm^{-1} compared to bulk Si is clearly visible (Fig. 2.9left). This behavior could be explained by already visible nanowire diameter influence on the system as it is reported that already for the nanowire of 100 nm in diameter thermal conductivity drops four time compared to the bulk silicon [29]. This means that size effects can play certain role here. On the Fig. 2.9right full width at half maximum (FWHM) of the peak is presented. Typical FWHM the one for the bulk silicon is visible. This behavior has its reflection in literature [31]. However authors explain their results in means of confinement effects being dominant (their nanowires have diameter below 25 nm).

‖published: Marczak et *al.*"The individual core/shell silicon nanowires' structure probed by Raman spectroscopy" *Physica Status Solidi C*, vol. 6, p. 2053, **2009** [28]

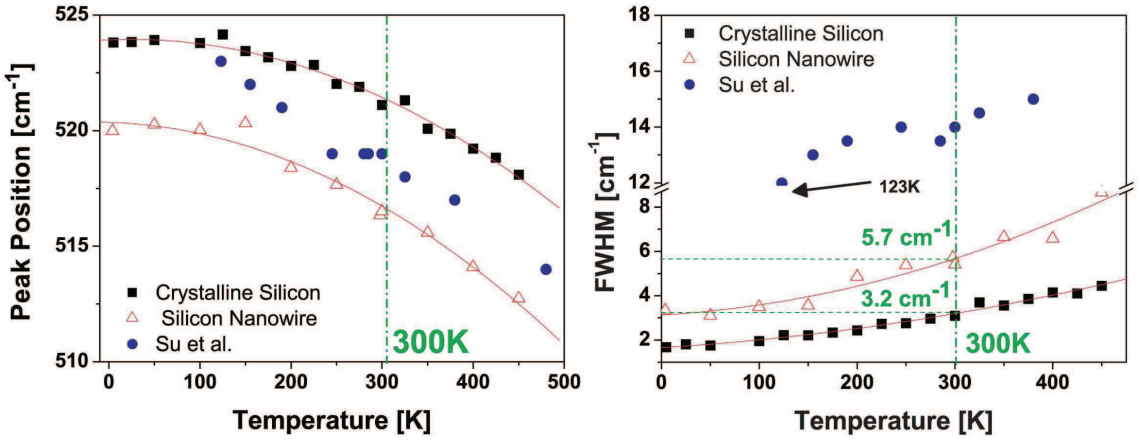

Figure 2.9: Silicon (squares) and SiNW (triangles) LO-TO peak positions and FWHM in function of temperature. A visible shift between SiNW and bulk Si is visible (left) as well as an increase in full width at half maximum (FWHM) (right). This is presented in comparison to nanowires probed by Su *et al.* (circle).

In our case nanowires are still large compared to them.

2.4 Doping analysis

Semiconductors

We can divide materials into three main groups regarding their electrical conductivity σ: metals ($\sigma \geq 10^{-6}$ Ωm^{-1}), semiconductors (10^{-8} $\Omega m^{-1} \leq \sigma \leq 10^{-6}$ Ωm^{-1}) and insulators $\sigma \leq 10^{-8}$ Ωm^{-1} [32].

Semiconductors can be divided to two types: intrinsic and doped ones. In general these are materials that have filled valence band and a band gap of less than 3 eV (in practice it is usually around 1 eV). These materials can have population of holes and electrons coming form thermal excitation causing that both of them contribute to the charge flow. This is an intrinsic semiconductor. To the most important semiconductors belong Si, Ge (from Group IV) and GaAs, InP, GaP (from group III-V). At very low temperature (reaching 4K) there will be no more charge flow under the influence of electric field.

Intrinsic semiconductors

In intrinsic semiconductors the Fermi-level is inside the band-gap of the semiconductor, leading to equilibrium thermal populations of electrons and holes in the conduction and valence bands. For the bottom conduction band of energy E_C we can write the number of electrons in this band ($n_e V$ where V is a volume) as following

$$n_e V = \int_{E_C}^{\infty} D(E) f_{fd}(E)\, dE \ , \tag{2.6}$$

where $f_{fd}(E)$ is a Fermi -Dirac distribution, which we can approximate as

$$f_{fd}(E) \approx e^{\frac{-(E-\mu)}{k_B T}} \ . \tag{2.7}$$

We can also write the energy relation for electrons at the bottom of the conduction band as

$$E = E_C + \frac{\hbar^2 k^2}{2m_e} \ . \tag{2.8}$$

The density of states for the conduction band has a form similar to the one for free electrons case, with exception that the energy zero is at the bottom of the conduction band

$$D(E) = \frac{m_e V}{\pi^2 \hbar^3} \sqrt{2m_e(E - E_c)} \ . \tag{2.9}$$

Now, if we put to Eq. (2.6) previous formulas, we will obtain

$$n_e V = \int_{E_C}^{\infty} \frac{m_e V}{\pi^2 \hbar^3} [2m_e(E - E_c)]^{1/2} e^{\frac{-(E-\mu)}{k_B T}}\, dE \ . \tag{2.10}$$

After simplification

$$n_e = \int_{E_C}^{\infty} \frac{m_e^{3/2}}{2\pi^2 \hbar^3} (E - E_c)^{1/2} e^{\frac{-(E-\mu)}{k_B T}}\, dE \ . \tag{2.11}$$

Solving this by substitution $y^2 = \frac{(E-E_C)}{k_B T}$ we will get

$$n_e = \frac{1}{4} \left(\frac{2m_e k_B T}{\pi^2 \hbar^2} \right)^{3/2} e^{\frac{-(E_C-\mu)}{k_B T}} \tag{2.12}$$

A similar calculation can be performed for holes in the valence band, with exception that for holes instead of f_{fd} we would use $(1 - f_{fd})$

$$n_h = \frac{1}{4} \left(\frac{2m_h k_B T}{\pi^2 \hbar^2} \right)^{3/2} e^{\frac{-(E_V-\mu)}{k_B T}} \ . \tag{2.13}$$

Hence for the intrinsic semiconductor $n_e = n_h$ and by comparing equations (2.12) and (2.13) we can obtain

$$\mu(T) = \frac{E_C + E_V}{2} + \frac{3}{4} k_B T ln \frac{m_h}{m_e} \ . \tag{2.14}$$

Introducing intrinsic carrier density by the formula $n_e n_h = n_i^2$ we can easily calculate n_i for silicon at room temperature $\sim 10^{16}$ m^{-3}.

Doped semiconductor

A way of obtaining more electrons in the conduction band (or holes in the valence band) is doping of the intrinsic semiconductor. If one dopes Si with group V element like phosphorus, it will replace a silicon atom. This will add an extra electron. This electron is weakly bound to the phosphorus and in ambient temperature can easily be excited into the conduction band. In this process, the impurity has donated an electron to the semiconductor. The density of electrons in the conduction band is equal to the density of donors. If the density of donors N_D is much greater that the intrinsic density n_i ($N_D >> n_i$) then clearly $n_e = N_D$. Eq. (2.14) for the chemical potential will take a form

$$\mu = E_C - k_B T ln \left\{ \frac{1}{4N_D} \left(\frac{2 m_e k_B T}{\pi \hbar} \right)^{3/2} \right\} \tag{2.15}$$

For $N_D \approx 10^{22}$ m^{-3} the μ is fraction of eV (0.1 - 0.2 eV at 1000 K) below the conduction band. Following the standard mass-action effect will show that the concentration of holes is negligible ($n_e n_h = n_i^2$). This means that the conductivity will be dominated by the electrons. This type of semiconductor is called **n-type**.

If the intrinsic semiconductor will be doped with elements form the III$^{\text{rd}}$ group (eg. boron) the effect will be opposite. Boron atom will take place of the silicon atom, but one electron will be missing. This will create an extra hole. In effect we have added a negative static charge. At the ambient temperature this hole will enter the valence band. Boron is an acceptor impurity. Similar as in previous paragraph,

the normal doping is determined by the number of acceptors N_A and if we write the expression for chemical potential we will get

$$\mu = E_V + k_B T ln \left\{ \frac{1}{4N_A} \left(\frac{2m_h k_B T}{\pi \hbar} \right)^{3/2} \right\} \tag{2.16}$$

and it will be of order of one eV above the valence band. Again, by mass-action the concentration of electrons in the conduction band and is significantly reduced and because of that the conductivity is dominated by holes. This type of semiconductor is called **p-type** [33, 32].

Methods to determine doping

There are many different methods to measure silicon boron doping. The most common among them are I-V measurements and Femtosecond Laser Assisted Tomographic Atom Probe analysis [34]. The first method is very precise and commonly used and the measurement itself is fast. However you can not re-use the nanowire and the sample preparation is time consuming as it involves few electro-lithography steps. Second method Femtosecond Laser Assisted Tomographic Atom Probe analysis [35] is very precise and provides information about doping and its 3D distribution. Unfortunately, the nanowire preparation is very time consuming and difficult (single nanowire has to be glued to the holder) and nanowire is being destroyed during measurement.

Raman spectroscopy

An answer to these problems is Raman spectroscopy which can provide fast information about grown silicon structure. Additionally, it can characterize operating device.

In Raman spectra of boron doped silicon nanowires one can distinguish two characteristic peaks. First a LO-TO mode around 520 cm^{-1} originating from crystalline silicon (cSi) and second one (sometimes double) at 620 cm^{-1} (and 640 cm^{-1}) originating from boron doping presented in Fig. 2.10. Additionally, the peak from cSi

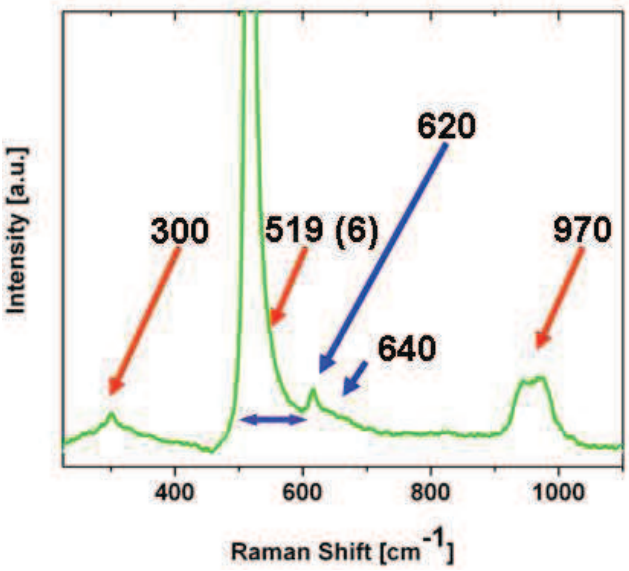

Figure 2.10: Raman spectra of boron doped silicon nanowire. Boron (B) features are visible at 620 and 640 cm^{-1} and in LO-TO mode ($\sim$520 cm^{-1}) asymmetry and broadening (FWHM of 6 cm^{-1}).

shows a certain asymmetry, resulting from boron doping. This has been broadly described in literatures [36, 37] in the case of bulk silicon.

But only one time doping analysis based on Fano resonance is mentioned to be used for silicon nanowires [14]. Its advantage is that it can be used for "as grown" nanowires, what makes it fast and easy method. Its drawback is low sensitivity to doped materials below 10^{19} atoms/cm^3 and very low sensitivity to n-type silicon. This method is based on observation, in boron doped silicon, of the interference between discreet phonon Raman scattering and continuous electronic Raman scattering. This effect is related to Fano resonance [21] and is described by the formula

$$I(\omega) = A\frac{(q+\epsilon)^2}{1+\epsilon^2} \tag{2.17}$$

where A is intensity coefficient; $\epsilon = \frac{\omega-\omega_0}{\Gamma}$ (ω_0 is peak frequency and Γ is peak width); most important element of this equation is asymmetry parameter q. The smaller the q is the bigger the asymmetry is (see Fig. 2.11). Fano parameters for silicon are well known and grouped in the work of Cerdeira *et al.* [36] and parameters are reproduced in Fig. 2.12. One can clearly see for the same boron concentration a difference of q and Γ parameters for various laser wavelengths.

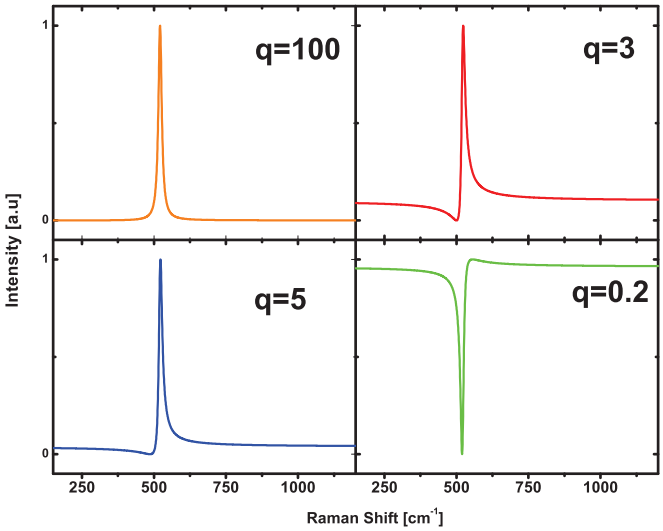

Figure 2.11: Calculated evolution of a Fano line. The bigger the q parameter, the more symmetrical LO - TO the peak becomes (it approaches Lorentzian line).

TABLE I. Parameters obtained by fitting experimental first-order Raman spectra of p-type Si at $T = 77$ K with the Fano lines shape of Eqs. (2). The spectra were obtained with two different laser lines ($\lambda_L = 4880$ and 6471 Å). The values of η are computed for $\lambda_L = 4880$ Å.

$10^{-19} N$ (cm^{-3})	q		Γ (cm^{-1})		$\delta\Omega$ (cm^{-1})		$\eta = (\Gamma^3 q^2)^{1/5}$ ($cm^{-3/5}$)	$\beta = \frac{q(4880)}{q(6471)}$
	$\lambda_L = 4880$ Å	$\lambda_L = 6471$ Å	$\lambda_L = 4880$ Å	$\lambda_L = 6471$ Å	$\lambda_L = 4880$ Å	$\lambda_L = 6471$ Å		
0.6	32.8	18.4	1.1	1.2	−0.1	−0.1	6.6	1.8
1.7	12.4	6.7	2.8	2.8	−0.4	−0.4	5.0	1.8
2.6	14.6	6.4	3.2	3.2	−0.1	0.0	5.9	2.3
4.0	9.8	4.3	4.4	4.4	−1.1	−1.2	6.0	2.3
7.0	4.7	3.1	6.2	5.9	−1.8	−1.9	5.6	1.5
16	3.7	1.4	8.1	8.1	−6.7	−6.5	5.9	2.6
40	2.8	0.4	10.5	10.7	−14.7	−14.7	6.3	7.0

Figure 2.12: Values of q and Γ determined from measurements for bulk boron doped silicon by Cardeira *et al.* [36].

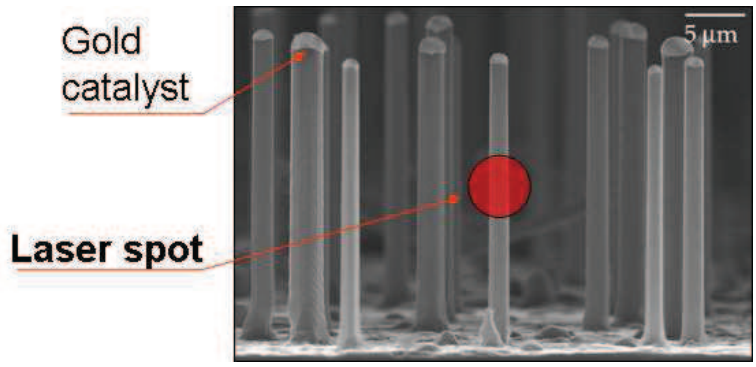

Figure 2.13: A piece of surface with as grown boron doped silicon nanowires is placed in a holder perpendicular to the laser beam (red circle).

2.4.1 Experiment preparation

A surface with "as grown" silicon nanowires as shown in Figure 2.13 is placed in a special holder perpendicular to the laser beam. Nanowire were grown using Chemical Vapor Deposition (CVD) which resulted in up to 250 nm in diameter and up to 8 μm of length. This is described in details in chapter one. Nanowires used here are different from the ones in the previous section. These nanowires are slightly conical and there is no aSi in the structure. Instead they are doped with boron what is clearly expressed in the spectra. Experiment was performed in ambient conditions using LABRAM Dilor Raman Spectrometer using Ar+ laser **. The wavelengths of 638.2 nm and 514.5 nm were used. The resolution of the spectrometer is 1 cm^{-1} and the laser spot size is $\sim$ 1 μm.

2.4.2 Results and discussion

Experimental results are shown in Fig 2.14 clearly showing the asymmetry of the peak. The LO-TO line is downshifted to 516 cm^{-1} for the green wavelength excitation (514.5 nm). The fitted Fano width and asymmetry parameters are Γ=7 and q=6.9, respectively. For the red wavelength excitation (632.8 nm) the LO-TO line is downshifted to 517 cm^{-1} and the fitted Fano width and asymmetry parameter are Γ=6 and q=3.2, respectively. If we compare these obtained fit parameters to

**collaboration with E. Pichnonat (LASIR, USTL)

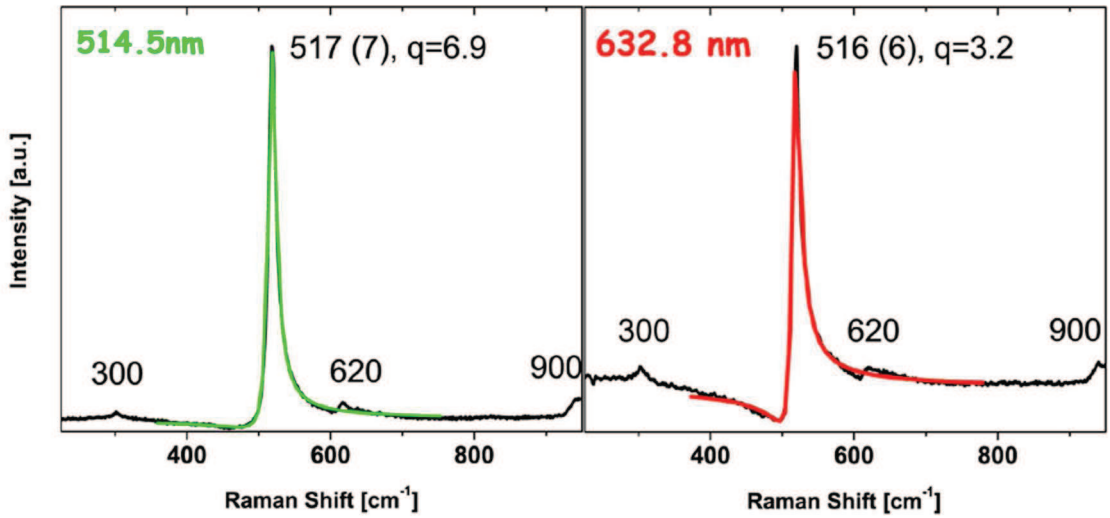

Figure 2.14: The LO-TO mode of silicon is visible. A Fano line fit to the LO-TO mode of a doped silicon nanowire for two laser lines: 514.5 nm and 632.8 nm. The LO-TO line is downshifted at 516 cm^{-1} for the green wavelength excitation (514.5 nm) and the fitted Fano width and asymmetry parameters are Γ=7 and q=6.9. For the red wavelength excitation (632.8 nm) the LO-TO line is downshifted at 517 cm^{-1} and the fitted Fano width and asymmetry parameters are Γ=6 and q=3.2.

the one obtained by Cerdeira *et al.* [36] we can deduce the doping level. The easiest way is to plot measured and fitted with the Fano line points as **q** vs. Γ (see Figure 2.15) we will see that the results are perfectly between values obtained for bulk silicon. On this basis we can claim to have the doping level at 10^{19} cm^{-3}. Next we have measured the spectra along the nanowires in three points (base, middle and tip). It was interesting to see that the doping is increasing toward the nanowire tip as the q parameter decreases and Γ increases. We look for the explanation of this fact in the growth process. Boron atoms will incorporate themselves in the nanowire structure during the growth process. The silicon structure comes form the over-saturated droplet and as the diameter of the nanowire decreases the boron concentration should be higher at the nanowire base. But as the whole process occurs at the high temperatures the doping migration toward the less doped substrate can occur, causing the effect that was observed.

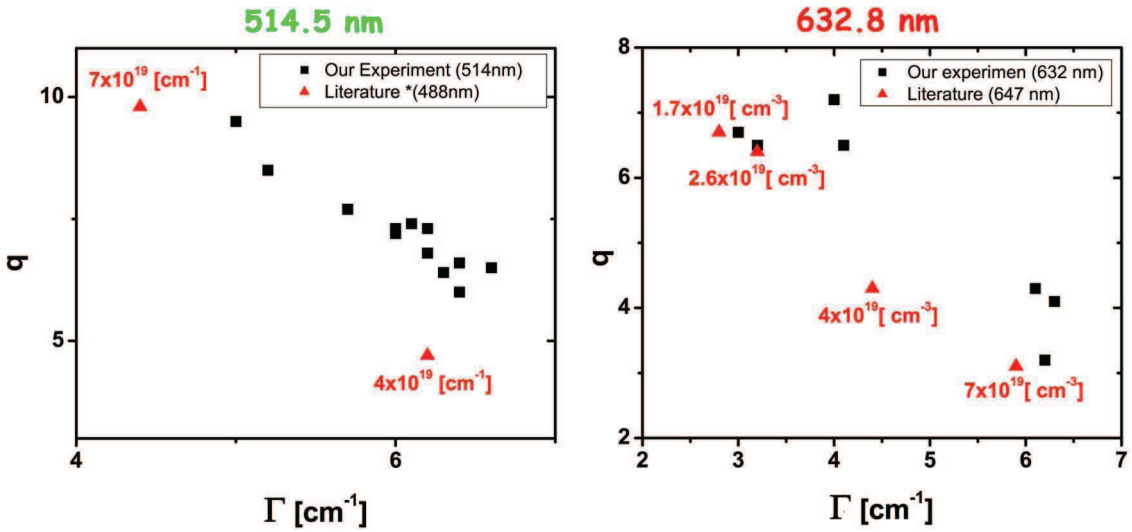

Figure 2.15: Plotted values of **q** vs Γ. Values in red correspond to the literature and points in black come from our experiment. Estimation of doping level give: 2×10^{19}.

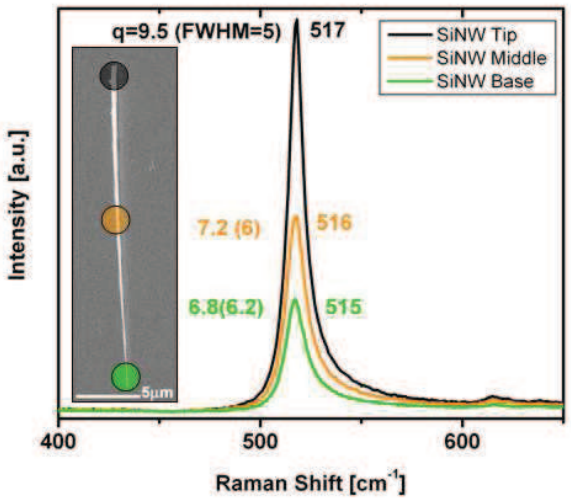

Figure 2.16: Boron doping is increasing towards silicon nanowire tip (q is increasing and Γ - decreasing).

2.5 Conclusions

In this chapter I presented results of measurement of Raman scattering spectra for single, well separated Si nanowires. The analysis of the spectra shows that the nanowires are crystalline, but surrounded by an amorphous envelope. A crystalline Si core is surrounded by an amorphous envelope. The local temperature of the nanowires has been withdrawn from the I_S/I_{AS} ratio and from the analysis of the LO-TO 520 cm^{-1} downshift. A good agreement has been observed between these two methods. From the Raman spectra we have obtained information on nanowire morphology (crystalline silicon core in amorphous sheath) and temperature distribution which have shown that silicon core is cooler than amorphous silicon shell. We explain this effect as caused by poor thermal nanowire conductivity and good silicon core tip contact with metal substrate. Additionally boron doped silicon nanowires were investigated. Using Fano resonance fit and comparing its parameters with bulk doped silicon, the Boron concentration in the nanowires was determined at 10^{19} cm^{-3}. This chapter has shown how universal, easy and fast Raman spectroscopy tool can be. It can provide, maybe not the most, accurate information, but it is sufficient to decide whether grown nanowires are good or not, whether expected parameter were achieved or not. On this basis further more complicated and time consuming measurements can be performed without risk that the material is of low quality.

Chapter 3

Dielectrophoresis

The objective of using dielectrophoresis in this thesis is the development of a method producing structures with nanometric feature size characteristic of nanowires and suitable for large scale assembly. Manipulation of nanowires can be used in sample preparation to gain further knowledge about their fundamental properties. On the other hand, the behavior of the nanowire such as its dielectric response is the key to novel assembly, manipulation or separation techniques. This interaction makes the two research topics suitable for integration into one joint project.

We shall focus on a post-growth process in contrast and complementary to approaches such as directed growth by arrangement of catalytic precursors or applying electrostatic fields during growth. Electrostatic trapping of nanowires onto a previously fabricated electrode array does not satisfy these requirements since neither the repetition rate nor the feature size can be better than that of the pre-patterned support. The expected solution is a continuous process. If electrostatic forces are to be involved rather than moving parts, the technique of choice is travelling field dielectrophoresis since this approach can assure the continuity of the process by conveying the oriented nano-objects across a device with re-entering channel. Handling of nano-objects, i.e. aligning and spacing them equidistantly, in a perpetuous process, not only allows mass producing of nanowire electronic devices but also has potential applications in other branches as composite or optical materials research

and fabric industry, since many novel materials can be synthesized in fiber shape and appropriate assembly methods contribute even more functionality.

For aligning needle shaped objects and assuring the continuity of the process, it appeared obvious to us that different force components had to be put into competition to each other, *e.g.* static electric fields or their gradients to rotate the object to the desired orientation, and propagative forces to eject the aligned objects and supply the manipulator device with fresh material. These competitive steps can be performed simultaneously or in alternance. Concerning the propagative aspect, it is a priori possible to exert these force onto the nanoobjects directly or onto the liquid carrier. The latter is done here, since particles with the desired sizes much smaller than electrodes risk to be trapped as will be shown later.

In section 3.1, the state of the art of dielectrophoresis particle handling and electrohydrodynamic or osmotic liquid pumping is presented. In section 3.2, a completely new approach of microfluidic pumping is suggested: the role of a particle to which travelling wave dielectrophoresis is applied is now attributed to the liquid contained in a microchannel with different complex dielectric function. It is shown that the roles of a particle in liquid environment can be inversely applied to a liquid volume in solid environment to build a new micropump. The theoretical demonstration is provided by decomposing the device into unit cells described by an RC model.

Liquid pumping itself is very important in the success of Lab-on-chip technology [38] that depends on further miniaturization [39], dense integration and cost efficiency of devices that manipulate and analyze liquid matter [40, 41]. Key issues are pumping [42, 43], dosing [44] or sorting [45, 46] of different substances. Liquid pumping without moving parts by traveling electric fields dates back to nineties when Hagedorn [47, 48] demonstrated an electrohydrodynamic (EHD) micropump. The two mechanisms most often involved in lab-on-chips systems are EHD and traveling wave electro-osmotic (TWEO) pumping. EHD setups are based on electric shear forces [49, 50], requiring a conductivity gradient of the liquid and frequencies near the dielectric relaxation frequency of the (slightly) conductive liquid to introduce

the phase shift between the medium polarization and the applied field necessary to exert a force. At steady state, an equilibrium is established between viscous and electrostatic shear forces, leading to the typical velocity profile with a maximum between the electrode array and cover plate. TWEO [51, 52] depends on the formation of a double layer above the electrode array, leading to drag forces onto the ions at the interface in the propagating field.

The approach of this part of work is the application of the dielectrophoresis particle handling technique in a propagating field [53] to a liquid volume: instead of applying a force to a particle with a dielectric constant different from its surroundings, traveling wave dielectrophoresis should inversely be able to apply a force to a liquid with a complex dielectric constant different from the surroundings by attributing the former role of the particle to the liquid volume. Although in the case of a re-entrant channel, the usual formalism consisting in treating the object as ellipsoidal body and obtaining its polarization by the Clausius-Mosotti equation as described for example by Hughes [53] cannot be applied here, it follows from exchanging the roles of particle and liquid volume that it should be possible to apply dielectrophoretic forces to pump liquid in a channel without relying on one of the previously mentioned mechanisms.

In this work, we demonstrate a microfluid pumping device consisting of interdigitated electrode combs buried below an insulating layer to generate a traveling field in a microchannel. This device distinguishes itself by operating mode that exerts a force on the channel volume independently of a conduction gradient [50], inherent media dispersion and double layer effects [49, 54], and its interpretation by decomposing it into an RC model.

The operating range in terms of relation between the operating frequency below 1 MHz and the microscopic dimensions of the device corresponds to the quasi-electrostatic limit, meaning that the channel does not propagate electromagnetic waves as a hollow microwave guide does. The device produces the necessary phase lag between the applied field and the polarization of the liquid by structural dispersion due to the dielectric electrode coating and the conductivity of the ionic liquid.

Inherent media dispersion is not involved, allowing the operating frequency to be chosen far below the dielectric relaxation frequency of the liquid and consequently to handle liquids of higher conductivity than the EHD approach.

For analytic modelization, the traveling wave electrode array is decomposed into a rudimentary RC model, with the resistance corresponding to the liquid conductivity and the capacitance to the dielectric electrode coating. Analytical treatment not only allows estimating the relation between the dielectric properties and the frequency of the applied four-phase signal to maximize pumping force, but also shows that this condition coincides with the observation of cross-over of the impedance measured between electrode combs. This is confirmed experimentally. On one hand, the analytic approach fills a gap between precise numerical simulation [55, 56, 57, 58, 59, 60] and the trial and error methods frequently observed in experimental implementations. On the other hand, it is demonstrated that the use of impedance spectroscopy for monitoring the matching of the frequency and liquid conductance can trigger a whole new generation of devices: if used in alternance with pumping, the impedance feedback not only allows correcting tolerances in device fabrication and liquid preparation, but can also be used for compensating time dependent fluctuations in real-time, assuring continuous optimized pumping power. Previous works [54, 61, 62, 63] have used impedance spectroscopy in combination with dielectrophoresis only to measure the impedance of cells trapped in the channel of a DEP device, but not as a means of maximizing the dielectrophoretic pumping force.

In section 3.3, the micropump is applied to a nanowire suspension. Direct forces of the electric field now do also act onto the nanoobject, creating a competition to the viscous drag forces experienced in the moving liquid. Three different modes of operation depending on the frequency range of the supply voltage can be distinguished and their use in the overall nanowire handling process are suggested.

Section 3.4 summarizes the results and conclusions.

3.1 Introduction

From the previous chapter we have learned how and why nanowires are important as building blocks. However to get access to all their properties various manipulation techniques have to be developed, which will depend on nanowire applications. Some alignment techniques are perfectly suited for local measurements of single structures but a real challenge is a large scale nanowire assembly. The best technique would be **(a)** a **direct growth** on the desired surfaces conserving one direction of growth as illustrated in Figure 3.1 (part of my work) showing the direct growth of aligned nanowires parallel to the surface, and orthogonal to two walls. However this requires good understanding of the growth conditions and surface preparation. Solution to the first part is already presented in the work of Hourlier *et al.* [1] where well aligned silicon nanowires are grown on $\langle 111 \rangle$ silicon surface. However technologically this is a complicated process as it involves targeted gold deposition what is a main drawback of this technique. This technique will be presented in detail in the chapter 4. There is a variation of this technique called deposition on prepatterned substrate [64], which allow to prepare the substrate using silicon nitride mask and silicon oxide etching in a way to have controlled nanowire growth. Although authors claim this technique to be easy, traditional methods developed by Hourlier *et al.* [1] seem to

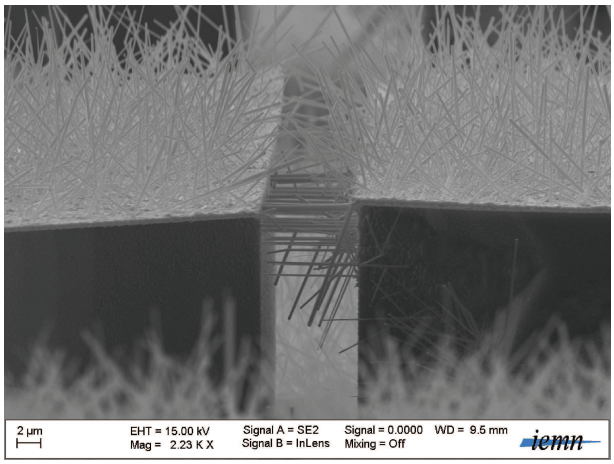

Figure 3.1: Silicon nanowires grown between walls parallel to the surface. Gap between walls: 8 μm.

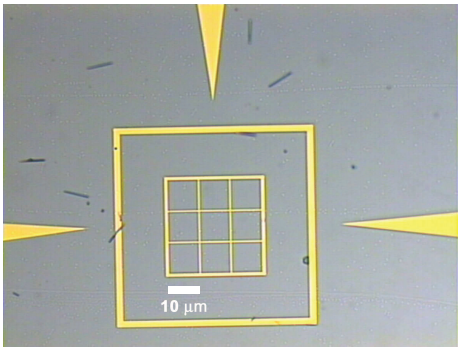

Figure 3.2: Optical microscope picture of silicon nanowires deposited from the ethanol suspension. Random localization is clearly visible. Golden pattern serves here as a marker.

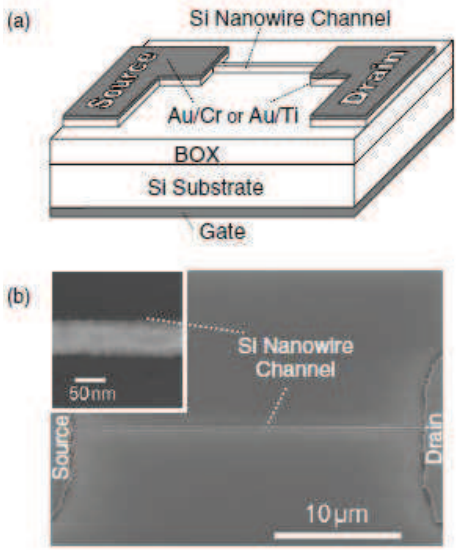

Figure 3.3: (a) Schematic diagram of the SiNWFET. (b) Scanning electron microscopy (SEM) images of the nanowire channel.

be more efficient. However it is very interesting approach. Next approach only for single nanowire devices is **(b) from suspension deposition**. A piece of substrate with nanowires grown with technique (a) is immersed in few ml of alcohol (typically ethanol or isopropanol - the first one is however better as the boiling temperature is lower - 70°C). Next the solution is ultrasonificated and a droplet of a such solution is deposited; nanowires will spread and deposit randomly on the surface like shown in the Figure 3.2 or 3.3 in work of Koo *et al.* [65]. Here we can align the device electrodes with respect to single nanowire using lithography techniques. One of

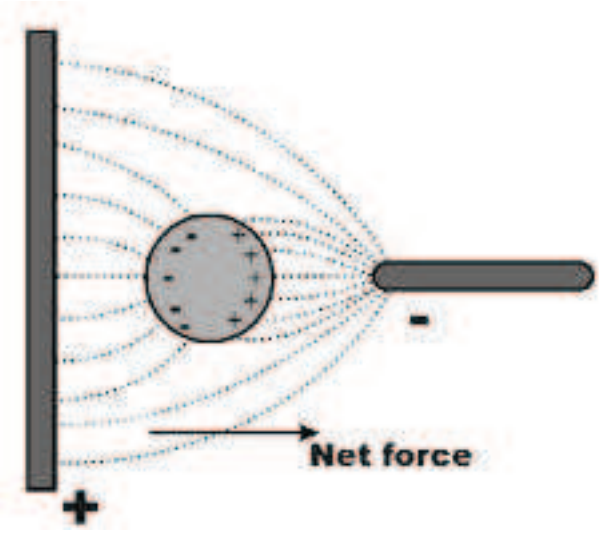

Figure 3.4: Dielectrophoresis: A dielectric object in dielectric medium exposed to the external inhomogeneous electric field.

the big advantages of this method is a very fast access to the nanowire (eg. one can easily deposit metallic electrodes on the SiNW ends and measure an I-V or a transistor characteristics). However this technique is limited to single objects, with no possibility of using it on the large scale. Another difficulty is to have nanowires at the desired place because deposition is random. To improve this technique one can use **(c) manipulation by AFM in contact mode**. Although time consuming this can provide desired results (see [66]). This brings us to the most interesting and most commonly used deposition technique **(d) dielectrophoresis (DEP)**. This phenomenon was first described by Pohl [67] in 1978. In general DEP is defined as the motion of uncharged dielectric particle caused by a polarization effect in a non-uniform electric field. There are two kinds of DEP forces depending on medium ϵ_m and particle ϵ_p permittivities: 1. Positive DEP where $\epsilon_p > \epsilon_m$ particles are attracted to regions of stronger electric field and 2. Negative DEP: $\epsilon_p < \epsilon_m$ where particles are repelled from region of stronger electric field. This is well illustrated on the Fig. 3.4. The net force acting on the particle (for a spherical object of diameter a) will be described by the equation

$$\vec{F} = 2\pi a^3 \epsilon_m f_{CM} \nabla |E|^2 \ , \tag{3.1}$$

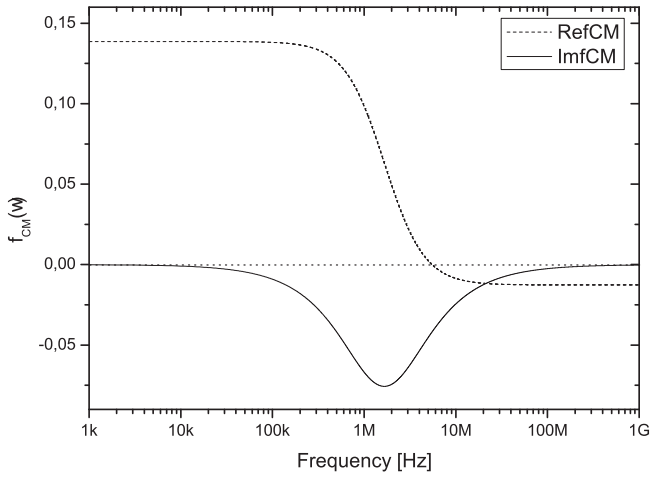

Figure 3.5: Real and imaginary part of Clausius-Mosotti factor vs. frequency.

where $f_{CM} = \frac{\epsilon_p^* - \epsilon_m^*}{\epsilon_p^* + 2\epsilon_m^2}$ is a Clausius-Mosotti factor and $\epsilon^* = \epsilon - j\frac{\sigma}{\omega}$ is a complex permittivity, where ω is an angular frequency. The fact that the permittivity is frequency dependent can be used in switching between positive and negative mode, only by adopting frequency. If we create a traveling field $E(x,t) = E_0 \exp i(kx - \omega t)$, by building an array of interdigitated electrodes (like in the Fig. 3.11) we will get a travelling dielectrophoresis effect. In such system on the spherical particle in a medium will be acting two forces: trapping and propagating ones. First one will be proportional to the real part of Eq. (3.1)

$$\vec{F}_{trap} = 2\pi\epsilon_m r^3 Re(f_{CM}) \nabla E_{rms}^2 \tag{3.2}$$

and the second one to the imaginary part. In propagation direction it will take form of

$$\vec{F}_{prop} = \frac{8\pi\epsilon_m r^3}{\lambda} Im(f_{CM}) E_{x,rms}^2 \ . \tag{3.3}$$

If we plot real and imaginary part of f_{CM} vs. frequency (Fig. 3.5) we see how important frequency is and that the pumping depends only on the complex part of f_{CM}.

Static form of dielctrophoresis allows to deposit silicon nanowires form solution like I did in my testing devices. It will be used in chapter 4 for device preparation.

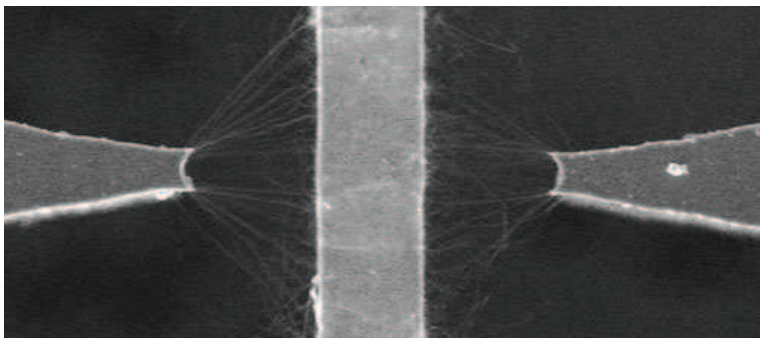

Figure 3.6: Electric-field assisted growth and self-assembly of intrinsic silicon nanowires by Englander *et al.* [69].

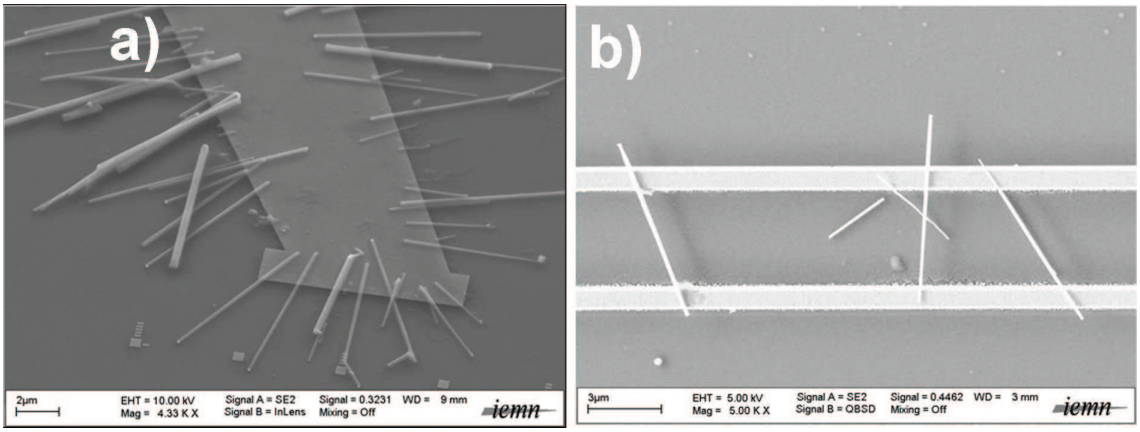

Figure 3.7: (a) SiNW deposited on one electrode, alignment trend perpendicular to the electrode is well visible. (b) SiNWs deposited between two thin electrodes.

Figures 3.7b and 3.8 present the nanowires deposited using dielectrophoresis. One can see them very well aligned between electrodes. This method is very common nanowire deposition technique also including active fluid flow over electrodes [68]. A variation of this technique is electrostatically directed growth [69]. In this technique electric-field assisted growth and self-assembly of intrinsic silicon nanowires is visible (see Fig. 3.6).

One can see them very well aligned between electrodes 3.7b and additionally the nanowires can be suspended 1 μm over the surface (see Fig. 3.7 and 3.8c). To avoid SiNWs detaching from surface a top metalization was performed (see Fig. 3.8b) [for more details see chapter 4]. This technique is very promising and widely used by other groups [70, 71]. In chapter 4, in which I will describe how it can be

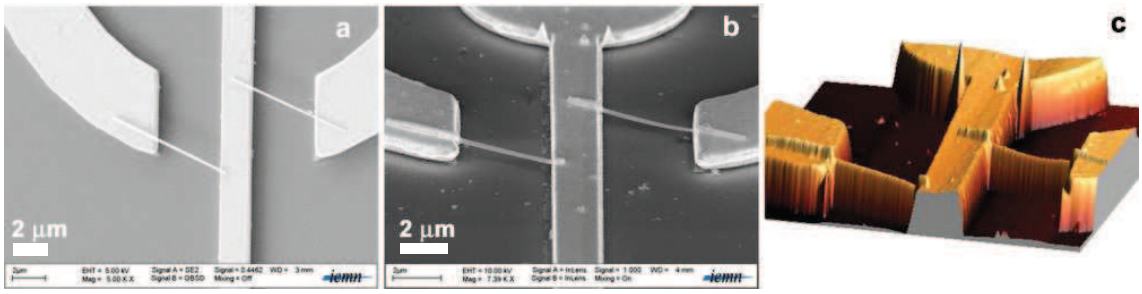

Figure 3.8: SEM image of silicon nanowires deposited on the metallic electrodes (a). They are suspended 1 μm over the surface. (b) after first metalization to ensure that nanowires will stay on the surface and (c) 3D AFM image of the suspended nanowires.

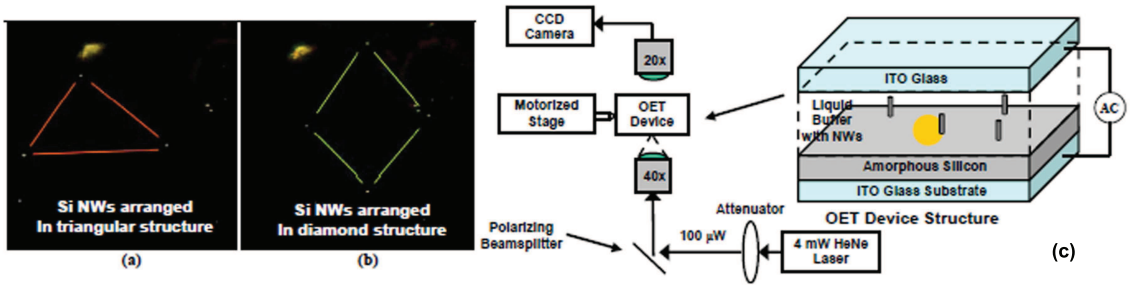

Figure 3.9: Arrangement of silicon nanowires into (a) a triangular structure (b) a diamond structure. Silicon nanowires were aligned vertically with the electric field. The white dots in the background are the wires that have adhered to the surface of the OET chip (c). [72]

used to build suspended electrical or electromechanical devices. A very interesting combination of this technique with laser for single nanowire manipulation (d) was shown by Jamshidi et at. [72] called - optoelectronic tweezers. There nanowires move toward an illuminated area. The maximum speed reported by the authors was 68 μm/s. Silicon nanowires of 100 nm diameter, 5 μm length, and 10^{16} cm^{-3} boron doping were diluted in a 1.6 μS/m conductivity solution of DI water and KCl. The arrangement of nanowires in a triangular structure and diamond structure' is shown in Fig. 3.9ab In this process, the nanowires are maintained vertically by and ac field, while the tweezers are used to move the nanowires. The set-up schema is presented in Fig. 3.9c.

The examples presented above (Fig. 3.2) show that dielectrophoresis seems to be possible answer to the challenging question of large scale assembly raised at the

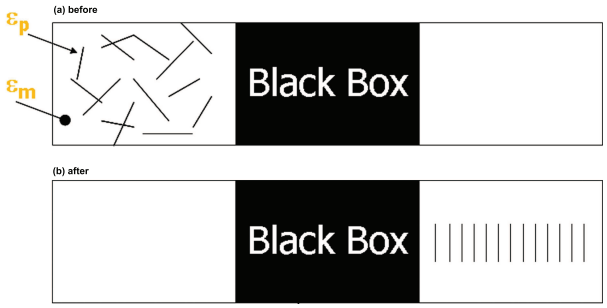

Figure 3.10: Nanowire alignment blackbox principle. On figure (top) nanowires are randomly oriented in a solution before passing through the blackbox (bottom) nanowires form an array of aligned nanowires.

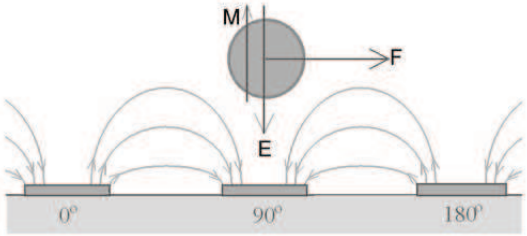

Figure 3.11: Traveling dielectrophoresis. An array of interdigitated electrodes creates a traveling field. On the object will be acting trapping (F_{trap}) and propagating (F_{prop}) forces.

beginning. However the aim is to improve and to simultaneously align and to move nanowire. It can be well illustrated using a Blackbox example (see Figure 3.10), where at image (a) are shown randomly located nanowires in the liquid. After turning on the device, nanowires leaving the box are aligned (b). First, a device to pump the liquid had to be develop, to which first part of this chapter will be devoted. In the second part nanowires will be added to the liquid and pumping of the nanowire suspension will be performed.

3.2 Liquid pumping

This section* will be divided to the following subsections: First in section (3.2.1) I will write about out of phase media polarization, attribution of the former particle role to a liquid volume, next in section (3.2.2) I will proceed to RC network of the

*collaboration with H. Diesinger (IEMN)

cell. In section (3.2.3) I will present a detailed model including parasitic reactive components, experimental approach to the determination of these component values and I will follow in section (3.2.4) to the experimental techniques and in section (3.2.5) to spectroscopy of the cell impedance. A the end I will present in section (3.2.6) a movie sequence presenting liquid pumping.

3.2.1 Principle of DEP pumping: out of phase media polarization

In particle handling by dielectrophoresis, an inhomogeneous field causes a polarization of a particle and at the same time of the surrounding medium [67, 73, 74]. Since the permittivities and conductivities of both materials are different, the polarization will differ, resulting in an Archimedes-like force acting on the body in the water: the particle is pushed to or repelled from the field maxima. The idea of traveling field DEP (TWDEP) originates from linearized electro-rotation [47] and consists in replacing the static field gradient by the dynamic one associated with a propagating sinusoidal field. In asynchronous TWDEP, the particle speed can be neglected with respect to the motion of the traveling wave, and the particle polarization is partly out of phase with the electric field of the traveling wave, resulting in a continuous net mean force in the propagation direction.

Following the approach of inversed roles, the objective is the pumping of liquid by polarizing it with a phase difference relative to an applied traveling field to exert a net force on the liquid. This is possible if the liquid has a complex dielectric response. In the frequency range that can easily be applied to a microarray and that we intend to work with, $f \leq 1$ MHz, ionic liquids are well described by a bulk dielectric constant consisting of a static term ϵ' and a conductivity σ:

$$\epsilon_{liq} = \epsilon' + i\epsilon" = \epsilon' + \frac{i\sigma}{\omega} \tag{3.4}$$

If the liquid (or other conductive material described by this model) is exposed

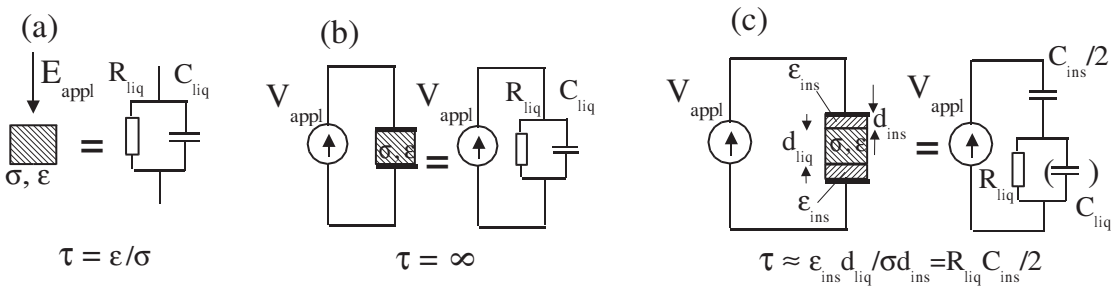

Figure 3.12: Dielectric relaxation: (a) conductive material (*e.g.* ionic liquid) exposed to a constant, homogeneous electric field, (b) same material in contact with conductive plates, (c) same material between conductive plates covered by an insulator.

to an electric field E_{appl}, as in Fig. 3.12(a), the field inside the liquid volume is determined by the Fresnel law (equal dielectric displacement on both sides of the interface):

$$E_{liq} = E_{appl}\frac{\epsilon_{ext}}{\epsilon_{liq}} = E_{appl}\frac{\epsilon_{ext}}{\epsilon' + i\frac{\sigma}{\omega}} = E_{appl}\frac{\frac{\epsilon_{ext}}{\epsilon'}}{1 + i\frac{1}{\omega\tau}} \ . \tag{3.5}$$

This shows that the polarization of the liquid is subject to decay with a time constant τ: the build-up of an accumulation layer at the interface screens the polarization inside the material, but the establishing of the accumulation layer is governed by the dielectric relaxation time constant $\tau = \epsilon'/\sigma$. The relaxation effect can give rise to a polarization with a phase shift relative to the applied field. The same time constant would be obtained as $\tau = R_{liq}C_{liq}$ if the liquid volume was considered as a RC parallel circuit consisting of the resistance and capacitance R_{liq} and C_{liq} respectively. This can be written as functions of the physical dimensions d_{liq} of the liquid volume and its surface A if calculated in the plane geometry, and its static dielectric constant ϵ', and its conductivity σ:

$$R_{liq} \approx \frac{d_{liq}}{A\sigma} \ , \tag{3.6}$$

$$C_{liq} = \frac{A\epsilon'}{d_{liq}} \ . \tag{3.7}$$

This RC element has a crossover frequency typically of 200 MHz, too high to apply with conventional cabling.

Fig. 3.12(a) and Eq. (3.5) describe the situation where the liquid volume is exposed to a given homogeneous electric field. In practice, the electric field must be applied by nearby electrodes supplied with a certain voltage whereas the electric fields across the setup are unknown. Fig. 3.12(b) shows the configuration where the liquid is in contact with the conductive electrodes. In this case, the field screening accumulation layer cannot build up since the ions react at the electrodes rather than accumulating. In the range of validity of this simple model of the complex dielectric constant where the RC equivalent circuit applies, a setup with conductive electrodes in contact with the liquid consequently cannot polarize the liquid with an out-of-phase component relative to the applied field. However at much higher frequencies, a number of effects inherent to the liquid can introduce out-of-phase polarization.

Fig. 3.12(c) shows a setup where the electrodes are insulated from the liquid by a thin dielectric layer, along with the corresponding RC model. If the insulating layer is thin with respect to the liquid volume, its capacitance is higher than the one of the liquid, justifying to neglect the capacitance due to the static ϵ' of the liquid ($C_{liq}\rangle\rangle C_\epsilon$). With this approach, the equivalent electric circuit using plane capacitors and resistances leads to

$$V_{liq} = V_{appl}\frac{1}{1+\frac{1}{i\omega R_{liq}C_{ins}/2}}\ , \tag{3.8}$$

where factor 2 in denominator comes from two capacitors C_{ins} in series (see Fig. 3.13) and

$$C_{ins} = \frac{A\epsilon_0\epsilon_{ins}}{d_{ins}} \tag{3.9}$$

The voltage drop in the liquid volume is subject to a decay time constant, comparable to the field in the liquid volume described in Fig. 3.12(a). However, the decay time constant τ_c of this configuration is determined by the liquid resistance and the capacitance of the *insulator*:

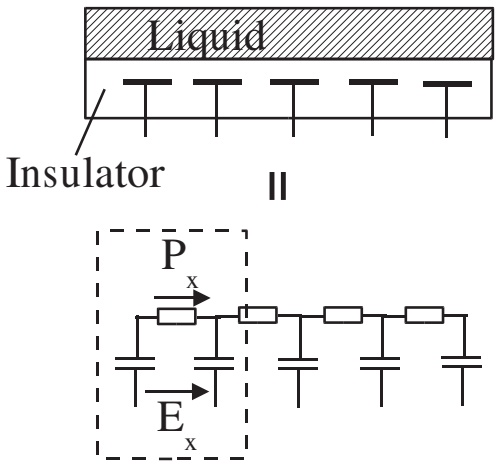

Figure 3.13: Decomposition of the electrode array into an RC model: the isolated array covered by the ionic liquid is represented by an equivalent RC network. A single cell is surrounded by a box.

$$\tau_c = \frac{R_{liq} C_{ins}}{2} \tag{3.10}$$

Compared to setup (a), this shows that for setup (c) with electrodes covered by a thin insulator, the time constant is higher by a factor C_{ins}/C_{liq}. This means that in a configuration where an ionic liquid is polarized between conductive plates covered by a thin insulating layer, an out-of-phase polarization can be used at much lower frequency for a given liquid conductivity, or can be obtained at a given frequency for higher conductivities.

3.2.2 Decomposition of the electrode into an RC network

To generate a traveling wave, an array of interdigitated electrode combs is supplied with a four phase voltage. For simplicity, only the longitudinal component of electric field and media polarization in the direction of propagation are taken into account here. The equivalence between the microelectrode array and an RC network is shown in Fig. 3.13. The polarization of the ionic solution is represented by the voltage drop across the resistor and the electric longitudinal field in one cell is proportional to the voltage applied between two neighboring electrodes.

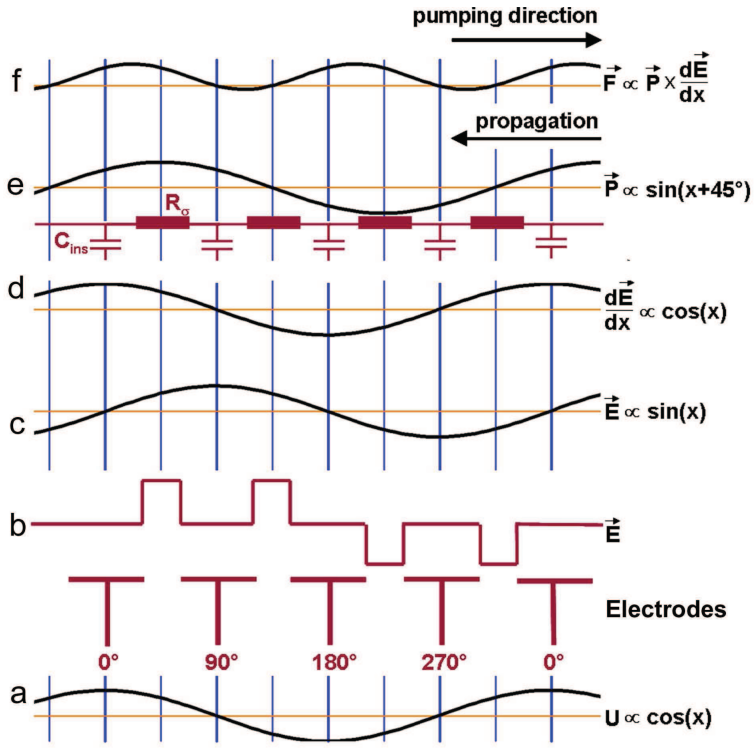

Figure 3.14: Phase relations between the applied voltage (a), the electric field (b and c), the field gradient (d), the liquid polarization(e) and the resulting force (f) acting on the liquid at $t = 0$. The resulting polarization of the liquid is leading the E_x field (by the 45°) at the frequency where the pumping force is maximized. The pumping force is proportional to the mean value of the product of the polarization and the field gradient. Electric field at the electrodes level is discrete (b), which at higher distance above the electrodes will approach sinusoidal shape.

By taking into account only longitudinal components, the force onto the volume of a single cell is:

$$F_x \propto P_x \frac{d}{dx} E_x \tag{3.11}$$

The voltage, electric fields, field gradient, medium polarization, and dielectrophoretic force of the four-phase signal powered microarray is indicated in Fig. 3.14. Curve (a) shows the applied voltage. The longitudinal electric field far above the electrode array E_{appl} can be approached as a sinusoidal wave (Fig. 3.14c)

$$E_x \propto \frac{V_0}{L} \cdot Re\left[\exp i\left(k_x + \omega t - \frac{\pi}{4}\right)\right] \ , \tag{3.12}$$

where V_0 is the peak voltage, L is the pitch and the $\pi/4$ phase shift is due to the fact that the field maximum of the sinewave approach is just above the 90 degree electrode at $t = 0$. In the plane of the electrodes, the field has square x dependence rather than sinusoidal (Fig. 3.14b), but at a height on the order of the pitch above the electrodes, the higher spatial frequencies are evanescent and a sinewave is approached [51] (Fig. 3.14c). Curve (d) shows the field gradient.
The gradient is given by

$$\frac{d}{dx}E_x \propto \frac{V_0}{L} \cdot Re\left[ik \exp i\left(k_x x + \omega t - \frac{\pi}{2}\right)\right] \tag{3.13}$$

and the polarization (Fig. 3.14e) of the volume element above the array along the propagation direction is

$$P_x \propto \frac{V_0}{L_R} \cdot Re\left[\frac{R_{liq}}{R_{liq} + \frac{1}{i\omega C_{ins}}} \exp i\left(k_x x + \omega t - \frac{\pi}{4}\right)\right] \ , \tag{3.14}$$

where L_R is an effective cell length to take into account non-planar geometry. In order to obtain a net force, meaning a non vanishing mean value of Eq. (3.11), if integrated over a time period $T = \frac{2\pi}{\omega}$, the imaginary part of the RC voltage divider

$$\mathrm{Im}\left(\frac{R_{liq}}{R_{liq} + \frac{1}{i\omega C_{ins}}}\right) \tag{3.15}$$

must be maximized, meaning

$$R_{liq} = \frac{1}{\omega C_{ins}} \ , \tag{3.16}$$

which is the case at the crossover frequency of the overall cell impedance $Z = R_{liq} + \frac{1}{i\omega C_{ins}}$. Including Eq. (3.6) and Eq. (3.9) the condition given by Eq. (3.16) then becomes

$$\sigma = \omega \epsilon_0 \epsilon_{ins} \frac{L_R}{d} \ . \tag{3.17}$$

As can be expected from the phase shift between the medium polarization and applied field, the pumping direction will be opposite to the traveling direction of the field.

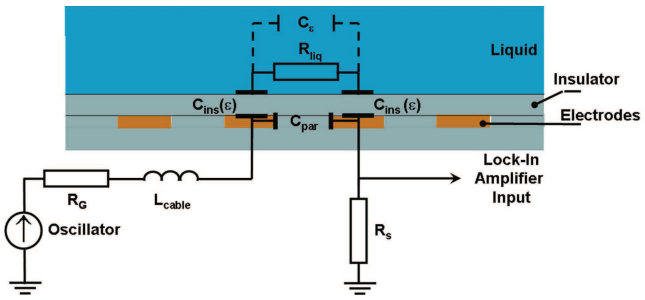

Figure 3.15: The cell with liquid inside can be represented as a RC circuit. The liquid is represented by R_{liq} and the insulator by C_{ins}. Between the electrodes appears the parasitic capacitance C_{par}. R_s is a shunt resistance, which is a part of a voltage divider used in our equations. R_G is the impedance of the generator. L_{cable} is the inductance of the wiring.

3.2.3 Experimental measurement of the crossover frequency

To experimentally measure the cell impedance and to find its crossover frequency, the setup needs to be modeled by taking into account other reactive components in proximity of the cell and in the cabling, as indicated in Fig. 3.15. [For detailed model evolution process see Appendix A] Between the electrodes appears a parasitic capacitance, which has to be taken into account by the model in order to resolve for the RC of interest, i.e. R_{liq}, C_{ins} and C_{par}. R_s is a shunt resistance, which is a part of a voltage divider used in our equations, R_G is the internal impedance of the generator - 50Ω. L_{cable} is the inductance of the wiring. The shunt voltage U_S as function of the applied oscillator voltage U_{OSC} is given by the voltage divider equation

$$U_s = \frac{R_S}{R_S + i\omega L + \underbrace{\left(R_{liq} + \frac{1}{i\omega C_{ins}}\right) || \frac{1}{i\omega C_{par}}}_{Z_{cell}}} U_{osc} \ . \tag{3.18}$$

To obtain L we have removed the cell from the setup and short-circuited the connecting wires ($Z_{cell} = 0$) - see Fig. 3.16. We resolve Eq. (3.18) for ωL

$$\omega L = -\frac{\text{Im}[U_S] U_{OSC} R_S}{|U_S|^2} \ . \tag{3.19}$$

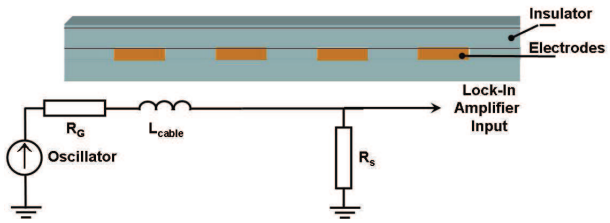

Figure 3.16: Short-circuited setup to obtain a inductance of the wiring L.

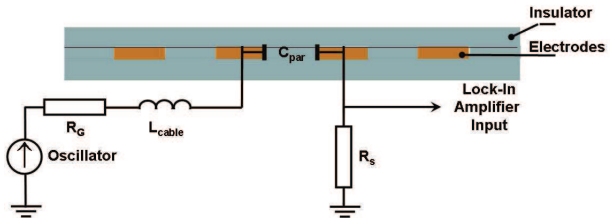

Figure 3.17: Setup without liquid to obtain a parasitic capacitance C_{par}.

$L = 2\ \mu$H is obtained from the slope after plotting Eq. (3.19) over ω.

Knowing the values of L Eq. (3.18) can be resolved for the real and imaginary part of the cell impedance

$$Re[Z] = \frac{Re[U_S]U_{OSC}R_S}{|U_S|^2} - R_G - R_S \ , \tag{3.20}$$

$$\mathrm{Im}[Z] = -\frac{Im[U_S]U_{OSC}R_S}{|U_S|^2} - \omega L \ . \tag{3.21}$$

Next, the cell without liquid ($R_{liq} = \infty$) is connected and the measurement is repeated - see Fig. 3.17. This time Eq. (3.18) is resolved for ωC_{par}

$$\omega C_{par} = \left(\frac{\mathrm{Im}[U_S]U_{OSC}R_S}{|U_S|^2} + \omega L\right)^{-1} \ . \tag{3.22}$$

$C_{par} = 31$ pF is obtained from the slope after plotting the expression (3.22) over ω.

To compensate for the effect of C_{par} in order to obtain the characteristics of R_{liq} and C_{ins}, it is necessary to switch from the cell impedance to admittance

$$Y_{C_{par}} = i\omega C \ , \tag{3.23}$$

$$\begin{cases} |Z| = [(\mathrm{Re}[Z])^2 + (\mathrm{Im}[Z])^2]^{\frac{1}{2}} \\ \Theta_Z = \arctan \frac{\mathrm{Im}[Z]}{\mathrm{Re}[Z]} \end{cases}, \tag{3.24}$$

$$\begin{cases} \mathrm{Re}[Y] = \frac{\cos(-\Theta_Z)}{|Z|} \\ \mathrm{Im}[Y] = \frac{\sin(-\Theta_Z)}{|Z|} \end{cases}. \tag{3.25}$$

Now the admittance of R_{liq} in series with C_{ins} is obtained

$$\begin{cases} \mathrm{Re}[Y_{Corr}] = \mathrm{Re}[Y] \\ \mathrm{Im}[Y_{Corr}] = \mathrm{Im}[Y] - \mathrm{Im}[Y_{Cpar}] \end{cases}. \tag{3.26}$$

Plotting $\mathrm{Im}[Y_{Corr}]$ vs. $\mathrm{Re}[Y_{Corr}]$ will result in a Nyquist plot corresponding to the RC circuit consisting of R_{liq} and C_{ins} [see reffig:fig4].

3.2.4 Experimental techniques

Chip preparation

In the experimental implementation the electrode array shown in Fig. 3.18 was used. A 200 nm high dielectrophoresis electrode array (Fig. 3.18A) was buried in $Si0_2$ (500 nm) deposited on a $\langle 100 \rangle$ n-type silicon wafer. The array was covered with 150 nm of Si_3N_4 and interconnection holes (Fig. 3.18B) were etched with CHF_3/CF_4. Next, the bus lines (Fig. 3.18C) of 150 nm height were deposited, simultaneously being connected to the electrodes via interconnections. Another layer of 200 nm of Si_3N_4 (Fig. 3.18D) was deposited and area over contact pads was etched with CHF_3/CF_4 to uncover the electrodes pads necessary to connect the four phase supply voltage. Finally the 60 μm high microchannels were made using SU8 resist (Fig. 3.18E). The width of the channel (L) varied from 8 to 30 μm and electrode sizes (x) (same as their spacing) from 2 to 10 μm. The four phase interdigitated electrode design of Fig. 3.18B was repeated 25 times, leading to a 1.2 mm long channel with traveling field.

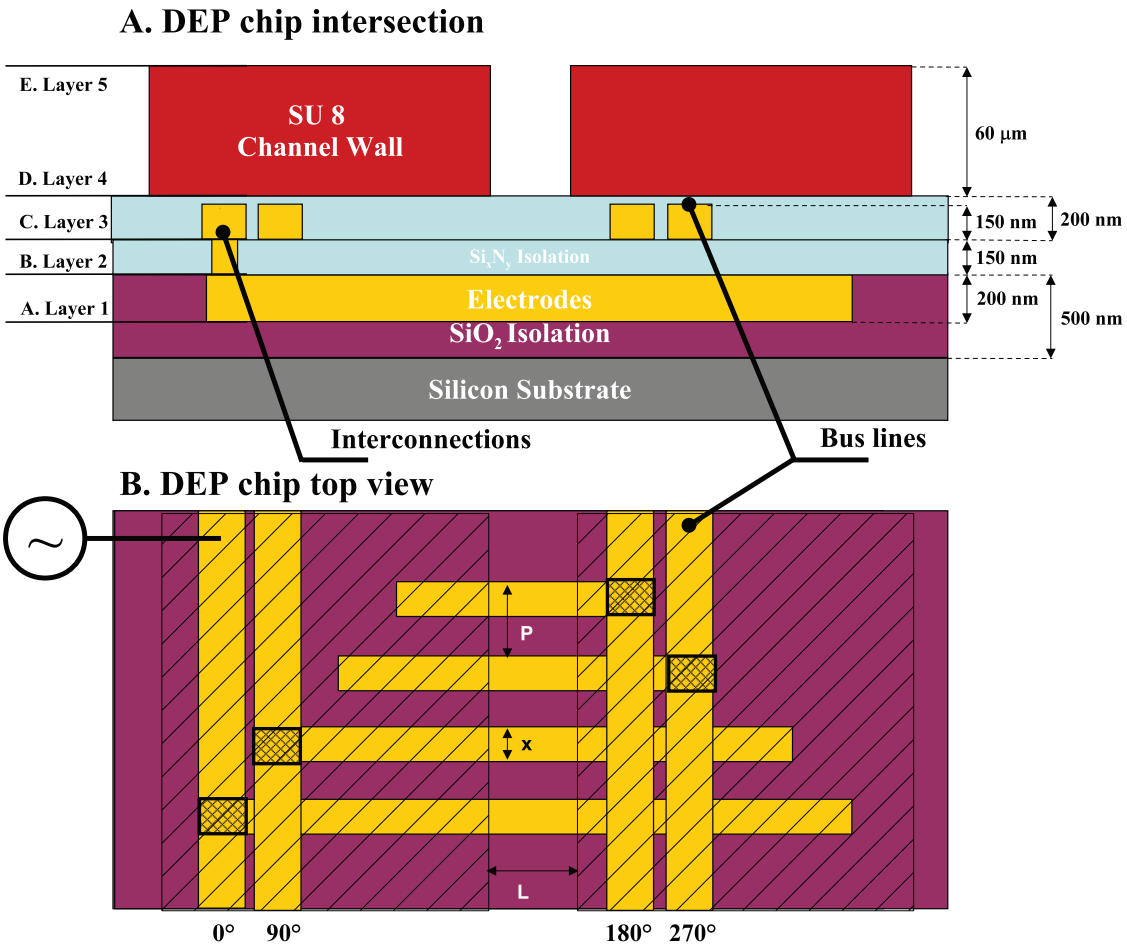

Figure 3.18: Dielectrophoresis chip intersection (1) and top view (2). Five photolithography levels required to fabricate the chip are presented.

Liquid preparation

To 2 ml of DI water 0.5 μl of NaCl 0,9 % solution (Gilbert, France) was added. Resulting liquid conductivity was estimated using Kohlrausch law at $\sigma = 0.001 \frac{\mathrm{S}}{\mathrm{m}}$. After the impedance spectroscopy measurements [see section (3.2.3)], 0.1 ml suspension of latex beads of 10 μm in diameter (Fluoresbrite^{TM}) was added to visualize the motion of the liquid.

3.2.5 Spectroscopy of the cell impedance

A dielectrophoresis chip (Fig. 3.20ab) has been connected to a electrical switch (Fig. 3.19 DEP/ impedance spectroscopy (IS) switch and 3.20c). This switch is

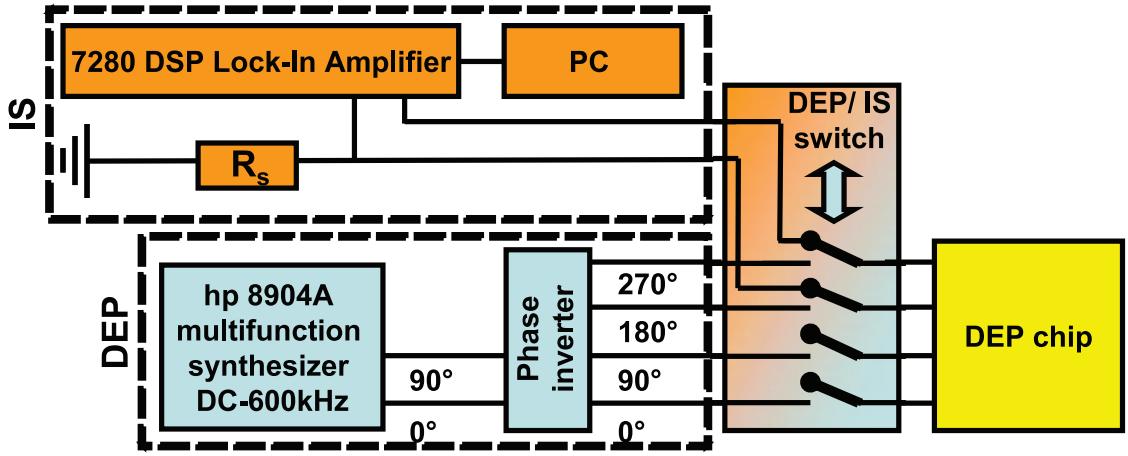

Figure 3.19: Block diagram of a traveling dielectrophoresis setup (TWDEP) allowing to commute the electrode array between impedance spectroscopy measurement (IS) or four phase power supply (DEP).

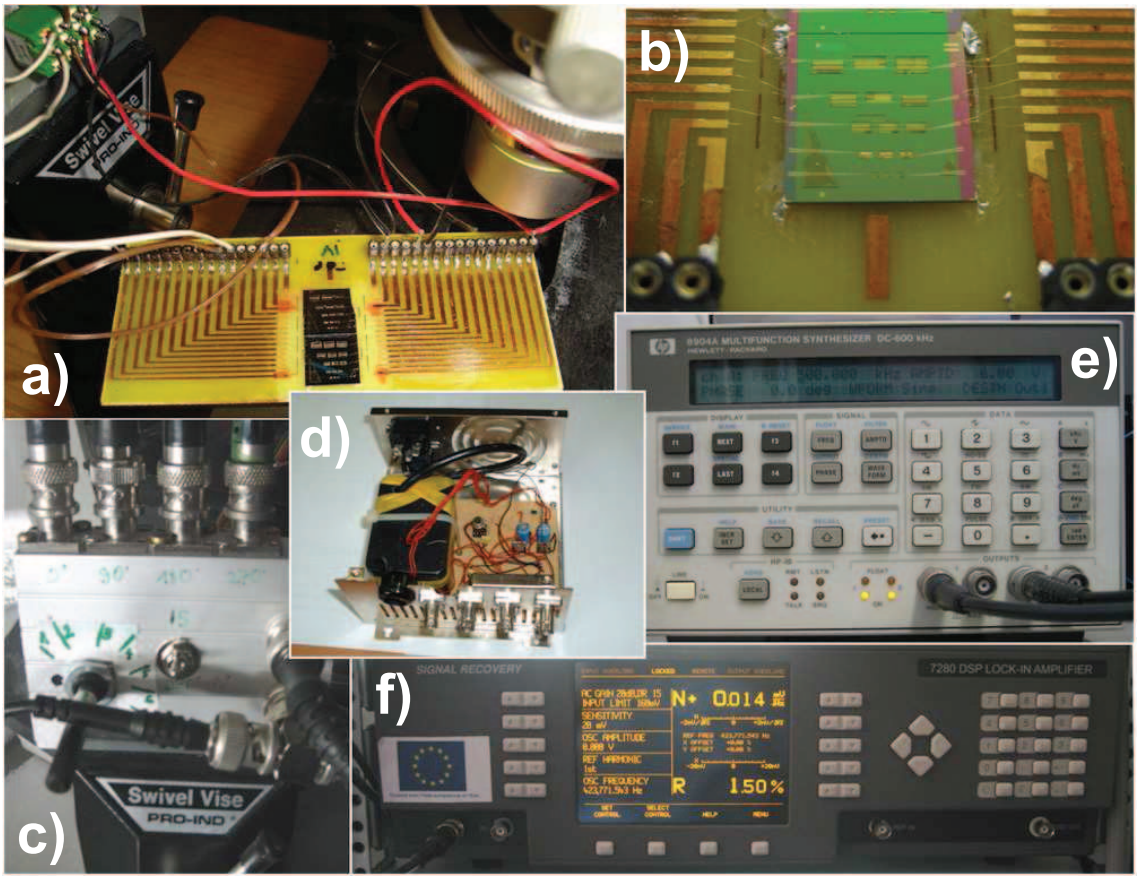

Figure 3.20: (a) DEP chip holder connected to the powers setup; (b) DEP chip connected with golden wires to the holder; (c) DEP/ Impedance spectroscopy switch; (d) Phase inverter; (e) Power supply HP8904a (f) 7280 DSP Lock-in amplifier.

responsible for changing between traveling dielectrophoresis (Fig. 3.19 bottom) and impedance spectroscopy mode (Fig. 3.19 top). For the first mode the signal is generated by a HP8904a multifunction generator (Fig. 3.20e). Since it is only able to generate two signals, a 180° inverter had to be designed (Fig. 3.20d). Two AC signals with phase 0° and 90° are generated by the multifunction generator and connected to the input of the inverter, providing four signals with the same amplitude but different phases 0°, 90°, 180°, 270°. These signals are applied to the electrodes in the DEP chip to generate a traveling field. For the impedance measurement, the signal is generated by a 7280 DSP Lock-In amplifier (Fig. 3.20f). It is connected only to two neighboring electrode combs. Furthermore, we added the possibility to switch between all possible combinations of the electrode comb pairs in impedance spectroscopy mode (not shown for simplicity). This has been necessary to detect symmetry problems and short-circuits between the electrodes. A spectrum is acquired in the $0 - 2$ MHz range (for $V_{OSC} = 0.02$ V), reading the voltage drop on the shunt resistance R_s. By performing the current spectroscopy between two electrode combs rather than on the unit cell as indicated in Fig. 3.15, the reasoning of section 3.2.3 remains valid. By applying the necessary corrections, the impedance cross-over frequency, at witch the liquid pumping is predicted to be optimized (see section 3.2.3), is obtained. The determined frequency, is then entered into the function generator and the mode is set to traveling field dielectrophoresis, using a sinusoidal drive voltage $V_{pp} = 8$ V. With these working parameters, the DEP chip is placed under the optical microscope. A magnification of 200x allows us to observe the motion of the suspension of the latex beads described in section 3.2.4.

Nyquist plot of C_{ins} and R_{liq} serial circuit

Plotting the Im$[Y_{Corr}]$ vs. Re$[Y_{Corr}]$ will give an Nyquist plot (Fig. 3.21). The intersection of the Nyquist plot with the unity slope line yields a cross-over frequency of $f = 545$ kHz.

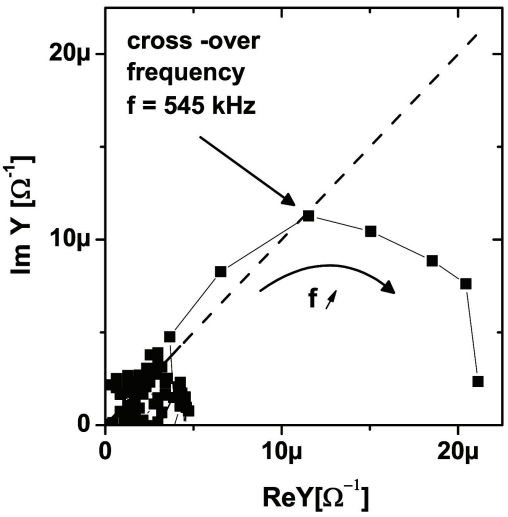

Figure 3.21: Nyquist plot. The cross-over frequency is found to be at $f = 545$ kHz.

3.2.6 Movie sequence - pumping

Fig. 3.22 shows screens-shots of the movie presenting the liquid being pumped with an applied frequency $f = 545$ kHz. It visualizes a bead that is dragged with the liquid. To proof the reproducibility, the direction of the traveling field was inversed. The direction of the liquid flow (Fig. 3.22 A>B>C) was inversed as expected (Fig. 3.22 D>E>F). The speed of the pumped liquid was frequency dependent as shown in Fig. 3.23C. The peak speed $v = 140$ μm/s was found at $f = 500$ kHz, which is very close to the frequency previously predicted by impedance spectroscopy. [†].

3.3 Nanowire manipulation

As mentioned at the beginning nanoassembly has become more and more important in the recent years. This includes both motion and rotation of nano objects. Motion of both particles and liquid is of significant interest as micro liquid and particle handling techniques are necessary for Lab-On-Chip devices [38, 39, 40]. One of the

[†]published: Marczak et *al.* "Traveling wave dielectrophoresis micropump based on structural dispersion, using impedance spectroscopy as feedback", *Journal of Applied Physics* vol. 105, 12, p. 124511 [75]

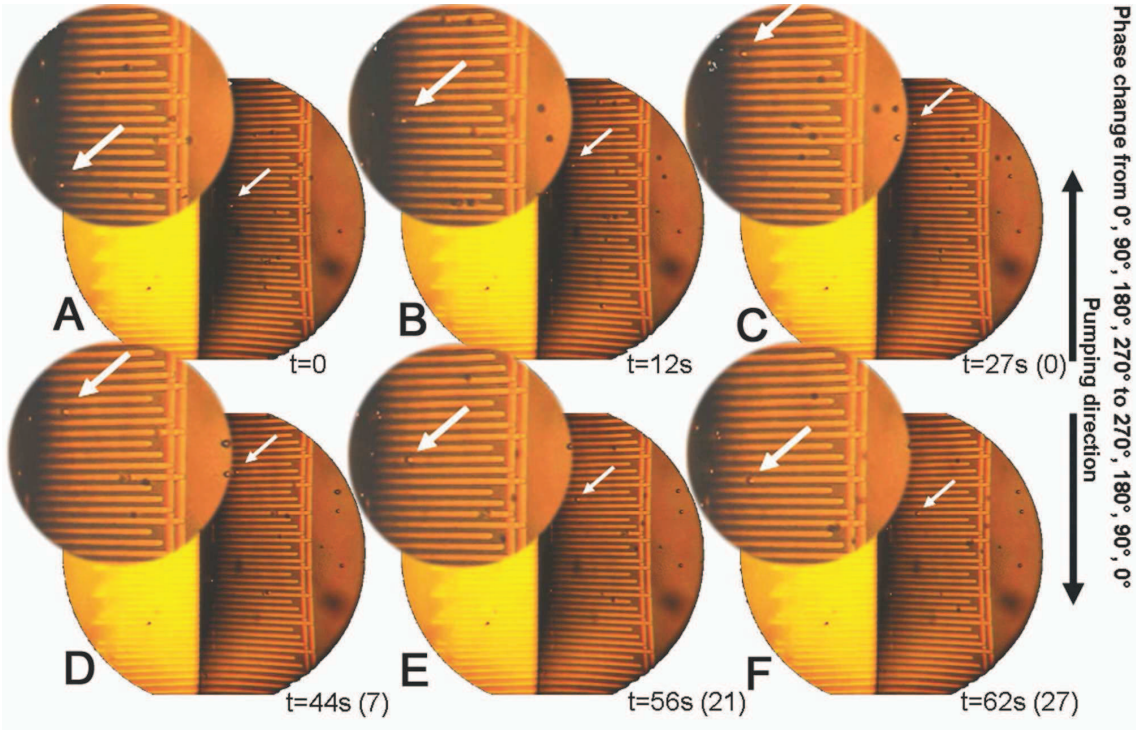

Figure 3.22: Sequences from the liquid pumping movies. Drive voltage 8 V, electrode width 6 μm and electrode spacing 6 μm.

approaches has started with the dielectrophoresis (DEP) discovery described by Pohl in 1978 [67]. This phenomenon was at the beginning used to drag and separate cells, bacteria and particles. It is based on the complex permittivity difference between an object and a medium. By applying a multiphase signal to an electrode array, rotating and propagating fields can be generated causing rotation and motion along the wave propagation vector rather than along a static gradient. The idea was then exploited by Hagedorn [47, 48] who linearized the eletrorotation effect and used it in an electrohydrodynamic pump to move the liquid in the channel.

Electrotation in early experiments was used to determine the object Clausius-Mossotti factor from its rotation speed [53] or to study bacteria behavior [76]. During last years this technique was also applied to metallic nanowires which can serve as polarization filters, microfluidic valves or stirring devices [77]. Recent works have shown that electrorotation is a very useful end efficient tool to rotate metallic nanowires. Frequencies up to f_{rot} = 1800 rpm have been reached in the work of

Fan *et al.* [78] for single nanowires and the synchronous rotation of hundreds of nanowires has been demonstrated by the Mayer group [77].

The aim of this part is a nanowire assembly in the liquid, by inducing the motion on the liquid which would drag aligned nanowires. A dielectrophoresis liquid pumping method based on RC dispersion between the insulating layer covering an electrode array and the bulk resistivity of the liquid was demonstrated previously above. In contrast to other liquid handling methods, it is based on bulk properties and is not based on applying shear forces on a double layer [51] or on a resistivity gradient [50].

Here, our pumping is applied to a suspension of nanowires, and the viscous drag force on the nanowires in the moving liquid is set into competition with trapping forces in the static geometric field gradient above the electrode array. When the propagating field is on, nanowires get aligned perpendicular to the interdigitated electrodes and are dragged with the moving liquid. Some of the nanowires experienced additionally internal electric field and a competition between these forces and pumping forces resulted in nanowires rotation. Following this a new behavior in AC field is presented, which is an out-of-plane rotation with respect to the electrodes, not observed with conventional geometries, as in works of Fan [78] and Mayer [77]. It is also shown that either propagation or rotation can be controlled by tuning the traveling field frequency.

For this DEP experiment large diameter nanowires (described in section 1.4) within the range of $150 - 300$ nm and length of $5 - 10$ μm have been selected. This enables their real time observation by optical microscopy and their responses to changing DEP parameters.

The liquid prepared as in the section 3.2.4 was tested as described above to obtain appropriate pumping frequency as visible in the Fig. 3.23A. To eliminate possible influences of other effects the pumping direction was reversed (Fig. 3.23B). In both cases, liquid speed versus frequency was registered as shown in the graph in Fig. 3.23C. This liquid is further used to prepare the SiNW suspension. A piece of wafer containing nanowires was put into the solution and to suppress water

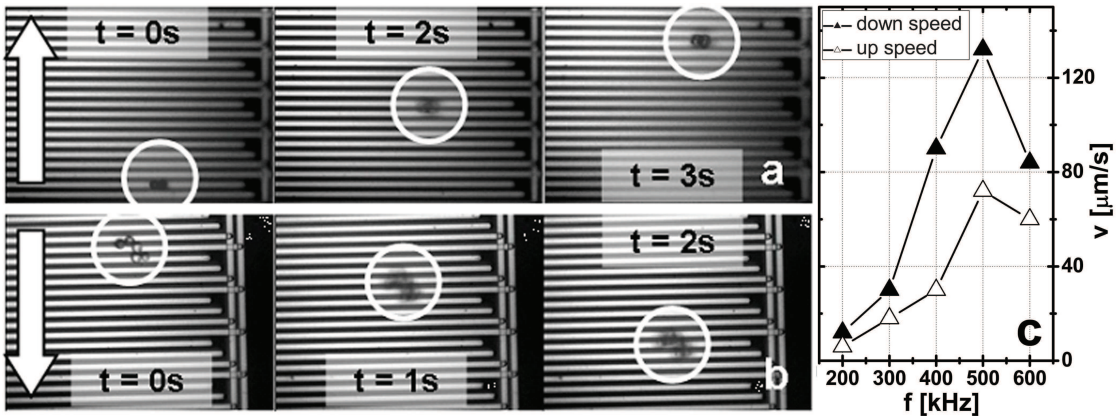

Figure 3.23: Liquid pumping. Bead (10 μm in diameter) transport with the liquid is visible in two directions - up (A) and after phase inversion - down (B). The pumping speed (C - right graph) is frequency dependent and its maximum is $v = 140\ \mu\mathrm{m}/s$ at f = 500 kHz.

repulsion from the hydrophobic nanowires, 4 μl ethanol was added. The suspension was ultrasonicated for one minute to detach nanowires from the substrate. Next, ready suspension was used in the DEP device.

While using the pumping frequency f = 545 kHz, nanowires appeared to align between electrodes and to stick to the surface. When the frequency was reduced to f = 200 kHz a liquid drag of the nanowires was observed. After the frequency was even more reduced to f = 75 kHz beside the nanowire transport, nanowire electrorotation has occurred. In the Fig. 3.24 a movie sequence is shown. In the circles nanowires transport in one direction (Fig. 3.24 $A > B > C$) is shown and when the flow direction is inversed a reproducible behavior is observed (Fig. 3.24 $E > F$). In squares two stages of the electrorotation are visible. First the nanowire is parallel to the surface (A) and then perpendicular (B). The maximum observed rotation frequency was f_{rot} = 200 rpm. The observation was performed until the suspension droplet has evaporated. The nanowires sticked to the surface with the alignment trend perpendicular to the electrodes (parallel to the pumping direction, see 3.24D). The electric field was on until total droplet evaporation.

To tentatively explain the nanowires sticking and electro-rotation a simple model is applied. Two simultaneous traveling dielectrophoresis force systems are considered: **1.** the pumping force $\mathrm{F}_{\mathrm{pump}}$ onto the water ($\epsilon' = 81, \sigma = 0,001$ S/m) on

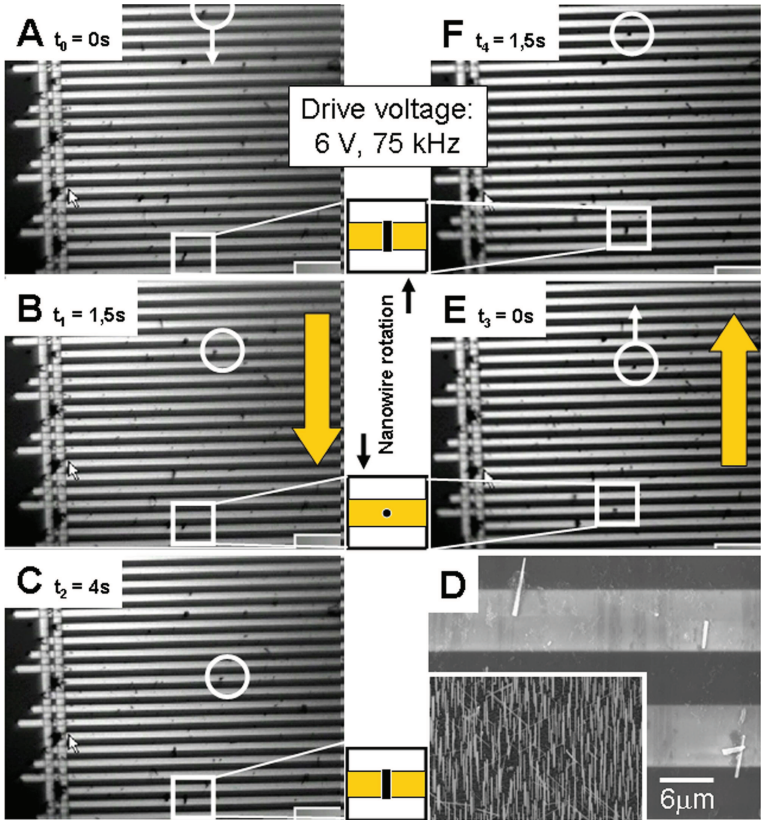

Figure 3.24: Nanowire propagation (circles) and rotation of the nanowires perpendicular to the electrodes (squares). First flow is in one direction ($A > B > C$) and then to sustain the reproducibility phases were inversed and the flow direction has changed ($E > F$). The maximum observable rotation frequency in average was $f_{rot} = 200$ rpm. The SEM image (D) shows that nanowires conserved the alignment after liquid evaporation. The inset presents a SEM image of the nanowires used in the solution.

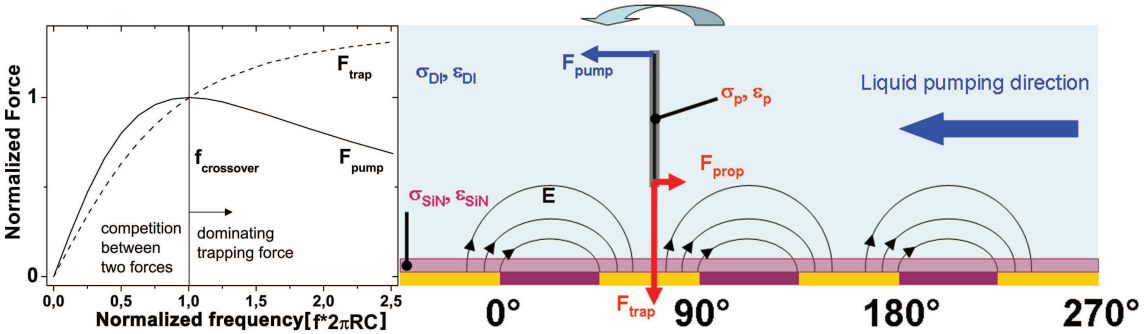

Figure 3.25: This picture models the competition between drag forces F_{drag} and dielectrophoresis induced force F_{trap} and negligible F_{prop}. In the graph the normalized to unity pumping and trapping forces competition is presented.

the silicon nitride insulated electrode environment ($\epsilon' = 7, \sigma = 10^{-15}$ S/m), **2.** the dielectrophoresis forces ($F_{trap} \gg F_{pump}$) on the boron doped silicon nanowires in the water. The former is proportional to the imaginary part of Eq. (3.14), the latter depends on the static gradient seen by the particle in the liquid, depending only on the modulus of the voltage drop within the liquid but not its phase. The qualitative frequency dependence of both forces is shown in Fig. 3.25 (graph). Each curve is normalized to one at $f_{crossover}$, but different coefficients may apply to F_{pump} and F_{trap}. At low frequency, the pumping forces and consequently, due to very small Reynolds number (10^{-15}) [78], the viscous drag force (F_{drag}) on the nanowires are dominating. At high frequency, the direct dielectrophoresis forces onto the nanowire dominate. Furthermore, once the nanowire is between electrodes it can be considered that the direct forces are purely trapping forces since the contribution from the further electrodes can then be neglected and the nanowire does not see a propagating field. Consequently we observe a competition between direct trapping forces on the nanowire (which is dominant at the high frequency), and viscous drag forces proportional to the pumping of liquid (which is dominant at low frequency). If the coefficient of the trapping force is further increased on Fig. 3.25 frequencies lower than $f_{crossover}$ are required to make the drag force dominant and release the nanowire from trapping.

At very low frequencies < 100 kHz it is not expected from Fig. 3.25 that the trapping occurs again since the trapping force stays below the propagating force as zero frequency is approached. The observed behavior, trapping together with electrorotation, might be explained by a strong polarizability of the nanowires at low frequency, *e.g.* by the reaction of the Helmholtz layer of the nanowires to the field, which can be explained in this frequency range. This would increase the coefficient of the trapping forces and make it dominant. Concerning electrorotation it must be explained by permanent dipole moment or net charge remaining on the nanowire. This can cause the nanowire to flip in the alternating field, particularly after one of its ends is lifted by the drag forces. The modelization of the frequency dependent dielectric behavior of the nanowire itself falls, however, beyond the scope

of this work. [‡]

3.4 Conclusions

In this chapter a micropump principle based on the application of dielectrophoretic forces on the liquid has been presented. The necessary out-of-phase polarization of the liquid volume required to apply a force on it as it is exposed to a traveling field is obtained by structural dispersion due to the RC behavior between the insulating electrode coating and the conductive liquid. This makes the mechanism independent of bulk-inherent dispersion and interface effects used by other micropump devices. The analysis of the device by a basic RC model allows to determine the operating conditions and simultaneously shows that optimized pumping force corresponds to the crossover of the complex cell impedance. This coincidence is exploited in the experimental setup by using impedance spectroscopy to monitor and adjust the operating conditions. Since the operating principle is based on structural dispersion, the optimum frequency for a given fluid conductivity can be made considerably lower than the dielectric relaxation frequency of the medium or vice versa; at a given frequency a more conductive liquid can be pumped by appropriately choosing the dimensions of the device. The analytic section describes the method comprehensively. Due to the geometrical simplifications, a precise numerical modelization by a finite element method will however be a remaining task if the method is to be developed further for future applications.

Based on this liquid pumping method a new approach to the nanowire transport was shown. Nanowires translation plus out-of-plane rotation, controlled by the frequency of the DEP was observed and a phenomenological explanation to this phenomenon was proposed as a result of competition between liquid drag and dielctrophoresis induced forces, but further numerical investigations would be of a big interest.

[‡]submitted to *Applied Physics Letters* "Competition between dielectrophoretic forces for the manipulation of nanowires in liquid environment", (2009)

Chapter 4

Nanowire devices

This chapter will focus on nanowire devices. In section (2.4.1) boron doped nanowires were analyzed. These nanowires after successful identification were used to build suspended nanowire devices for nano electro-mechanical systems (NEMS) and Raman Spectroscopy (RS) applications. This chapter will be divided into three sections. First in the introduction (section 4.1) I will provide information about device preparation (which is the same for both types of devices that will be presented). In section (4.2) I will present the silicon nanowire based transistor and its coupling with Raman Spectroscopy and in section (4.3) a device for electrical actuation of SiNWs. In section (4.4) I will show germanium nanowires grown between walls and excited to their resonance frequencies by a piezo element.

4.1 Device preparation

In this chapter two kinds of nanowire devices using suspended nanowires will be demonstrated: (i) for nano electro mechanical systems (NEMS) and (ii) Raman spectroscopy (RS). The clean-room technological steps for the preparation of these devices are identical, and for this reason, I will present them first.

We start with growing 300 nm of thermal silicon oxide on the 3 inch silicon wafer. Next surface is prepared for the first layer of electron beam lithography for electrical

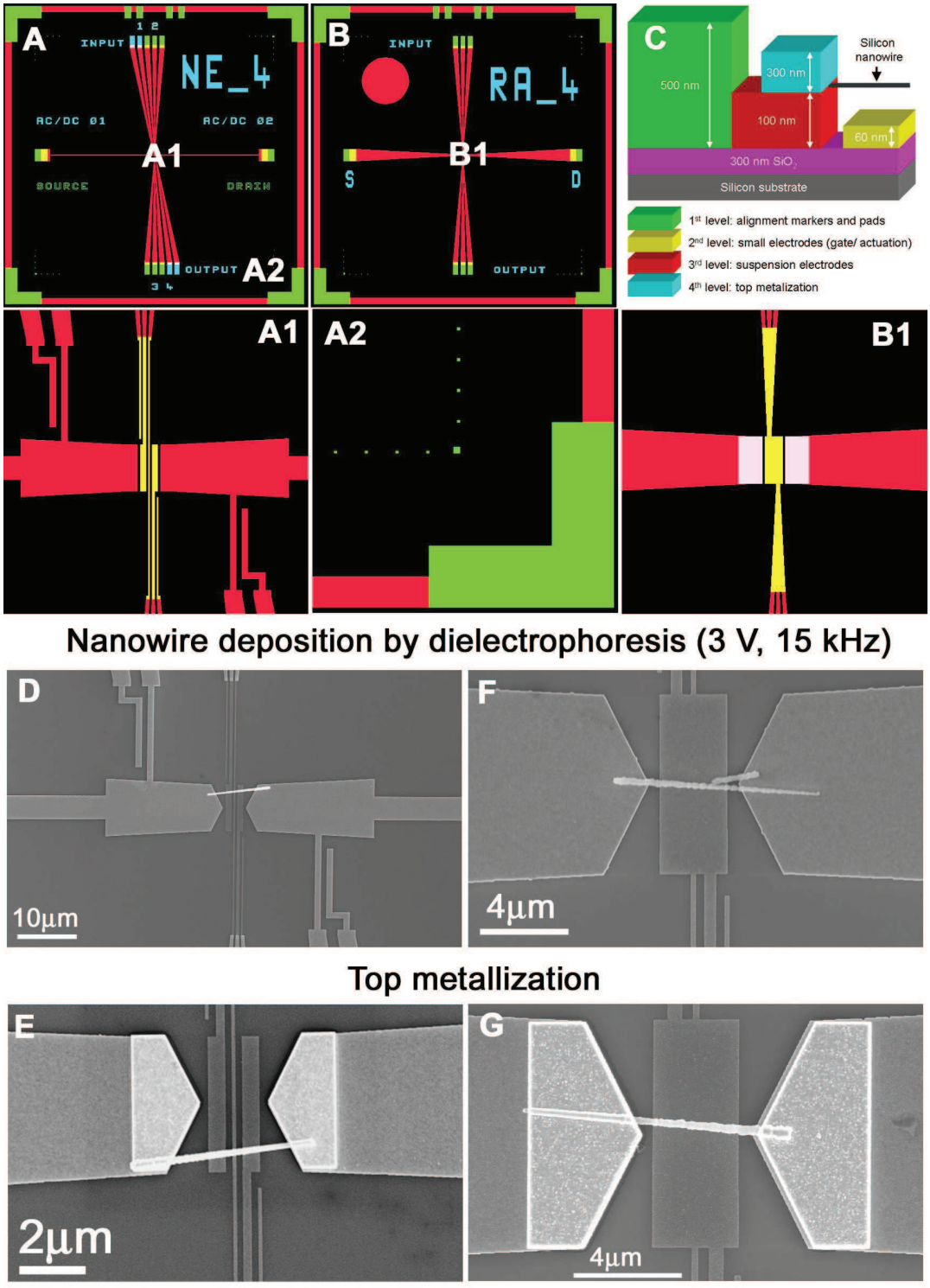

Figure 4.1: Suspended silicon nanowire device preparation steps: (A) for nano electro mechanical systems (NEMS) (A1 - central area zoom) (B) for Raman spectroscopy (RS) application (B1 - central area zoom). Four steps of electron-beam lithography are presented (C). The dielectrophoretic deposition of nanowires is performed after the third step. (D and F). Next nanowires are covered with top layer of metal (E and G). In case of NEMS device small electrodes will actuate and sense the nanowire motion. For the RS device the electrode will serve as a gate.

connection pads and electro-lithography markers (see Fig. 4.1 ABC (green) and A2 for markers). A two layer resist is used (PMGI and PMMA). Next 150/350 nm of Ti/Au are deposited (Ti is used as a sticking layer). After the lift-off process next layer of lithography is prepared (resins EL and PMMA). Here the actuating and/or gate electrodes will be deposited (10/50 nm of Ti/Au). Depending on the application the layout of this layer can be chosen depending on the application type (for NEMS Fig. 4.1 A1, for RS Fig. 4.1 B1, see also Fig 4.1 C yellow). It is also possible to have both types of device produced simultaneously on one wafer. The design is repeated 100 times on the surface. The third step involves big electrode deposition, on which nanowires will be deposited (suspended) (see Fig. 4.1 A, B, and C (red)) (resins EL and PMMA). The metal deposition height is 100 nm to ensure a $\sim$40 nm gap between the nanowire and the electrodes below. The horizontal spacing between big electrodes is 4 μm.

When this stage is completed the wafer exits the cleanroom area and nanowires are deposited. For the deposition of nanowires by dielectrophoresis the suspending electrodes are connected to the AC voltage of $V_{pp} = 3$ V and 15 kHz frequency. Next, nanowires are deposited from a suspension in ethanol (the same preparation procedure applies as in section 2.2.2). One droplet of 2 μl is deposited over the electrode. The whole setup is under an optical microscope to enable a real-time observation of the trapped nanowires. When a nanowire is trapped between two electrodes, the electric field is shut down. We have built in an on/off switch into our electrical circuit, to avoid extended nanowire deposition. For possible deposition errors please see the Appendix B. Nanowires used for deposition are first checked with Raman spectroscopy for doping level as described in section (2.4). In the Figure 4.1 D and F we can see deposited nanowires. After this process wafer returns to the cleanroom for the final metalization step (layer 4, see Fig. 4.1C (blue)). Resins used here are PMGI and PMMA. Next 300 nm gold is deposited. After lift-off the structures presented in Fig. 4.1 E and G are ready for further applications. Normally no negative influence of the resin on the nanowire has been observed. However some errors may occur (see Appendix B).

4.2 Raman spectroscopy coupled devices

This part of work was realized under collaboration with E. Pichonat (LASIR, USTL) and D. Hourlier (EPIPHY Group, IEMN).

In this chapter suspended nanowires were prepared for the Raman measurement application. The aim was to polarize the doped nanowires, vary the gate voltage and to observe the LO-TO (520 cm^{-1}) silicon mode position change (due to phonon-electron interactions) and the change in Fano asymmetry (see section 2.4).

4.2.1 Experiment preparation

In the device, under the nanowire a 60 nm high, 2 μm wide and 4 μm long golden pad has been deposited (see in Fig. 4.1 F and G). It plays double role: (1) to screen the silicon substrate influence during the Raman spectra acquisition *; (2) to act as as a back-gate, so as to tune the carrier density in the nanowires by application of a back-gate bias.

To be able to perform the experiment under LABRAM Raman spectrometer† a special holder was designed. A quarter of wafer was glued to the surface. The device electrodes were connected to the exterior pads by wirebonding. Such device enabled us to polarize the nanowire and to apply the voltage to the gate.

4.2.2 Electrical characterization

The devices after deposition have been tested electrically and by Raman spectroscopy. First a simple I(V) measurement is performed in order to check the usability of a nanowire. If the nanowire exhibits interesting properties (see Fig. 4.5B), the cross I(V) measurements are then performed. It means we check if there is no shortcut between source (S) - gate (G) and drain (D) - gate. In most cases nanowires exhibit ohmic contacts (see Fig. 4.2). Here the resistance is $R = 7\text{k}\Omega$ ‡.

*laser beam used in RS measurements can penetrate the material up to certain depth, as described in section (2.3). Additionally the laser beam diameter is around 1 μm.

†experiment performed at LASIR with Emmanuelle Pichonat

‡Other SiNW parameters: $L = 4$ μm, d = 200 nm, $\rho = 6x10^{-5}\Omega$m, $\sigma = 2 \times 10^4$ Sm^{-1}

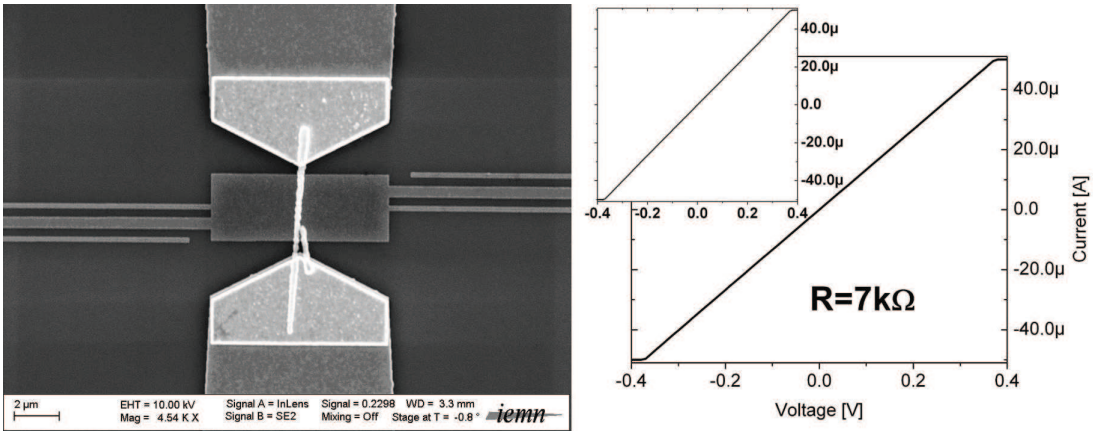

Figure 4.2: Suspended nanowire I(V) characteristics giving $R = 7\text{k}\Omega$ for the SiNW resistance. These parameters: $L = 4\ \mu m$, d = 200 nm, $\rho = 6 \times 10^{-5}\ \Omega$m, $\sigma = 2 \times 10^{4}\ \text{Sm}^{-1}$. The ohmic behavior is recognizable.

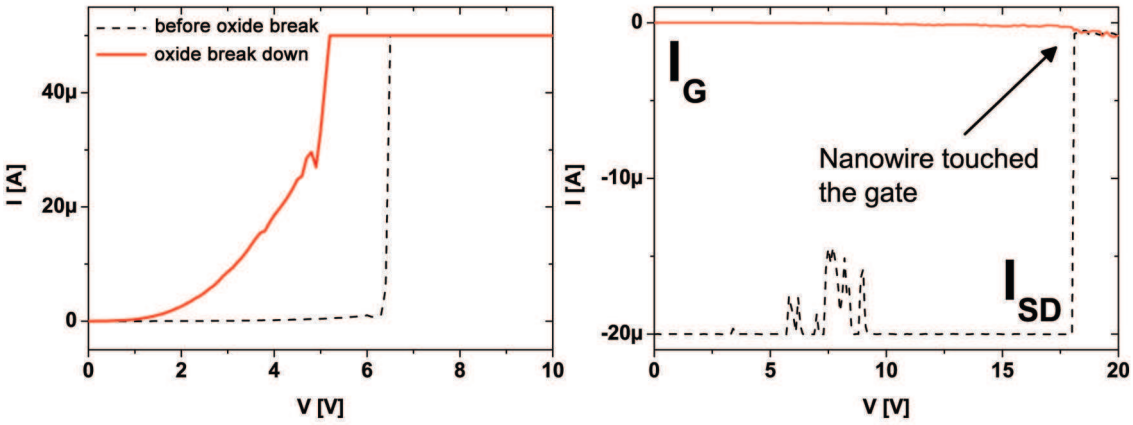

Figure 4.3: (left) Oxide break during I(V) measurement (6 V); (right) Current in function of gate voltage (V_{G}). At $V_{\text{G}} = 15$ V sudden change in I_{SD} current is visible. This implies that the pulling force at this voltage was enough to bend the nanowire more than 40 nm.

In some cases we have Schottky barrier contact like in Fig. 4.4. There the resistance is 42 $k\Omega$ [§]. The resistance is acquired from the linear fit ($y = ax$), where $1/a = R$ in the voltage range close to zero (-0.1 - 0.1 V) (as shown in the inset of Fig. 4.2 and Fig. 4.4). In this measurement an interesting phenomena has occurred. For some nanowires I(V) dependence in the low V_{SD} range was very weak. However after applying voltage > 6 V a sudden change in I(V) graph was observed, like in Fig. 4.3left. We attribute this change to a native oxide break between the silicon

[§]Other SiNW parameters: $L = 4\ \mu$m, d = 200 nm, $\rho = 3x10^{-4}\Omega$m, $\sigma = 2 \times 10^{3}\ \text{Sm}^{-1}$

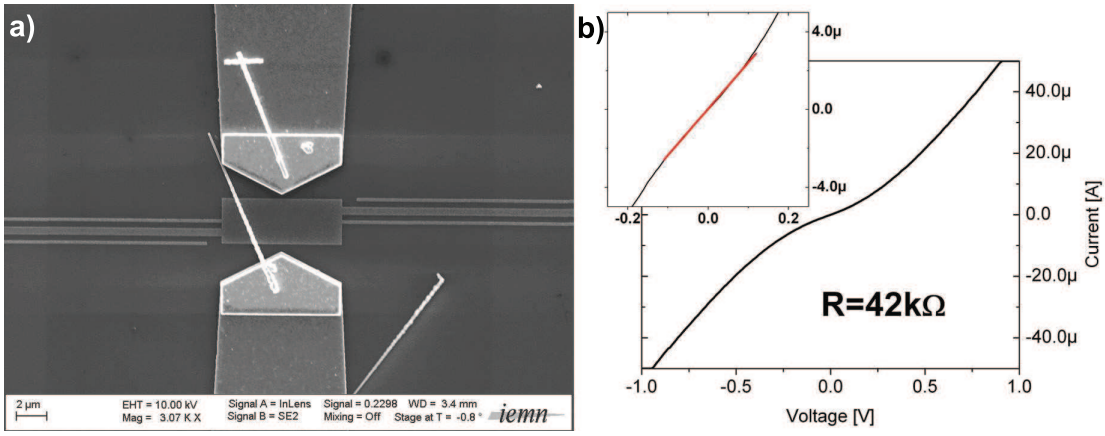

Figure 4.4: Suspended nanowire IV characteristic giving $R = 42\text{k}\Omega$ of the SiNW resistance. These parameters: $L = 4$ μm, d = 200 nm, $\rho = 3 \times 10^{-4}$ Ωm, $\sigma = 2 \times 10^{3}$ Sm^{-1}. Schottky-like behavior (b) is recognizable.

nanowire and metallic contact. A clear change in the hysteresis is visible (Fig. 4.3 dash line before break and the solid red line after)

The next step was to measure the gate influence on the nanowire. The measurement was performed on the polarized nanowire and gate voltage was varied accordingly. We have observed the source drain (I_{SD}) and source gate (I_G) currents. Nanowire was polarized with adequate to its I(V) characteristic (in this case 4 V). In the range up to $V_G \sim 20$ V no gate influence was observed, but at 18 V there is a sudden change in both I_{SD} and I_G currents (see Fig. 4.3right). This implies that the nanowire touched the gate. To prove it source-gate I(V) measurement was performed. This has confirmed our prediction.

These results mean that our device is unfortunately not suitable to perform the field effect transistor experiment. We can approach (supposing the NW is metallic and all the voltage drop occurs between NW and gate) the capacitance C[F/m] between the nanowire and electrode below, what will give us

$$C = \frac{2\pi\epsilon_0\epsilon_{\mathrm{r}}}{\ln\left(\frac{4\ \mathrm{d_{gap}}}{\mathrm{d_{NW}}} + 1\right)}\ , \tag{4.1}$$

where $\mathrm{d_{gap}}$ is the distance between nanowire and electrode, $\mathrm{d_{NW}}$ is nanowire diameter, ϵ_0 is the vacuum permittivity and ϵ_r relative permittivity (in our case air). Now using a relation that CV = Q and Q being proportional to the doping $\rho = \rho_{\mathrm{doping}}e$,

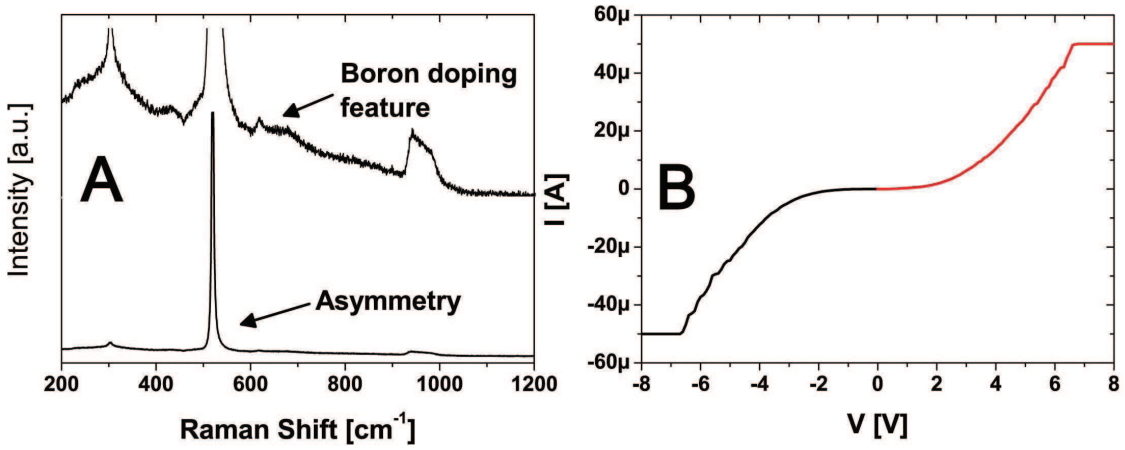

Figure 4.5: (A) Raman spectra of suspended boron doped silicon nanowire; (B) I(V) characteristics of the same nanowire.

where ρ_{doping} is nanowire doping level, e is an elementary charge, we can calculate the voltage - V, needed on the gate to influence the carriers in the nanowire

$$V = \ln\left(\frac{4\ \mathrm{d}_{gap}}{\mathrm{d}_{NW}} + 1\right)\frac{\mathrm{d}_{NW}^2 \rho \alpha}{8\epsilon_0}\ , \tag{4.2}$$

where α is influence coefficient in percents (100% is for suppressing all carriers). For diameter of the nanowire $\mathrm{d}_{NW} = 150$ nm, boron concentration 10^{19} atoms/cm^3 (reflected in Raman spectra in Fig. 4.5A) and $\alpha = 10\%$ we will get 20 V. Our device does not comply with this requirement. One of the possible solutions would be to diminish the doping or to reduce the gap. This on one side disappointing result suggest that nanowires should be suitable for NEMS applications, described in the following section (4.3).

4.3 NEMS

This part of work was realized under collaboration with B. Legrand (Microsystems Group) and D. Hourlier (EPIPHY Gropup) from IEMN.

The interest in MicroElectroMechanical System started in 1960s [79]. Nowadays they are commercially designed for sensing, dosing and moving systems. Just to mention few of MEMS applications: ink jet printers (ink dosing system [80]); accelerometers (used for airbags switch sensors) and in telecommunications (various

resonators to tune in to the appropriate signal frequency) [81]. There is a range of other applications in development like small mirrors to modulate light beams [82]. They are of a big interest for industry as most of them are based on advanced silicon technologies. Recent advanced silicon technologies are allowing significant size and mass reductions. This way NEMS have emerged. But they are still at the research and development stage [79]. The critical size for NEMS is in the range from hundreds to few nanometers. One class of these devices, on which my work is focused, consist of suspended or double-side clamped wires/beams of nanometers diameters. These objects will be actuated at their resonance frequencies, which will vary depending on the material (ρ), beam length (l), beam width (w) and Young modulus (E). This frequency (f_0) of a double clamped beam will be expressed with the following formula

$$f_0 = 1.028 \frac{w}{l^2} \sqrt{\frac{E}{\rho}} \ . \tag{4.3}$$

The following frequencies will be at $\mathrm{f_1} = 2,76\mathrm{f_1}$, $\mathrm{f_3} = 5,39\mathrm{f_1}$, $\mathrm{f_3} = 8,94\mathrm{f_1}$

One of the recent challenges are biosensors, which would act as a nanobalance of pg[¶] resolution or of a sensor for the presence of dangerous substances. An interesting work was performed by Davis *et al.* [83] in which the authors have shown a NEMS devices reacting with specific molecular species. They have calculated that their device with cantilever of dimensions 50 μm $\times$ 500 nm $\times$ 1.8 μm with spring constant 0.08 N/m and resonant frequency of 286 kHz could detect masses down to 9.7×10^{-16} g. They presented a formula to evaluate this (where the attached particle does not influence the spring constant of the beam)

$$\Delta m = \frac{k}{0.72\pi} \left(\frac{1}{f_2^2} - \frac{1}{f_1^2} \right) \ , \tag{4.4}$$

where, f_1 and f_2 are the resonance frequencies before and after adding the mass Δm. This principle can be used for creating a very precise virus, bacteria or particle sensor. During 8 years this technique has evolved tremendously and in 2008 Lassagne *et al.* presented a nanotube device based setup able to detect mass down to 1.4×10^{-21} g [84].

[¶]pico gram

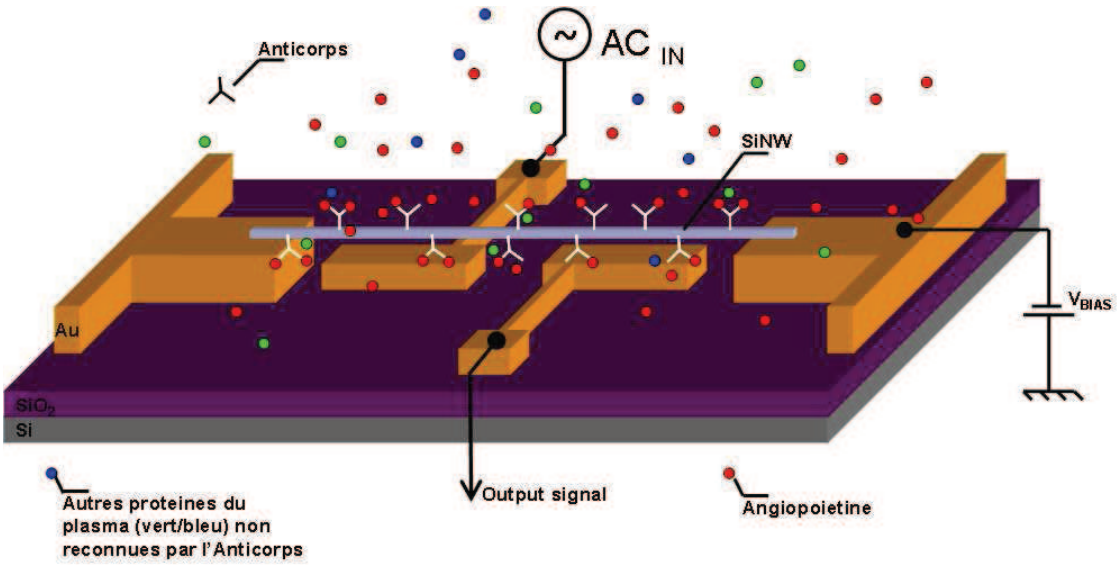

Figure 4.6: Presentation of the operation principle of a NEMS biosensor. Suspended nanowires are first deposited on the suspending (left and right) electrodes, and then functionalized to be able to attract proteins. The working principle is based on the excitation of the suspended nanowire by electrostatic forces using the actuation electrode, and the vibration detection using a capacitive detection (second electrode below the nanowire). The nanowire resonance frequency is expected to change.

4.3.1 Experiment preparation

The aim of our project was to test the use of CVD nanowires as beams for the realization of NEMS devices, with the final aim to produce a biosensor. The 3D representation is shown in Fig. 4.6, where the capacitive detection of the nanowire oscillation amplitude is used. If a protein would attach to the functionalized nanowire, the nanowire mass would change, and thus its mechanical resonance frequency. Its principle bases on the excitation by electrostatic forces between nanowire and one of the electrode in the substrate plane below the nanowire and the vibration detection by the second one using capacitive effects.

4.3.2 Results and discussion

Devices were prepared as described in section (4.1) using NEMS small electrode mask in step two of the e-beam lithography. Resulting ready devices are presentend in Fig. 4.9b and in three dimensional perspective are presented in Fig. 4.7. Before

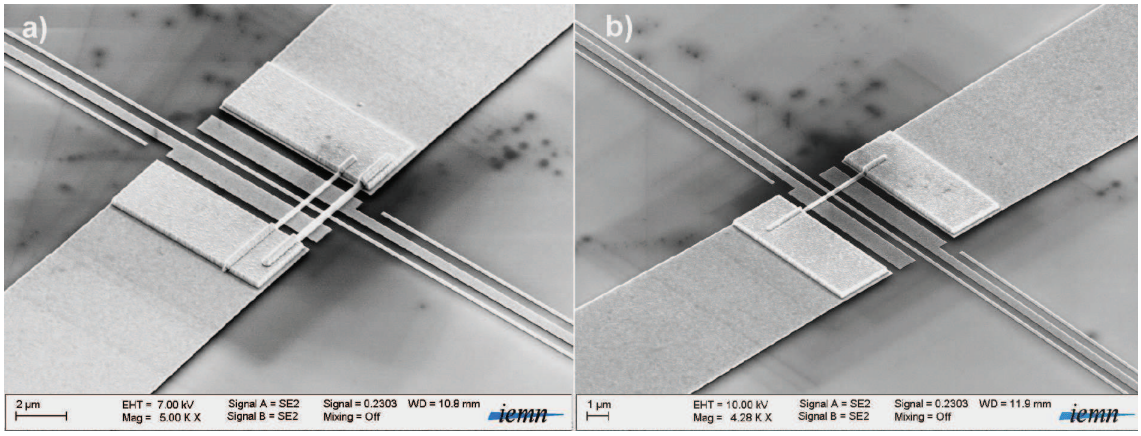

Figure 4.7: SEM 3D images of silicon nanowires deposited for NEMS applications.

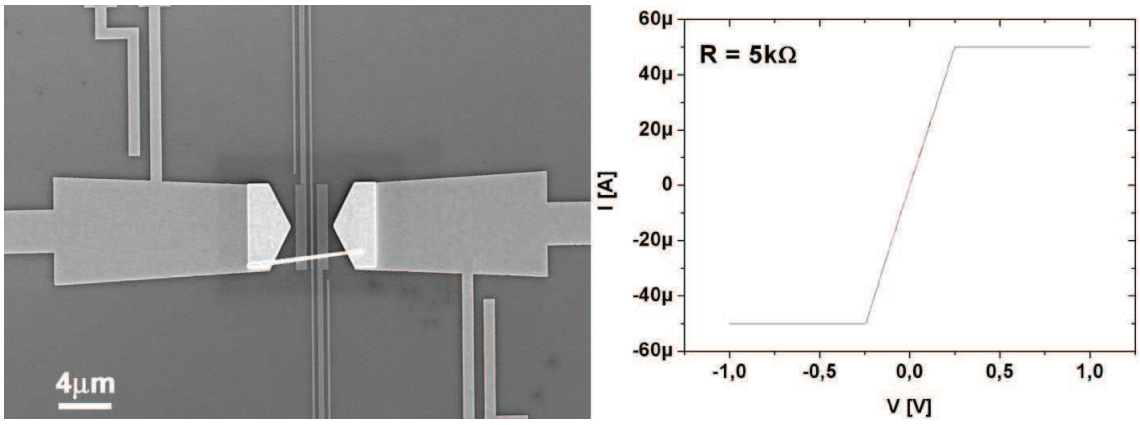

Figure 4.8: (left) Suspended nanowire I(V) characteristics giving $R = 5\text{k}\Omega$ of the SiNW resistance. There parameters: $L = 4$ μm, d = 200 nm, $\rho = 6 \times 10^{-5}$ Ω m, $\sigma = 2 \times 10^4$ S m^{-1}. Ohmic behavior (right) is recognizable. The observed saturation in the I(V) is due to a compliance of the analyzer (is 50 μA) which limits the measurable current for safety issues.

devices were connected to the actuating/ detecting setup they were characterized electrically. The first doped silicon nanowire generation was almost metallic in behavior (see Fig. 4.8). From this I(V) spectrum we can deduce that the nanowire contacts were ohmic and calculate a resistance of 7 kΩ [‖]. For such prepared structures a theoretical resonance frequency is expected at 50 MHz. Devices were connected to the measurement setup. Nanowires were first polarized with DC voltage (3 V). Next to the actuating electrode AC voltage up to 6 V_{pp} was applied to create a pulling field. The second electrode was set to detect the change of capacitance between it

[‖]for the nanowire diameter of 200 nm

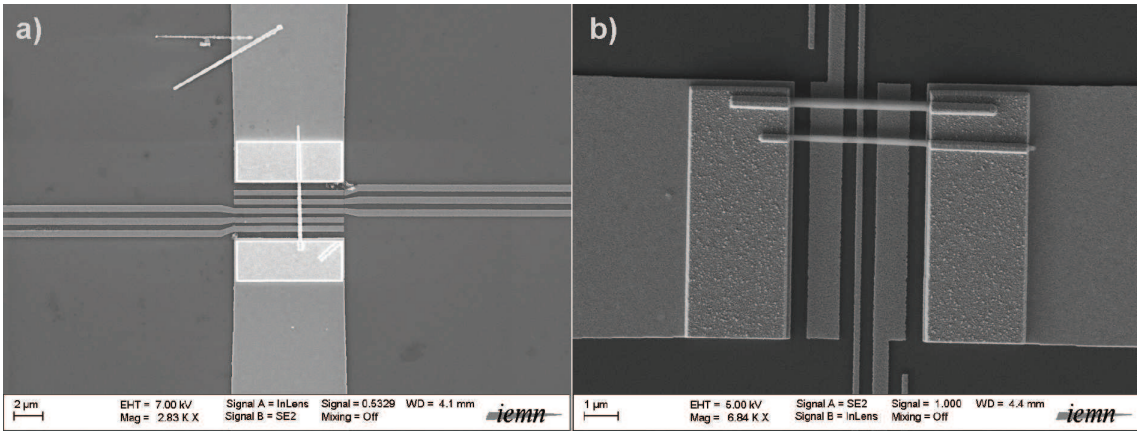

Figure 4.9: Suspended silicon nanowires on rectangular electrodes over different gate electrodes design: (a) Multigate transistor test and (b) Nems application: actuation and reading electrodes are visible. Nanowires are 40 nm the electrodes.

and the nanowire. The resonant frequency has been observed in the preliminary measurements at 57 MHz**.

Before the end of this work I have deposited germanium nanowires which are $2-4$ μm long and $10-20$ nm in diameter. But this structures are still under development as the germanium nanowires are too soft and stick to the surface during deposition, so I cannot use them in this type of devices, unless reducing the lateral spacing between the suspending electrodes. The future step for this experiment would be to diminish the gap between the wire and the gate electrode up to $10-20$ nm or lateral spacing, or to use smaller nanowires. By finding the compromise between those elements one could decrease the resonance frequency and drive voltages, leading to more user friendly device operation.

**measurements performed by B. Legrand from the Microsystems group at IEMN

4.4 Nanowire mechanical excitation

This part of work was realized under collaboration with D. Troadec (Centrale de technologie, IEMN) and D. Hourlier (EPIPHY, IEMN).

4.4.1 Sample preparation

Germanium nanowires (GeNW) were grown on walls etched in silicon. At the beginning on a special SOI wafer 200 nm of silicon nitride is grown. It will serve as a mask during etching. But first the mask has to be etched in the Si_3N_4. Wafer is covered with SAL 601 negative resist and walls design is transmitted using electron beam lithography. This step is vital, as the walls have to be aligned according to the $\langle 111 \rangle$ crystalline plain of the wafer. (this plane is etched by KOH much slower than others). Next the wafer is etched with CHF_3/CF_4 to uncover the silicon. However leaving the nitride screened by the SAL 601 resist. After this process SAL 601 is removed with Acetone and Plasma O_2 etching. Such processed wafer is ready for KOH etching. The silicon top layer of the SOI is etched down to the oxide. The walls have different lateral spacing starting from 6 μm and increasing up to 20 μm. Their height is 20 μm, length 150 μm and width 60 μm. To make the lateral growth possible gold has to be deposited on the one side of the wall. To do this the metalization process is performed with tilted wafer. After cleaning in isopropanol alcohol and acetone the structure is ready for the growth. The growth of the GeNW was performed by D. Hourlier.

Ready sample, with nanowires, after pre-examination in scanning-electron microscope (SEM), was mounted on an atomic force piezo-element and loaded in the vacuum chamber of a SEM. The piezo-element was excited using a sine-wave generator, and SEM images were acquired with and without excitation.

4.4.2 Results and discussion

Due to the nanowire geometrical characteristics (nanowire diameter $20-30$ nm and length 10 μm, density of Ge: 5.323 g$\cdot$cm^{-3}, Young modulus: 106 GPa [85]), the

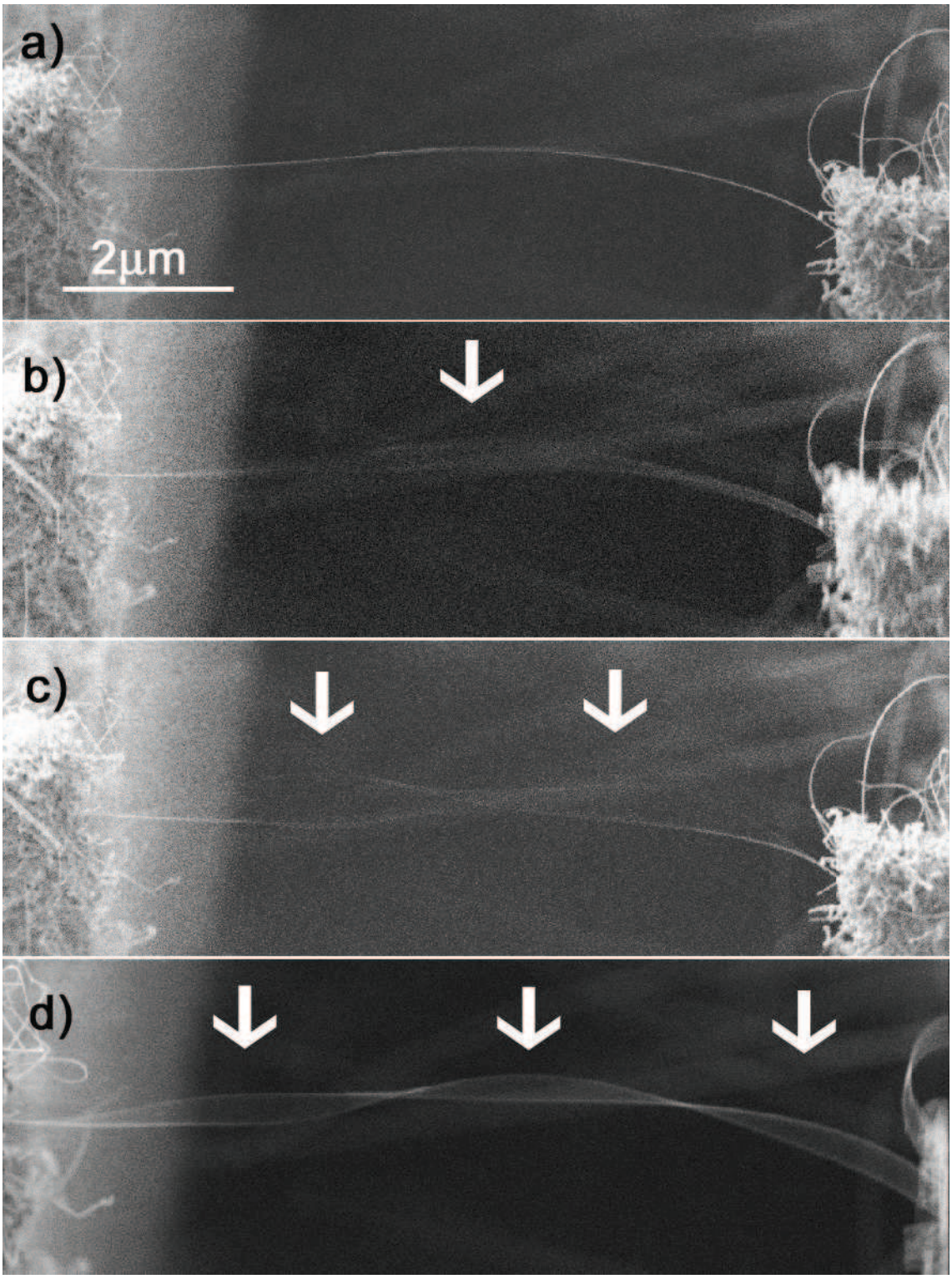

Figure 4.10: Germanium nanowire grown between walls (10 μm long and 20 nm in diameter): (a) without mechanical excitation; (b) Selective mechanical excitation of the nanowire at ∼1.8 MHz (quality factor Q∼1000); (c) second excitation at ∼2.25 MHz mode; (d) third excitation at ∼2.35 MHz.

resonance frequencies can be calculated from the Eq. (4.3) to be in the range of few MHz. The images in Fig. 4.10 show the resonance patterns observed for the nanowire (a) without mechanical excitation, and with mechanical excitation at (b) 1.82 MHz, (c) 2.25 MHz and (d) 2.35 MHz. The observation of respectively one, two and three half waves in (b), (c) and (d) attest that the oscillation pattern corresponds to vibration eigenmodes in a rough agreement with the resonance frequencies estimated from a doubled clamp beam model (see formula (4.3) for the fundamental frequency). However, the fact specific (*i.e.* not cylinder) geometry of the nanowire and the fact that the nanowires are not grown straight along the walls may alter the eigenfrequencies, as observed *e.g.* in the case of the oscillation pattern of nanotubes probed from field-emission experiments [86]. The quality factor of the resonances has been estimated to ∼1000.

4.5 Conclusions

In this chapter three types of structures based on nanowires were prepared and analyzed. First two based on doped silicon nanowires and the third on the germanium nanowires. At the beginning application for Raman spectroscopy was tested - to be able to measure the Raman spectra of polarized nanowire in function of gate voltage. Second approach was to test usability of nanowires for NEMS application. In the first case the final aim was not reached but it made a significant influence on the second one, where electro actuation has been observed. However reasons for the Raman coupled device failure were identified: (i) the gap between nanowire and gate/ actuating electrodes is to big, (ii) nanowires diameter should be diminished. In the third part germanium nanowires were grown between the walls and actuated mechanically. This part ended successfully by observing different nanowires vibration modes. The Q factor of the GeNW was estimated to be $\sim$ 1000.

Chapter 5

Summary

In the first part of this work I have described Raman effect and measured Raman scattering spectra of single, well separated Si nanowires. The analysis of the spectra shows that the nanowires are crystalline, but surrounded by an amorphous envelope. The local temperature of the nanowires has been determined from the Stokes/ anti-Stokes (I_S/I_{AS}) ratio and from the analysis of the LO-TO line 520 cm^{-1} down-shift. A good agreement has been observed between these two methods. From the Raman spectra we have obtained information on nanowire morphology (crystalline silicon core in amorphous sheath) and temperature distribution which have shown that silicon core is cooler than amorphous silicon shell. We explain this effect as caused by poor thermal nanowire conductivity and good silicon core tip contact with metal substrate. Additionally, boron doped silicon nanowires were investigated. Using Fano resonance fit and comparing its parameters with bulk doped silicon, the Boron concentration in the nanowires was determined at 10^{19} cm^{-3}. This chapter has shown how universal, easy and fast Raman spectroscopy tool can be. It can provide maybe not the most accurate information, but sufficient to decide whether grown nanowires are good or not, whether expected parameters were achieved or not. On this basis further more complicated and time consuming measurements can be performed without risk that the material is of low quality.

In the second part a micropump principle based on the application of dielec-

trophoretic forces on the liquid has been presented. The necessary out-of-phase polarization of the liquid volume required to apply a force on it, as it is exposed to a traveling field, is obtained by structural dispersion due to the RC behavior between the insulating electrode coating and the conductive liquid. This makes the mechanism independent of bulk-inherent dispersion and interface effects used by other micropump devices. The analysis of the device by a basic RC model allows to determine the operating conditions and simultaneously shows that optimized pumping force corresponds to the crossover of the complex cell impedance. This coincidence is exploited in the experimental setup by using impedance spectroscopy to monitor and adjust the operating conditions. Since the operating principle is based on structural dispersion, the optimum frequency for a given fluid conductivity can be made considerably lower than the dielectric relaxation frequency of the medium or vice versa, at a given frequency a more conductive liquid can be pumped by appropriately choosing the dimensions of the device. The analytic section describes the method comprehensively. Due to the geometrical simplifications, a precise numerical modelization by a finite element method will however be a remaining task if the method is to develop further for future applications.

Based on this liquid pumping method a new approach to the nanowire transport was shown. Nanowires translation plus out-of-plane rotation, controlled by the frequency of the DEP was observed and a phenomenological explanation to this phenomenon was proposed as a result of competition between liquid drag and dielectrophoresis induced forces, but further numerical investigations would be of a big interest.

In the last part first based on the doping analysis by Raman spectroscopy silicon nanowires were investigated for possible applications for: nanoelectromechanical biosensor and Raman spectroscopy device enabling observing gate influence on the polarized nanowire spectra. Nanowires were deposited using static dielectrophoresis.

The technological background has been prepared for such devices based on bottom-up CVD-grown nanowires, but the success of these subjects will require a deeper insight and further research. However technological background has been

prepared, and applied in the nanowire electrical actuation (observed at 57MHz).

At the end germanium nanowires grown between etched silicon walls are presented. Nanowires were actuated mechanically in the few MHz range.

To summarize, in my thesis I have shown Raman Spectroscopy as an efficient nanowire characterization method, which allows easily to extract information about nanowire structure, doping level and local temperature used further for nanowire devices applications. A dieletrophoresis phenomenon has been shown in application for nanowire manipulation and propagation (traveling dielectrophoresis), which has proved the applicability of silicon and germanium nanowires in nanodevices. Meaning that the aims of the PhD has been successfully accomplished.

Bibliography

[1] D. Hourlier and P. Perrot, "Answer to the challenging question: Is there a size limit of nanowires?," *Journal of Nano Research*, vol. 4, p. 135, 2008. [cited at p. 7, 41]

[2] A. Compton, "A quantum theory of the scattering of x-rays by light elements," *Physical Review*, vol. 21, p. 483, 1923. [cited at p. 12]

[3] R. Singh, "C. v. raman and the discovery of the raman effect," *Physics in Perspective*, vol. 4, p. 399, 2002. [cited at p. 12, 13, 14]

[4] C. Raman, "A change of wave-length in light scattering," *Nature*, vol. 121, p. 619, 1928. [cited at p. 13]

[5] Renishaw *http://www.renishaw.com/en/6259.aspx*. [cited at p. 15]

[6] S. Sasic, D. Clark, J. Mitchell, and M. Snowden, "A comparison of raman chemical images produced by univariate and multivariate data processing a simulation with an example from pharmaceutical practice," *Analyst*, vol. 129, p. 1001, 2004. [cited at p. 15]

[7] S. Osswald, E. Flahaut, H. Ye, and Y. Gogotsi, "Elimination of d-band in raman spectra of double-wall carbon nanotubes by oxidation," *Chemical Physics Letters*, vol. 402, p. 422, 2005. [cited at p. 15]

[8] M. Zdrojek, W. Gebicki, C. Jastrzebski, T. Mlin, and A. Huczko, "Studies of multiwall carbon nanotubes using raman spectroscopy and atomic force microscopy," *Solid State Phenomena*, vol. 99, p. 265, 2004. [cited at p. 15]

[9] J. Chalain, "Identification of ge pol diamonds: a second step," *Journal of Gemmology*, vol. 27, p. 73, 2000. [cited at p. 15]

[10] R. Clark, "Raman microscopy as a structural and analytical tool in the fields of art and archaeology," *Journal of Molecular Structure*, vol. 834, p. 74, 2007. [cited at p. 15]

[11] S. Harris, A. O'Neill, W. Wang, P. Gustafson, J. Boileau, W. Weber, B. Majumdar, and S. Ghosh, "Measurement of the state of stress in silicon with micro-raman spectroscopy," *Journal of Applied Physics*, vol. 96, p. 7195, 2004. [cited at p. 15]

[12] N. Stone, C. Kendall, N. Shepherd, A. Crow, and H. Barr, "Near-infrared raman spectroscopy for the classification of epithelial pre-cancers and cancers," *Journal of Raman Spectroscopy*, vol. 33, p. 564, 2002. [cited at p. 15]

[13] G. Jochem and R. Lehnert, "On the potential of raman microscopy for the forensic analysis of coloured textile fibres," *Science & Justice*, vol. 42, p. 215, 2002. [cited at p. 15]

[14] G. Imamura, T. Kawashima, M. Fujii, C. Nishimura, T. Sai-toh, and S. Hayashi, "Distribution of active impurities in single silicon nanowires," *Nano Letters*, vol. 8, p. 2620, 2008. [cited at p. 18, 19, 30]

[15] Y. Cui, Z. Zhong, D. Wang, W. Wang, and C. Lieber, "High performance silicon nanowire field effect transistors," *Nano Letters*, vol. 3, p. 149, 2003. [cited at p. 18]

[16] Y. Cui, Q. Wei, H. Park, and C. Lieber, "Nanowire nanosensors for highly sensitive and selective detection of biological and chemical species," *Science*, vol. 293, p. 1289, 2001. [cited at p. 18]

[17] X.-J. Huang and Y.-K. Choi, "Chemical sensors based on nanostructured materials," *Sensors and Actuators B: Chemical*, vol. 122, p. 659, 2006. [cited at p. 18]

[18] X. Zhou, J. Hu, C. Li, D. Ma, C. Lee, and S. Lee, "Silicon nanowires as chemical sensors," *Chemical Physics Letters*, vol. 369, p. 220, 2003. [cited at p. 18]

[19] B. Tian, X. Zheng, T. Kempa, Y. Fang, N. Yu, G. Yu, J. Huang., and C. Lieber, "Coaxial silicon nanowires as solar cells and nanoelectronic power source," *Nature*, vol. 449, p. 885, 2007. [cited at p. 18]

[20] F. Qian, S. Gradecak, Y. Li, C. Wen, and C. Lieber, "Core/multishell nanowire heterostructures as multicolor, high-efficiency light-emitting diodes," *Nano Letters*, vol. 5, p. 2287, 2005. [cited at p. 18]

[21] R. Gupta, Q. Xiong, C. Adu, U. Kim, and P. Eklund, "Laser-induced fano resonance scattering in silicon nanowires," *Nano Letters*, vol. 3, p. 627, 2003. [cited at p. 19, 30]

[22] M. Balkanski, R. Wallis, and E. Haro, "Anharmonic effects in light scattering due to optical phonons in silicon," *Physical Review B*, vol. 28, p. 1928, 1983. [cited at p. 19, 24]

[23] S. Piscanec, M. Cantoro, A. Ferrari, J. Zapien, Y. Lif-shitz, S. Lee, S. Hofmann, and J. Robertson, "Raman spectroscopy of silicon nanowires," *Physical Review B*, vol. 68, p. 241312, 2003. [cited at p. 19]

[24] I. Ponomareva, D. Srivastava, and M. Menon, "Thermal conductivity in thin silicon nanowires: Phonon confinement effect," *Nano Letters*, vol. 7, p. 1155, 2007. [cited at p. 19, 23, 25]

[25] A. Zwick and R. Carles, "Multiple-order raman scattering in crystalline and amorphous silicon," *Physical Review B*, vol. 48, p. 6024, 1993. [cited at p. 22]

[26] G. Allan, C. Delerue, and M. Lannoo, "Electronic structure of amorphous silicon nanoclusters," *Physical Review Letters*, vol. 78, p. 3161, 1997. [cited at p. 22]

[27] G. Allan, C. Delerue, and M. Lannoo, "Electronic structure and localized states in a model amorphous silicon," *Physical Review B*, vol. 57, p. 6933, 1998. [cited at p. 22]

[28] M. Marczak, J. Judek, A. Kozak, W. Gębicki, J. Jastrzębski, L. Adamowicz, D. Luxembourg, D. Hourlier, and T. Mlin, "The individual core/shell silicon nanowire structure probed by raman spectroscopy," *Physica Status Solidi C*, vol. 6, p. 2053, 2009. [cited at p. 23, 25]

[29] Y. Zhang, J. Christofferson, A. Shakouri, A. M. D. Li, Y. Wu, R. Fan, and P. Yang, "Characterization of heat transfer along a silicon nanowire using thermoreflectance technique," *IEEE Transactions on Nanotechnology*, vol. 5, p. 67, 2006. [cited at p. 23, 25]

[30] I. DeWolf, J. Jimenez, J. Landesman, C. Frigeri, E. D. P. Braun, and E. Calvet, *Raman and Luminescence for Microelectronics, Catalogue of optical and physical parameters*. European Commission, Directorate General Science, Research and Development, 1998. [cited at p. 23]

[31] Z. Su, J. Sha, G. Pan, J. Liu, D. Yang, C. Dickinson, and W. Zhou, "Temperature-dependent raman scattering of silicon nanowires," *The Journal of Physical Chemistry B*, vol. 110, p. 1229, 2006. [cited at p. 25]

[32] W. Bogusz, J. Garbarczyk, and F. Krok, *Podstawy Fizyki*. Oficyna Wydawnicza Politechniki Warszawskiej, 1999. [cited at p. 26, 29]

[33] I. Ford, "Semiconductors," *3C25 Solid State Physics Home Page*, 1999. http://www.cmmp.ucl.ac.uk/ ijf/3c25/notes9.pdf. [cited at p. 29]

[34] D. E. Perea, J. E. Allen, S. J. May, B. W. Wessels, D. N. Seidman, and L. J. Lauhon, "Three-dimensional nanoscale composition mapping of semiconductor nanowires," *Nano Letters*, vol. 6, p. 181, 2006. [cited at p. 29]

[35] P.Pareige, E.Cadel, and R.Lard, "Advances in the application of atom probe tomography to the study of semiconductor nanowires," in *Sumer School on Semiconductor Nanowires in Roscoff, France*, 2008. [cited at p. 29]

[36] F. Cerdeira, T. Fjeldly, and M. Cardona, "Effect of free carriers on zone-center vibrational modes in heavily doped p-type si. ii. optical modes," *Physical Review B*, vol. 8, p. 4734, 1973. [cited at p. 30, 31, 33]

[37] N. Nickel, P. Lengsfeld, and I. Sieber, "Raman spectroscopy of heavily doped polycrystalline silicon thin films," *Physical Review B*, vol. 61, p. 15558, 2000. [cited at p. 30]

[38] G. Whitesides, "The origins and the future of microfluidics," *Nature*, vol. 442, p. 368, 2006. [cited at p. 38, 60]

[39] D. Janasek, J. Franzke, and A. Manz, "Scaling and the design of miniaturized chemical-analysis systems," *Nature*, vol. 442, p. 374, 2006. [cited at p. 38, 60]

[40] R. Daw and J. Finkelstein, "Lab on a chip," *Nature*, vol. 442, p. 367, 2006. [cited at p. 38, 60]

[41] A. deMello, "Control and detection of chemical reactions in microfluidic systems," *Nature*, vol. 442, p. 394, 2006. [cited at p. 38]

[42] N. Islam, A. Zaman, and J. Wu, "Feedback control circuit for biased ac electroosmosis micropump," *Southeastcon, 2008. IEEE*, p. 27, 2008. [cited at p. 38]

[43] C. Cheng and C. Liu, "An electrolysis-bubble-actuated micropump based on the roughness gradient design of hydrophobic surface," *Journal of Microelectromechanical Systems*, vol. 16, p. 1095, 2007. [cited at p. 38]

[44] T. Lammerink, M. Elwenspoek, and J. Fluitman, "Integrated micro-liquid dosing system," *Micro Electro Mechanical Systems, Proceedings An Investigation of Micro Structures, Sensors, Actuators, Machines and Systems. IEEE.*, p. 254, 1993. [cited at p. 38]

[45] N. Green and H. Morgan, "Dielectrophoretic separation of nano-particles," *Journal of Physics D: Applied Physics*, vol. 30, p. L41, 1997. [cited at p. 38]

[46] H. Morgan, N. Green, M. Hughes, W. Monaghan, and T. Tan, "Large-area travelling-wave dielectrophoresis particle separator," *Journal of Micromechanics and Microengineering*, vol. 7, p. 65, 1997. [cited at p. 38]

[47] R. Hagedorn, G. Fuhr, T. Müler, and J. Gimsa, "Traveling-wave dielectrophoresis of microparticles," *Electrophoresis*, vol. 13, p. 49, 1992. [cited at p. 38, 48, 61]

[48] G. Fuhr, R. Hagedorn, T. Müler, W. Benecke, and J. G. B. Wagner, "Asynchronous traveling-wave induced linear motion of living cells," *Studia Biophysica*, vol. 140, p. 79, 1991. [cited at p. 38, 61]

[49] J. Melcher, "Traveling-wave induced electroconvection," [cited at p. 38, 39]

[50] J. Melcher and M. Firebaugh, "Traveling-wave bulk electroconvection induced across a temperature gradient," *The Phsics of Fluids*, vol. 10, p. 1178, 1967. [cited at p. 38, 39, 62]

[51] A. Ramos, H. Morgan, N. Green, A. González, and A. Castellanos, "Pumping of liquids with traveling-wave electroosmosis," *Journal of Applied Physics*, vol. 97, p. 084906, 2005. [cited at p. 39, 53, 62]

[52] J. Urbanski, T. Thorsten, J. Levitan, and M. Bazant, "Fast ac electro-osmotic micropumps with nonplanar electrodes," *Applied Physics Letters*, vol. 89, p. 143508, 2006. [cited at p. 39]

[53] M. Hughes, "Ac electrokinetics: applications for nanotechnology," *Nanotechnology*, vol. 11, p. 124, 2000. [cited at p. 39, 61]

[54] P. Gerwen, W. Laureyn, W. Laureys, G. Huyberechts, M. DeBeck, K. Baert, J. Suls, W. Sansen, P. Jakobs, L. Hermans, and R. Mertens, "Nanoscaled interdigitated electrode arrays for biochemical sensors," *Sensors and Actuators B*, vol. 49, p. 73, 1998. [cited at p. 39, 40]

[55] N. Green, H. Morgan, and A. Ramos, "Numerical solution of the dielectrophoretic and travelling wave forces for interdigitated electrode arrays using the finite element method," *Journal of Electrostatics*, vol. 56, p. 235, 2002. [cited at p. 40]

[56] T. Jones, "Basic theory of dielectrophoresis and electrorotation," *IEEE EMBS Magazine*, vol. 22, p. 33, 2003. [cited at p. 40]

[57] C. Kua, Y. Lam, C. Yang, K. Youcef-Toumi, and I. Rodriguez, "Modeling of dielectrophoretic force for moving dielectrophoresis electrodes," *Journal of Electrostatics*, vol. 66, p. 514, 2008. [cited at p. 40]

[58] K. Asami, "Dielectric dispersion in biological cells of complex geometry simulated by the three-dimensional finite difference method," *Journal of Physics D: Applied Physics*, vol. 39, p. 492, 2006. [cited at p. 40]

[59] K. Sekine, "Application of boundary element method to calculation of the complex permittivity of suspensions of cells in shape of d8h symmetry," *Bioelectrochemistry*, vol. 52, p. 1, 2000. [cited at p. 40]

[60] J. Gimsa and D. Wachner, "A unified resistor-capacitor model for impedance, dielectrophoresis, electrorotation, and induced transmembrane potential," *Journal of Biophysics*, vol. 75, p. 1107, 1998. [cited at p. 40]

[61] L. Yang, "Electrical impedance spectroscopy for detection of bacterial cells in suspensions using interdigitated microelectrodes," *Talanta*, vol. 74, p. 1621, 2008. [cited at p. 40]

[62] P. Patel and G. Markx, "Dielectric measurement of cell death," *Enzyme and Microbial Technology*, vol. 43, p. 463, 2008. [cited at p. 40]

[63] M. Varshney and Y. Li, "Interdigitated array microelectrodes based impedance biosensors for detection of bacterial cells," *Biosensors and Bioelectronics*, vol. 24, p. 2951, 2008. [cited at p. 40]

[64] L. Wana, W. Gonga, K. Jianga, H. Lia, B. Taoa, and J. Zhang, "Selective formation of silicon nanowires on pre-patterned substrates," *Applied Surface Science*, vol. 255, no. 6, p. 3752, 2009. [cited at p. 41]

[65] R. N. Sajjad and K. Alam, "Electronic properties of a strained <100> silicon nanowire," *Journal of Applied Physics*, vol. 105, p. 044307, 2009. [cited at p. 42]

[66] M. Marczak and D. Hourlier, "Interactions particularities of nanoobjects on solid state," *Tribologia*, vol. 3, p. 139, 2009. [cited at p. 43]

[67] H. Pohl, *Dielectrophoresis*. Cambridge University Press, 1978. [cited at p. 43, 48, 61]

[68] K. Oh, J.-H. Chung, J. Riley, Y. Liu, and W. Liu, "Fluid flow-assisted dielectrophoretic assembly of nanowires," *Langmuir*, vol. 23, p. 11932, 2007. [cited at p. 45]

[69] O. Englander, D. Christensen, J. Kim, L. Lin, and S. Morris, "Electric-field assisted growth and self-assembly of intrinsic silicon nanowires," *Nano Letters*, vol. 5, p. 705, 2005. [cited at p. 45]

[70] C. Highstrete, M. Lee, A. Vallett, S. Eichfeld, J. Redwing, and T. Mayer, "Disorder dominated microwave conductance spectra of doped silicon nanowire arrays," *Nano Letters*, vol. 8, p. 1557, 2008. [cited at p. 45]

[71] M. Wang and B. Gates, "Directed assembly of nanowires," *Materials Today*, vol. 12, p. 34, 2009. [cited at p. 45]

[72] A. Jamshidi, P. Pauzauskie, A. T. Ohta, H.-y. H. P.Y. Chiou, P. Yang, and M. Wu, "Semiconductor nanowire manipulation using optoelectronic tweezers," Tech. Rep. UCB/EECS-2006-116, 2006. [cited at p. 46]

[73] L. Benguigui and I. Lin, "More about the dielectrophoretic force," *Journal of Applied Physics*, vol. 53, p. 1141, 1982. [cited at p. 48]

[74] L. Benguigui and I. Lin, "The dielectrophoresis force," *American Journal of Physics*, vol. 54, p. 447, 1986. [cited at p. 48]

[75] M. Marczak and H. Diesinger, "Traveling wave dielectrophoresis micropump based on the dispersion of a capacitive electrode layer," *Journal of Applied Physics*, vol. 105, p. 124511, 2009. [cited at p. 60]

[76] R. Berry and H. Berg, "Torque generated by the flagellar motor of escherichia coli while driven backward," *Biophysica Journal*, vol. 76, p. 580, 1999. [cited at p. 61]

[77] B. Edwards, T. Mayer, and R.B.Bhiladvala, "Synchronous electrorotation of nanowires in fluid," *Nano Letters*, vol. 6, p. 626, 2006. [cited at p. 61, 62]

[78] D. Fan, F. Zhu, R. Cammarata, and C. Chien, "Controllable high-speed rotation of nanowires," *Physical Review Letters*, vol. 94, p. 247208, 2005. [cited at p. 62, 65]

[79] H. Craighead, "Nanoelectromechanical systems," *Science*, vol. 290, p. 1532, 2000. [cited at p. 73, 74]

[80] J. Boyd, "Epson using mems to create advanced inkjet heads for pos printers," *Technology Newsline, www.epson.co.jp*, 2003. [cited at p. 73]

[81] S. Evoy, D. Carr, L. Sekaric, A. Olkhovets, J. Parpia, and H. Craighead, "Nanofabrication and electrostatic operation of single-crystal silicon paddle oscillators," *Journal of Applied Physics*, vol. 86, no. 11, p. 6072, 1999. [cited at p. 74]

[82] P. V. Kessel, L. Hornbeck, R. Meier, and M. Douglass, "A mems-based projection display," *IEEE Proceedings*, vol. 86, p. 1687, 1998. [cited at p. 74]

[83] Z. Davis, G. Abadal, O. Kuhn, O. Hansen, F. Grey, and A. Boisen, "Fabrication and characterization of nanoresonating devices for mass detection," *Journal of Vacuum Science and Technology B*, vol. 18, p. 612, 2000. [cited at p. 74]

[84] B. Lassagne, D. Garcia-Sanchez, A. Aguasca, and A. Bachtold, "Ultrasensitive mass sensing with a nanotube electromechanical resonator," *Nano Letters*, vol. 8, p. 3735, 2008. [cited at p. 74]

[85] D. Smith, V. Holmberg, D. Lee, and B. Korgel, "Youngs modulus and size-dependent mechanical quality factor of nanoelectromechanical germanium nanowire resonators," *The Journal of Physical Chemistry C*, 2008. [cited at p. 78]

[86] S. Purcell, P. Vincent, C. Journet, and V. T. Binh, "Tuning of nanotube mechanical resonances by electric field pulling," *Physical Review Letters*, vol. 89, no. 27, p. 276103, 2002. [cited at p. 80]

Appendices

Appendix A

RC Model evolution

This appendix is related to section (3.2.3) where the theoretical background for our device is presented. Here I will focus on showing how the model is developed and I will provide more experimental data. First we have started with decomposing our setup to a simple RC circuit, but as it has turned out it was not sufficient. I will argumentate and show why we have taken into account all the modifications that have led to the model presented in section (3.2.3). Calculated values here are different from those in the text. The difference originates from the calibration of our model.

Model origins and evolution

We start with a simple model of our setup as an RC circuit. The impedance of the liquid in a channel is measured using a lock-in amplifier and a shunt - R_S. The aim is to modelize it as RC parallel circuit. As the cell for the measurement, we use the same channel that will later be used for pumping, that is, the array with insulated electrodes. This should prevent depletion of the liquid by chemical reactions, but adds another series capacitance C_{ins} due to the insulator. First we looked for insulator capacity C_{ins}, C_ϵ the capacity of the volume in the channel and the resistance R_{liq} of the volume in the channel. For further exploitation, we are interested in the ratio between these capacitances and the conductivity rather than

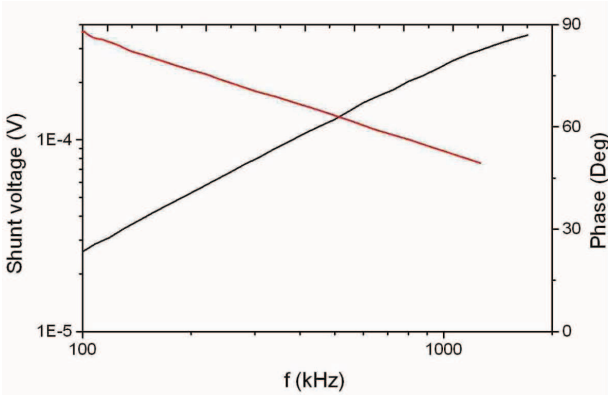

Figure A.1: Shunt voltage vs. frequency for a slightly conductive liquid.

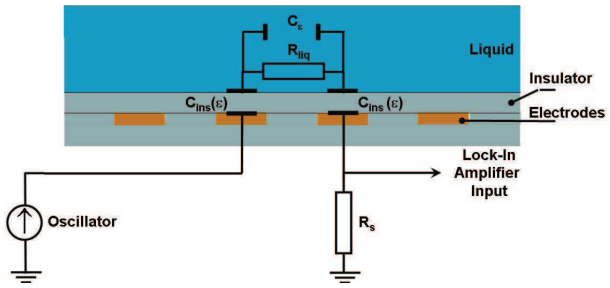

Figure A.2: Expected replacement circuit of the electrochemical cell of unknown impedance Z, in series with the shunt R_s, connected between the internal oscillator and A input of a lock-in amplifier.

the absolute value, because we want to obtain the frequency at which the imaginary part of the voltage drop in the channel, with respect to the overall applied voltage, is highest. For this measurement, it is not necessary to apply a propagative field using four electrodes.

It is sufficient to apply an AC voltage between two of the four electrode combs. Together with the shunt, we expect to have the replacement circuit of Fig. A.2. Fig. A.1 shows the shunt voltage on the 47 Ω resistor as a function of frequency. If we assume the voltage drop across the shunt is low compared to the $U_{appl} = 0.05\ V$, then the plotted signal can be proportional to the conductivity. The behavior looks like one for a RC circuit. Phase starts with 90° and is decreasing but it is difficult to say if this is the interaction of C_{ins} or C_ϵ with R. To obtain information about C_{ins} the channel was short-circuited by filling it with a highly concentrated NaCl solution. This leads to the replacement circuit presented in Fig. A.3. The resulting

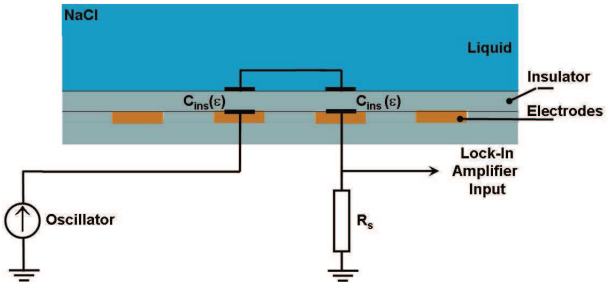

Figure A.3: Replacement circuit of the setup with the cell short-circuited by a highly conductive NaCl solution.

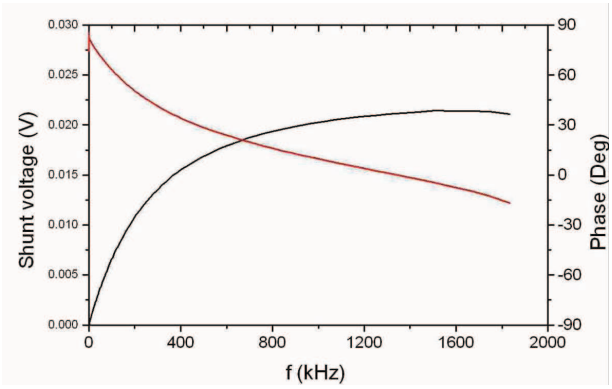

Figure A.4: Shunt voltage vs. frequency with a channel short circuited by a highly conductive NaCl solution.

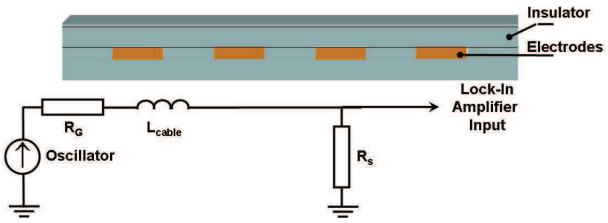

Figure A.5: Replacement circuit of the setup with the cell removed. R_G is generator impedance.

spectra at $U_{appl} = 0.05\ V$ are shown in Fig. A.4.

Against expectations the phase is not beginning at 90°, it is decreasing as one would expect at higher frequency when the capacitor becomes short-circuited, but then it drops below zero. For understanding this the cell was completely removed from the circuit and the wiring was short-circuited, as illustrated in Fig. A.5.

Now almost a constant signal was obtained over the spectrum (see Fig. A.6a),

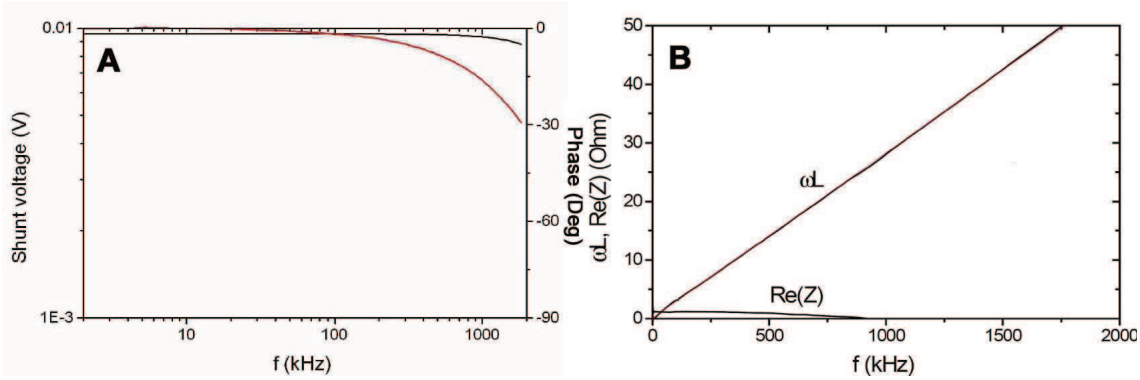

Figure A.6: Shunt voltage vs. frequency with a channel short circuited by a highly conductive NaCl solution.

only near 2 MHz, the signal decreases and the phase turns. The amplitude does not correspond to the applied one (U_{appl}=0.02 V) and the phase rotation is surprising. It turned out that the oscillator has 50 Ω output impedance (amplitude difference). The cabling inductance is found to be responsible for the frequency dependence. In the experimental setup a coaxial cable connects the internal oscillator to the cell support, then a non-coaxial wire (without the cell connected) goes from one BNC plug to the next, then another coaxial cable goes from the cell support to the input and then via a T connector, by another coaxial cable the shunt is connected. Here the non coaxial wire loop is modelized as an inductance. The improved replacement circuit accounting for these two effects is shown in Fig. A.5. Next, the voltage drop across the shunt is no longer neglected. The shunt voltage (form voltage divider) is calculated as follows

$$U_S = U_{OSC}\frac{R_S}{50\Omega + R_S + i\omega L} \ . \tag{A.1}$$

Resolving for ωL

$$i\omega L = \frac{U_{OSC}R_S}{U_S} - 50\Omega - R_S \ , \tag{A.2}$$

which is then split into real and imaginary part

$$0 = \frac{Re[U_S]U_{OSC}R_S}{U_S^2} - 50\Omega - R_S \tag{A.3}$$

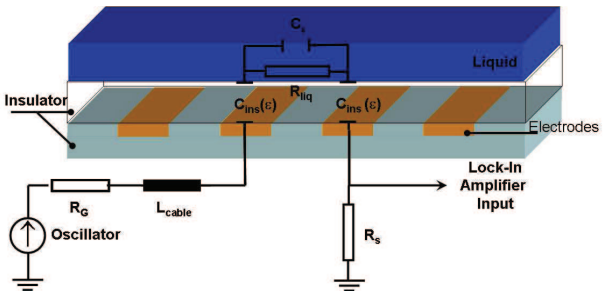

Figure A.7: Model of the setup consisting of the cell's insulating capacity C_{ins}, the resistance R_{liq} and capacitance C_ϵ of the liquid, and the components used in the setup to measure the cell impedance.

and we will get equation 3.19. When expression 3.19 is plotted over ω from the slope L (after dividing by 2π) can be obtained, as shown in A.6b. A value $L = 4.5$ μH was found. For the later experiment presented in Section 3.2.3 this value will be re-measured to be $L = 2$ μH due to the new cabling.

Next the cell is put back in place and the calculations are repeated. This time they are resolved for the unknown cell impedance Z. Equation A.1 becomes

$$U_S = U_{OSC}\frac{R_S}{50\Omega + R_S + i\omega L + Z} \tag{A.4}$$

and

$$Z = \frac{U_{OSC}R_S}{U_S} - 50\Omega - R_S - o\omega L\ . \tag{A.5}$$

Splitting to real and imaginary part gives Eqs. 3.20 and 3.21.

These are the real and imaginary impedance contributions of the cell itself. In Fig. A.9 a schema of the overall circuit with all components $R_G = 50\ \Omega$, L_{cable}, R_S and the cell components for the model *i.e.* C_{ins}, C_ϵ and R_S is shown.

Eqs. 3.20 and 3.21 are applied to obtain real and imaginary part of the cell impedance without the parasitic inductance cell nor R_S nor R_G nor L_{cable}.

For pumping, what we need is maximization of the complex part of the voltage drop across the channel. We look at equation that gives the voltage drop across the channel

$$U_{RC} = \frac{U_{appl}}{1 + \frac{C_\epsilon}{C_{ins}} + \frac{1}{i\omega RC_{ins}}}\ . \tag{A.6}$$

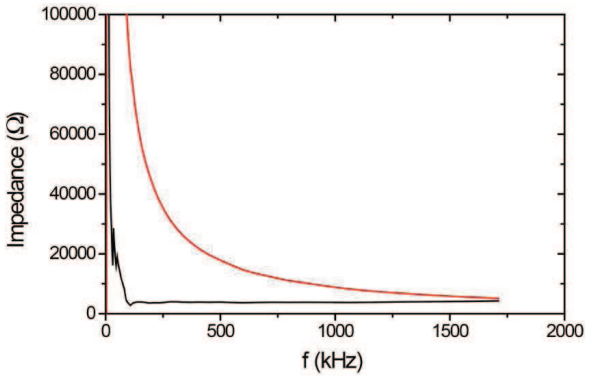

Figure A.8: Real and imaginary part of the cell impedance without the parasite inductance, for the slightly conductive liquid.

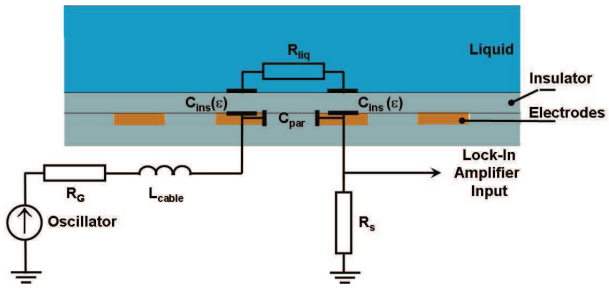

Figure A.9: Model of the setup consisting of the cells insulating capacity $C_{ins}$and the resistance R_σ of the liquid, and the components used in the setup to measure the cell impedance.

We have the simplification that $C_\epsilon < C_{ins}$ so that it can be neglected. The RC model of Fig. A.7 is replaced by a model without the capacitance C_ϵ of the liquid, shown in Fig. A.9. In this case, eq. A.6 simplifies to

$$U_{RC} \approx U_R \approx \frac{U_{appl}}{1 + \frac{1}{i\omega RC_{ins}}} \tag{A.7}$$

and one has to look for the crossover frequency where the insulating capacitances have an imaginary impedance $1/\omega C_{ins} = R$. If we check at the figure A.8A there is no crossover frequency, even if we zoom at high frequency.

The way to proceed now would be to measure the shunt voltage spectra, corrected immediately with Eqs. (3.20) and (3.21), to plot the impedance spectra and look for the crossover of real and imaginary part. If successful, then apply a propagative field at the same frequency. With the spectroscopic measurement we have obtained the values for the whole comb (n cells), but the crossover frequency is identical for

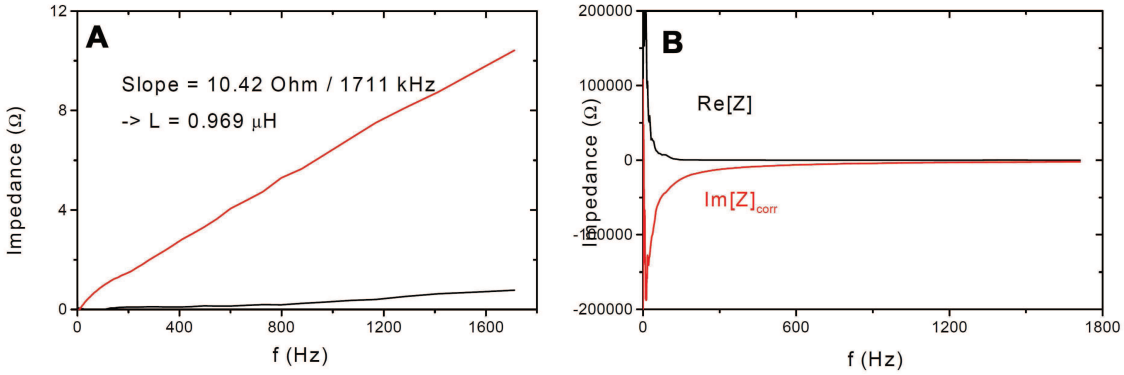

Figure A.10: (a) Expressions (A.3) and (3.19) plotted over f; (b) Impedance spectrum of the empty cell corrected to take into account the shunt (real part) and the inductance of the cabling (imaginary part) by applying Eqs. (3.20) and (3.21), respectively.

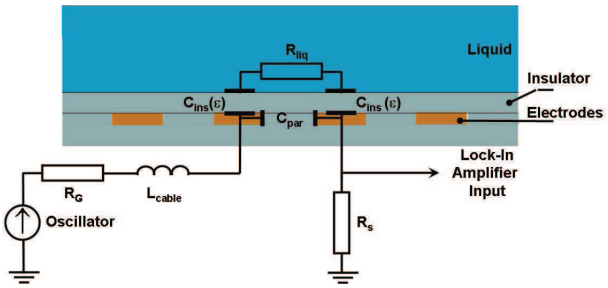

Figure A.11: Model of the setup consisting of the cell's insulating capacity C_{ins} and the resistance R_σ of the liquid, neglecting C_ϵ as in Fig. A.9 but adding the parallel parasitic capacity C_{par}. Along with the components used in the setup to measure the cell impedance.

an individual cell. The measurements with the cell shortcircuited, the cell without liquid and the filled cell were performed. First, we show the impedance spectra of the short-circuited cell to determine again the inductance of the cable loop, Fig. A.10a. By applying Eqs. (3.19) and (A.3) , R_s is found to be 49Ω for the real part of the impedance to be zero over the spectra, and L = 0.97 μH. Next, the cell impedance is measured with an empty cell. The impedance spectrum of the cell without liquid showed a new obstacle not yet taken into account : after applying Eqs. (A.5), (3.20) and (3.21) to subtract the inductive impedance from the cell impedance, the result is a cell impedance that becomes very low at high frequency. The origin of this non infinite impedance at high frequency is probably the parallel

capacitance present directly between the interdigitated electrode combs without the field lines crossing through the insulating layer and the liquid. The RC model that lastly had been simplified to yield the one shown in Fig. A.9 must be adapted correspondingly by adding the parallel parasitic capacitance C_{par} and is shown in Fig. A.11. The way to obtain its value is presented in section 3.2.3 starting from Eq. (3.22). The rest follows as in section 3.2.3.

Appendix B

Deposition errors

During nanowire deposition from liquid using dielectrophoreis many errors are possible. First thing that one has to take into account is top metalization height (Fig. 4.1). One has to know the nanowire height. Otherwise during the lift-off process with the resin nanowires higher than the metalisation will detach from the electrodes like shown in Fig. B.1. On the left are many nanowires before metalizationa and on the right after the process half of the nanowiers are gone. However this could be use to eliminate bigger naowires form the deposition.

Another error presented on the Fig. B.2A is a tricky one. Sometimes during

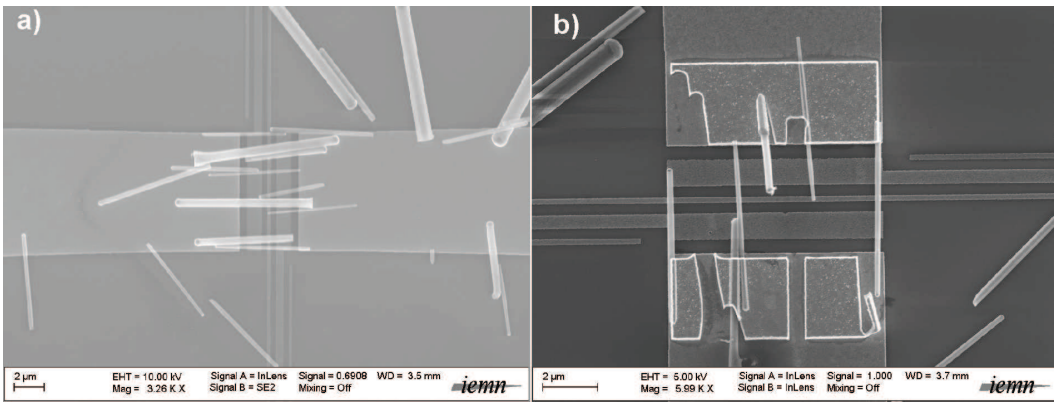

Figure B.1: Possible errors (1): A SEM image of the electrode after nanowires deposition (a) and after top metalization (b). Top metallization height was to low to fix bigger nanowires, resulting in their detach during the lift-off process

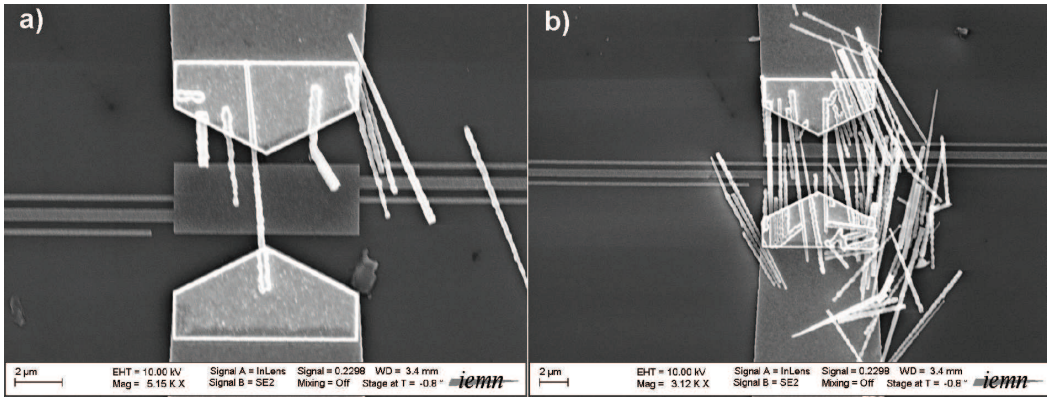

Figure B.2: Possible errors (2): On the left picture (a) nanowires bridge the gate with suspending electrode. It is possible to fix with contact AFM. On the right picture (b) deposition time was too long and to many nanowires have deposited.

the deposition a bigger nanowire will deposit bridging the gate (G) electrode with the source (S)/ drain (D) electrode. Due to this bridge a dielectrophoresis effect will also occur between G and S/D electrode. This will result in short nanowire deposition, as visible on the picture. This sort of error can be fixed using AFM in contact mode, by pushing the erroneous SiNWs away withe the tip.

On the Fig. B.2B an excess number of nanowire has deposited. This was a result of high nanowires concentration in the liquid. After few depositions like this we have mounted in a current switch to our power supply circuit. As we can observe the electrodes under the optical microscope it is possible to see nanowires depositing. When there is one it is enough to switch off the field. However in 2 cases from 10 the nanowire will detach. And the deposition has to be repeated.

The last two errors are related with the top metalization process itself. In the Fig. B.3A we can see that the e-beam lithography process was not precise. There is a shift of $10 - 20$ nm. In case of a big structures it is not disturbing but for the in case we try to build a side electrodes where the precision is extremely important this can destroy the whole deposition (see Fig. B.4). This error was due to some problem with the e-beam lithography machine (two months later it broke down). Last error presented in Fig. B.3B is hard to explain. From time to time after top metalization nanowire is gone and electrode below also. This can be caused maybe by some extra charge accumulated on the nanowire.

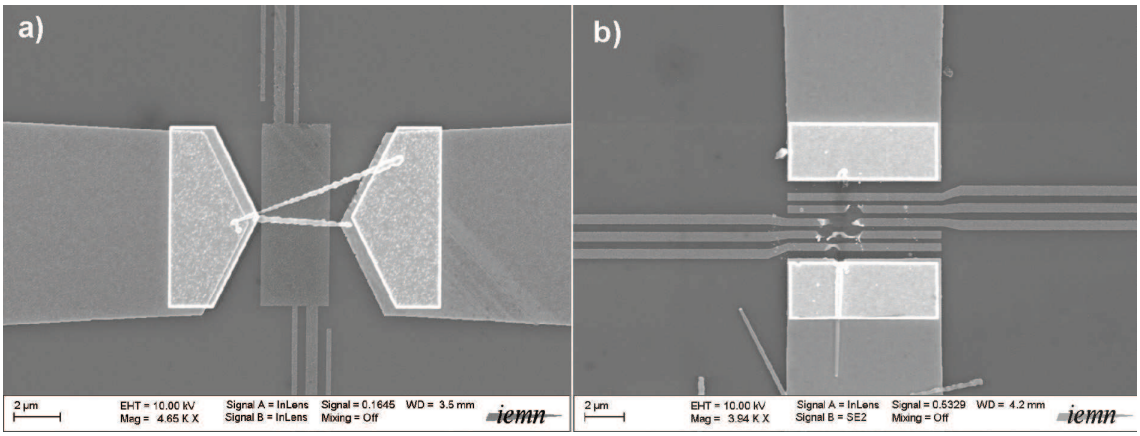

Figure B.3: Possible errors (a): Top metalization miss alignment resulting in faulty nanowires connection; (b) During the metal deposition or lift-off prosses some charges accumulated and nanowire has burned, as well as electrodes below

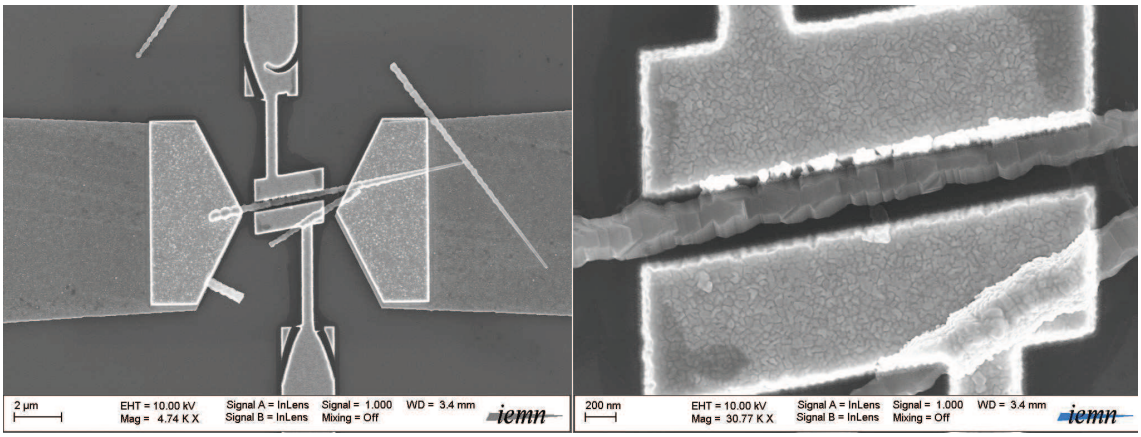

Figure B.4: Misalignment has caused binding of the side electrodes with the nanowire, making it unusable.

Publications

1. **M. Marczak**, J. Judek, A. Kozak, W. Gebicki, C. Jastrzebski, L. Adamowicz, D. Luxembourg, D. Hourlier and T. Mélin, "The individual core/shell silicon nanowires' structure probed by Raman spectroscopy" *Physica Status Solidi C*, vol. 6, p. 2053, **2009**

2. J. Judek, D. Brunel, T. Mélin **M. Marczak**, M. Zdrojek, W. Gebicki, L. Adamowicz, "Light-polarized resonant Raman spectra from individual single- and double-wall carbon nanotubes", *Phys. Status Solidi C*, vol. 6, p. 2056, **2009**

3. **M. Marczak** and H. Diesinger, "Traveling wave dielectrophoresis micropump based on structural dispersion, using impedance spectroscopy as feedback", *Journal of Applied Physics* vol. 105, 12, p. 124511 **2009**

4. **M. Marczak**, D. Hourlier, "Osobliwosci stykun nanoobiektow z powierzchnia ciala stalego", *Tribologia* vol. 225, p. 139, **2009**

5. **M. Marczak**, D. Hourlier, T. Mélin, L. Adamowicz and H. Diesinger, "Competition between dielectrophoretic forces for the manipulation of nanowires in liquid environment", *Applied Physics Letters*: submitted (2009)

Presentations and Posters

Presentations

2009 *Competition between dielectrophoretic forces for the manipulation of nanowires in the liquid*, Nanowires School, Autrans **(France)**

2009 *Nanowire assembly by dielectrophoresis*, IEMN in-house seminar, Lille **(France)**

2008 *Raman spectroscopy of boron-doped silicon nanowires*, European Materials Research Society, Warsaw **(Poland)**

2008 *Wyjasnienie istoty sladu nanodrutu (nanorurki) po ich przesunieciu*, M. Marczak; Warsztaty Tribologiczne - Nanotribologia. Wydzial Chemii Uniwersytetu Lodzkiego **(Poland)**

2006 *Raman spectroscopy characterization of single silicon nanowires*, 6th International Conference on Materials for Microelectronics and Nanoengineering, Cranfield **(Great Britain)**

2006 *Problems in tribology - vision and reality*, in cooperation with Prof. Dr Hab. Ing. Dr h.c. R. Marczak, 4th Tribological Meeting, Poznań **(Poland)**

2006 *Nanowires assembly by dielectrophoresis and raman spectroscopy of single silicon nanowires*, IEMN in-house seminar, Lille **(France)**

2006 *Nanowires assembly by dielectrophoresis*, Nanospectra Network Meeting (European Network Program), Zürich **(Switzerland)**

2006 *Raman spectroscopy of silicon nanowires*, Raman Spectroscopy Day, IEMN, Lille **(France)**

Posters

2008 *Characterization of the individual core/ shell silicon nanowires*, European Materials Research Society, Warsaw **(Poland)**

2008 *Raman spectroscopy of boron doped silicon nanowires*, Summer school on semiconductor nanowires, Roscoff **(France)**

2007 *Raman spectroscopy of individual cone-shaped nanowires*, 12th International Conference on Phonon Scattering in Condensed Matter, Paris **(France)**

2007 *Characterization and controlled assembly of single silicon nanowires*, IEMN PhD Day, Lille **(France)**

2006 *Single Si-based silicon nanowire raman spectroscopy*, European Material Research Society, Nice **(France)**

2006 Nanospectra Network Meeting (European Network Program), Hamburg, **(Germany)**